



Politechnika Wrocławska

FIELD OF SCIENCE: Engineering and technology

DISCIPLINE OF SCIENCE: automation, electronic, electrical
engineering and space technologies

DOCTORAL DISSERTATION

**Spectral conversion of ultrashort
laser pulses in nonlinear optical
fibers**

Mrs. Olga Szewczyk, MSc., Eng.

Supervisor/Supervisors:
dr hab. inż. Grzegorz Soboń

Keywords: nonlinear optics, microstructured fibers, nonlinear
effects in optical fibers

WROCŁAW 2023

I would like to thank my Supervisor dr hab. inż. Grzegorz Soboń for the mentorship, as well as continuous support and supervision throughout these few years. I would also like to thank dr hab. inż. Jarosław Sotor for sharing knowledge and support.

I would like to thank the team of the Laser & Fiber Electronics Group for the support and cooperation especially including: Dorota Tomaszewska-Rolla, Zbigniew Łaszczych, Dorota Stachowiak and Piotr Bojęś. It was fun and pleasure to work together in an office for few years.

Thanks to Dr. Aleksandra Foltynowicz-Matyba from Optical Frequency Comb Spectroscopy Group for the support during my short stay in Umeå, Sweden.

I'd like to express my gratitude to dr hab. inż. Karol Tarnowski for sharing knowledge and experience on the numerical simulations.

Lastly, I am also grateful to my family for their patience and encouragement. And, especially, my husband, Kacper, for the unconditional support and understanding during these intense years.

I would like to acknowledge funding:

- "Spectral compression of ultrashort laser pulses tunable in the biological window of 1600-1800 nm", Preludium, NCN, UMO-2022/45/N/ST7/03175
- "Polarization-maintaining dispersion-engineered fiber modules in the spectral range 1500-2000 nm", NCBR, POIR.04.01.01-00-0024/19
- "Dispersion-engineered fiber modules for tunable laser sources", NCBR, POIR.04.01.01-00-0037/17

Contents

List of Acronyms	5
1 Introduction	6
2 Nonlinear fiber optics: theoretical background	10
2.1 Introduction	10
2.2 Pulse propagation in optical fibers	11
2.2.1 Optical fibers: basic features	11
2.2.2 Mathematical description of electromagnetic wave propagation . . .	12
2.2.3 Fiber attenuation	14
2.2.4 Chromatic dispersion	15
2.3 Generalized Nonlinear Schrödinger Equation	18
2.3.1 Pulse propagation in the presence of dispersion only	19
2.3.2 Pulse propagation in the presence of nonlinearities only	21
2.4 Fundamentals of nonlinear phenomena	22
2.4.1 Self-phase modulation	23
2.4.2 Soliton solution	25
2.4.3 Modulation Instability	28
2.4.4 Cross-Phase Modulation (XPM)	30
2.4.5 Stimulated Raman Scattering	31
2.4.6 Four-Wave Mixing (FWM)	34
2.5 Numerical methods for simulating pulse propagation	35
2.6 Microstructured optical fibers (MOF)	36
2.6.1 Historical perspective and the idea of the MOF	36
2.6.2 Fiber structure	37
2.6.3 SSFS effect in air-silica MOF	39
2.6.4 Supercontinuum generation	41
2.6.5 Supercontinuum in the anomalous dispersion regime	42
2.6.6 All-Normal Dispersion (ANDi) supercontinuum	44
2.7 Pulse characterization methods	47
2.7.1 Dispersive Fourier Transform (DFT)	47
2.7.2 Pulse-to-pulse coherence	50
2.7.3 Frequency Resolved Optical Gating (FROG) measurements	51
2.7.4 Relative Intensity Noise (RIN)	52
3 Dual-wavelength pumped highly birefringent microstructured silica fiber	55
3.1 Introduction	55
3.2 Microstructured silica fiber	56
3.2.1 The aim of the study	56

3.2.2	Description of the fiber structure	56
3.3	Experimental results of the SSFS generation in the MOF	57
3.3.1	Coherence measurements	61
3.3.2	SSFS for different MOF segments	62
3.3.3	Polarization extinction ratio measurements	62
3.4	Conclusions	65
4	ANDi supercontinuum and SSFS as seed sources for Thulium-doped fiber amplifiers	67
4.1	Introduction	67
4.2	Spectral conversion for 2 μm laser sources: SSFS and ANDi-SC	68
4.3	Experimental setup	70
4.3.1	Measurement results	73
4.3.2	Tm-doped fiber amplifier seeded with ANDi-SC and SSFS	77
4.3.3	Relative intensity noise	78
4.4	Conclusions	83
5	Spectral compression and amplification of the frequency-shifted solitons	84
5.1	Introduction	84
5.2	Spectral compression technique	85
5.3	Numerical model of the spectral compression technique	87
5.3.1	Dispersion-increasing fiber at 1730 nm	88
5.3.2	Original comb-profile dispersion model	89
5.4	Narrow linewidth laser source. Experimental results.	95
5.4.1	Short-wavelength Tm-doped fiber amplifier.	98
5.5	Conclusions	99
6	Conclusions	100
	Streszczenie	102
	Abstract	104
	References	106
	List of achievements	121

List of Acronyms

ANDi	All-Normal Dispersion
CPF	Comb-Profile Fiber
DFT	Dispersive Fourier Transform
EDFL	Erbium-doped fiber laser
FROG	Frequency Resolved Optical Gating
GNLSE	Generalized Nonlinear Schrödinger Equation
GVD	Group Velocity Dispersion
MOF	Microstructured Optical Fiber
OCT	Optical Coherence Tomography
PCF	Photonic Crystal Fiber
PER	polarization extinction ratio
PM	polarization-maintaining
RIN	Relative Intensity Noise
SBS	Stimulated Brillouin Scattering
SPM	Self-Phase Modulation
SRS	Stimulated Raman Scattering
SSFS	Soliton Self-Frequency Shift
TOD	Third-Order Dispersion
YDFL	Ytterbium-doped fiber laser
ZDW	zero-dispersion wavelength

Chapter 1

Introduction

The area of nonlinear fiber optics has been an enormous research platform since the development of the first low-loss fiber in 1970. During these 50 years, the research evolved from concentrating on low-loss transmission and maintaining the proper quality of the signal to creating the μm -level structures inside the silica glass fibers. Optical fibers are now an essential part of not only telecommunication systems, but are also widely used as sensors or endoscopes for medical measurements, in power transmission systems, and numerous laser system configurations. All-fiber setups are easy to adjust, are prone to environmental conditions and possess a high potential of miniaturization and integration. What is more, fiber-based lasers are characterized by excellent beam quality and ease of heat dissipation in contrast to high-power solid-state lasers.

The invention of microstructured optical fibers (MOF) was a huge revolution to fiber laser systems. Their flexibility in designing nonlinear and dispersive parameters of the fiber allows for observation and generation of the nonlinear effects at levels that were not achievable before. This possibility is a direct consequence of the MOF feature, where the effective mode area can be decreased, which significantly increases the efficiency of the nonlinear processes. The nonlinear fibers combined with the simultaneously developed area of the ultrafast pulsed lasers allow to make sources widely used in spectroscopy, biomedical imaging, and frequency comb generation.

Indeed, the development of nonlinear optics would not be possible without the proper laser sources. Here, especially ultrafast fiber lasers generating pulses of a duration as short as even few femtoseconds are essential to generate a wide variety of phenomena in different optical fibers. Femtosecond lasers that implement different mode-locking mechanisms, such as graphene, SESAM, carbon nanotubes or nonlinear polarization evolution, have proved to provide a stable train of ultrashort pulses. The intensity levels of such pulses are high enough to allow for observations of various nonlinear effects. One of them is a spectral conversion that enables to shift the operating wavelength towards a desired wavelength region. As a result, we can aim at wavelengths that are not normally achieved through direct emission. Figure 1.1 shows the spectral coverage of the existing active media: Neodymium (Nd), Ytterbium (Yb), Erbium (Er), Thulium (Tm), and Holmium (Ho). It is clearly visible that these media do not cover all wavelengths. Yet, regions such

as 1.3 or 1.7 μm have recently started drawing attention due to their possible application in biomedical areas such as three-photon microscopy and optical coherence tomography. There is ongoing research on laser sources operating at these wavelengths, however, their efficiency is significantly limited. The solution here would be to implement nonlinear fibers with ultrafast lasers to shift the operating wavelength to the desired region. The spectral conversion in these fibers could successfully fill the gap in the spectral bandwidth between the available gain media. Such sources are going to be demonstrated in this dissertation.

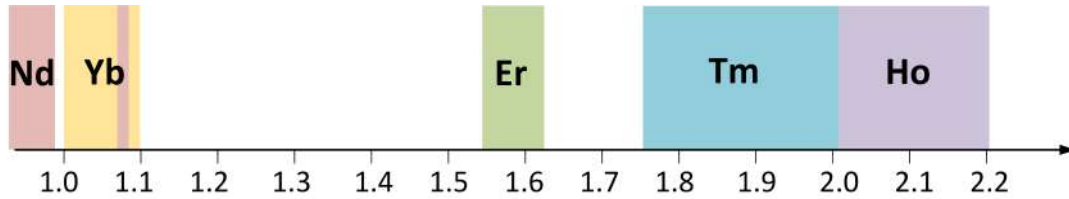


Figure 1.1: Spectral coverage of the gain media: Neodymium (Nd), Ytterbium (Yb), Erbium (Er), Thulium (Tm) and Holmium (Ho).

The combination of ultrafast lasers and nonlinear fibers makes a powerful tool that can be tailored for specific requirements. On the one hand, one can adjust laser pulse parameters such as pulse duration and a peak power, on the other, we can modify the fiber parameters in various ways, e.g., to change the zero-dispersion wavelength or increase the nonlinearities. However, although versatile and adaptive, these laser sources must satisfy a number of requirements for applications such as frequency metrology, spectroscopy or biomedical imaging. In these areas, the demands for possible sources are high, and the noise properties need to be highly controlled and suppressed. The requirements include high stability, high degree of coherence and excellent intensity noise properties. For this purpose, several methods and techniques have been developed and implemented to investigate the noise dynamics of the laser sources based on the nonlinear fibers.

The dissertation is devoted to an analysis of the spectral conversion phenomenon in nonlinear silica fibers. The conducted research included the generation and description of Soliton Self-Frequency Shift (SSFS) and supercontinuum effects, the investigation of the stability and noise properties of the generated signals, numerical simulations of these effects and the impact of self-phase modulation (SPM) on the pulse spectrum.

The aim of the research was:

- The characterization of the spectral conversion phenomenon in air-silica microstructured fiber when pumped with different laser sources (the Ytterbium- and Erbium-doped fiber lasers)
- A complete noise characterization of the nonlinear effects: SSFS generated in anomalous-dispersion fiber and supercontinuum in normal-dispersion fiber
- Numerical analysis of a spectral compression effect in an optical fiber with non-constant dispersion profile.

- An assembly of a setup of a narrow-linewidth laser source tunable in the wavelength range of 1650-1900 nm with an additional amplification stage.

The thesis was:

- Spectrally-shifted solitons generated in the anomalous dispersion regime possess as good stability as the all-normal dispersion supercontinuum and can be used as seeds for Tm-doped fiber amplifiers.
- The SSFS phenomenon allows for the generation of narrow-linewidth spectrally shifted solitons.

The dissertation consists of 6 Chapters, including Introduction and Conclusions. Chapter 2 provides theoretical background, Chapters 3 to 5 describe experimental work conducted by the Author.

Chapter 2 begins with an introduction to nonlinear effects in optical fibers. It contains theoretical information on ultrashort pulse propagation in an optical fiber, the nonlinear effects and dispersion that affect such pulses. The origins of a stimulated Raman scattering that leads to the spectral conversion process of the optical pulses provided to the fiber are discussed. The two major nonlinear effects: the soliton self-frequency shift (SSFS) and the supercontinuum are described. Also, a technique that is used to numerically model the nonlinear phenomena in optical fibers is presented. In the end, the microstructured optical fiber's design is given and the nonlinear effects such as SSFS and supercontinuum are simulated in segments of such fibers.

Chapter 3 presents the analysis of a microstructured silica fiber pumped in a dual-wavelength regime. Since the MOF technology allows for flexibility in designing fiber dispersion and nonlinearity properties, it opens new possibilities for creating fiber-based systems adapted to multi-wavelength pumping. Specifically, by shifting the ZDW towards shorter wavelengths, one can obtain a fiber suitable for two common pumping wavelengths: 1 μm and 1.5 μm . In this Chapter, the results of SSFS effect generated for two pumping sources in such a fiber are going to be demonstrated. The research is a result of the cooperation with the Faculty of Fundamental Problems of Technology, the Laboratory of Optical Fiber Technology in Lublin and the Fibrain Company from Zaczernie as a part of the research project. The goal of the project was to generate frequency-shifted solitons in the fabricated MOF for two pumping laser sources, and perform full characterization including measurements of optical spectra, average power levels stored in the solitons, pulse-to-pulse coherence and polarization extinction ratio.

Chapter 4 concentrates on the comprehensive noise characteristics of two nonlinear phenomena: SSFS and All-Normal Dispersion (ANDi)-supercontinuum, generated in a microstructured silica fiber designed for different dispersion regimes: anomalous and normal dispersion. The research addresses the current problem of finding a femtosecond laser source operating at 2 μm that would feature low noise and good stability. The

nonlinear effects generated in the microstructured fibers stand as an alternative to the direct emission with the use of Ho- and Tm-based sources. In this Chapter, an analysis of pulse-to-pulse coherence, shot-to-shot noise and amplitude noise for two nonlinear effects generated in MOFs with opposite dispersion profiles is being discussed and compared. Eventually, a Tm-doped fiber amplifier seeded by two generated nonlinear phenomena: SSFS and ANDi-SC, is presented. The fiber amplifier in two configurations has been compared in terms of intensity noise and characterized by the Frequency Resolved Optical gating (FROG) measurements.

Chapter 5 presents the description of the spectral compression technique that can be provided in a specially designed Comb-Profile Fiber (CPF). The first part concentrates on the comprehensive numerical analysis of the phenomenon. This part includes the simulations performed for an ideal CPF where the dispersion is described with a formula, and for a fiber that is combined of two commercially available fibers in such a way that the resulting dispersion profile varies along the fiber length. For the latter case, different configurations are tested. Next, the optimal configuration of the CPF is found and investigated in the experimental part. The ultrashort laser pulses from the Erbium-doped fiber laser are provided to a PM-SMF to obtain optical solitons tunable in the wavelength range between 1620-1900 nm. Then, these pulses go to the CPF. As a result, the assembled setup emerged as a narrow-linewidth laser source with the tuning possibility in the wavelength range of 1622-1900. In the end, the amplification stage is presented with the Thulium-doped amplifier adjusted for the short-wavelength range (1650-1860 nm).

Chapter 2

Nonlinear fiber optics: theoretical background

2.1 Introduction

Fiber optic systems have been attracting attention for a long time, but the real interest began in the 70s of the 20th century when fiber losses were reduced to the level of 20 dB/km [1]. Further development of the fiber fabrication allowed for the fiber loss to be scaled down to 0.2 dB/km for 1.55 μm wavelength [2]. The possibility of the low-loss transmission through optical fibers led to the enormous progress not only in the field of fiber optic telecommunication systems [3, 4], but it started a new research area on nonlinear optics [5, 6]. Soon after the first low-loss fiber was presented by Corning [1], the researchers in Bell laboratory observed numerous nonlinear effects in silica fiber such as Self-Phase Modulation (SPM), Four-Wave Mixing (FWM), Stimulated Raman Scattering (SRS), and Stimulated Brillouin Scattering (SBS) [7–12]. The intense studies on various nonlinear phenomena led to the revelation that optical fibers can support soliton pulses due to the interplay between dispersion and nonlinearities in the fiber [13] and the actual observation of the soliton in the optical fiber by Mollenauer et al. [14]. This major discovery was a real breakthrough as it enabled numerous advances in ultrashort pulse generation and pulse control, methods of pulse compression, and optical switching techniques.

A new revelation was finding that optical fibers can be doped with rare-earth elements (such as Erbium, Ytterbium, Thulium, and Holmium). It opened the possibility to build fiber lasers and amplifiers. What is more, together with the generation of the nonlinear effects also in the optical fibers, it is now possible to build entirely fiberized systems. Such setups became popular due to numerous advantages they offer, immunity to dis-adjustment, the possibility to be used outside the laboratory environment and often relatively low costs.

In this Chapter, basic information on the nonlinear phenomena in optical fibers is going to be demonstrated. An ultrashort pulse propagation inside the optical fiber is going to be analyzed in terms of dispersion, SPM and SRS. One of the most important formulas in nonlinear optics, the Nonlinear Schrödinger Equation, is going to be described. Examples

of different types of microstructured silica fibers are going to be presented. Eventually, the method for simulating pulse behaviour in the fiber is going to be explained.

2.2 Pulse propagation in optical fibers

2.2.1 Optical fibers: basic features

When we launch light into an optical fiber, it remains in the core and is propagated along the fiber length as a result of dielectric waveguiding. This mechanism is called *total internal reflection* and can be possible due to the core/cladding refractive index difference. This fact is the main distinction between optical fibers and bulk media, such as nonlinear crystals and liquids. The core diameter for single-mode fibers is $<10\ \mu\text{m}$, but it can be reduced to even below $1\ \mu\text{m}$ for microstructured silica fibers, which are extensively developed nowadays.

The silica glass is not especially known for its extraordinary nonlinear properties. In fact, it exhibits a relatively low nonlinear coefficient, even up to 100 smaller when compared to other nonlinear crystals and liquids [15]. When comparing the values of Raman and Brillouin coefficients with other nonlinear media, the values for silica are usually 2 orders of magnitude lower [16]. Nevertheless, there are a few unquestionable advantages of glass which make it a perfect material for the light transmission [17]:

- Low-loss transmission ($<1\ \text{dB/km}$). Although silica fibers feature low nonlinearities, they are able to transmit light over long distances maintaining the optical intensities of the signal. Today, most commercially available optical fibers are able to transmit 96% of the power over a 1 km fiber length.
- Wide range of accessible temperatures. Unlike many materials, such as metals, or water, glass does not become solid at a discrete temperature. It gets stiffer in a broader range of temperatures which is used as a feature to draw optical fibers.
- The strength of glass which is estimated to be around $140,000\ \text{kg/cm}^2$ [17]. A glass fiber that is used in telecommunication systems possesses a diameter of $125\ \mu\text{m}$ which corresponds to twice the human hair thickness, and is possible to support an $\approx 18\ \text{kg}$ load.

The efficiency of a nonlinear process is defined as a product of optical intensity (I_0) and the effective length L_{eff} where this intensity is maintained [18]. If the light is focused on a region with a spot of a radius w_0 , then the optical intensity can be described as $I_0 = P_0/(\pi w_0^2)$, where P_0 refers to the optical power of the incident light. From this relation, it can be concluded that the optical intensity can be easily increased by reducing the value of w_0 . However, for a Gaussian beam, the effective length is proportional to the spot area ($L_{eff} \propto \pi w_0^2/\lambda$, where λ denotes wavelength), therefore reducing the beam radius would consequently reduce the L_{eff} . For bulk media, the efficiency of a process is

described as:

$$(I_0 L_{eff})_{bulk} = \left(\frac{P_0}{\pi w_0^2} \right) \frac{\pi w_0^2}{\lambda} = \frac{P_0}{\lambda}, \quad (2.1)$$

and it does not depend on the spot size.

The spot size w_0 in a single-mode fiber is determined by the fiber core diameter and the core/cladding refractive index difference. Since the same spot size is kept along the entire fiber length L , the effective length is limited only by the fiber loss α . If we consider that $I(z) = I_0 \exp(-\alpha z)$, and that $I_0 = P_0/(\pi w_0^2)$, where P_0 determines the optical power coupled into the fiber, the efficiency of the process is described as:

$$(I_0 L_{eff})_{fiber} = \int_0^L I_0 e^{-\alpha z} dz = \frac{P_0}{\pi w_0^2 \alpha} (1 - e^{-\alpha L}). \quad (2.2)$$

When comparing Equations 2.1 and 2.2, it can be noticed that for long fibers, the efficiency can be improved by the factor:

$$\frac{(I_0 L_{eff})_{bulk}}{(I_0 L_{eff})_{fiber}} = \frac{\lambda}{\pi w_0^2 \alpha}, \quad (2.3)$$

where the assumption was that $\alpha L \gg 1$. For the wavelength $\lambda = 0.43 \mu\text{m}$ in the visible region, the spot size $w_0^2 = 2 \mu\text{m}$, and $\alpha = 2.5 \times 10^{-5} \text{ cm}^{-1}$ (10 dB/km), the enhancement factor is almost 10^7 . For the near-infrared region ($\lambda = 1.55 \mu\text{m}$), and fiber loss $\alpha = 0.2 \text{ dB/km}$, the enhancement factor reaches 10^9 . Such enormous values of efficiency enhancement of the nonlinear phenomena make silica single-mode fibers an optimal medium for the generation and observation of numerous nonlinear processes at relatively low optical power levels.

2.2.2 Mathematical description of electromagnetic wave propagation

The propagation of an electromagnetic field in optical fibers is governed by Maxwell's equations. In the International System of Units, they are defined as [19]:

$$\nabla \times \mathbf{E} = -\frac{\partial \mathbf{B}}{\partial t}, \quad (2.4)$$

$$\nabla \times \mathbf{H} = \mathbf{J} + \frac{\partial \mathbf{D}}{\partial t}, \quad (2.5)$$

$$\nabla \cdot \mathbf{D} = \rho_f, \quad (2.6)$$

$$\nabla \cdot \mathbf{B} = 0, \quad (2.7)$$

where symbols \mathbf{E} and \mathbf{H} refer to electric and magnetic field vectors, respectively, and \mathbf{D} and \mathbf{B} correspond to electric and magnetic flux densities. The sources for the electromagnetic field are represented by the current density vector \mathbf{J} and the charge density ρ_f . In a medium such as an optical fiber, where there are no free charges, both these symbols \mathbf{J}

and ρ_f amount to zero.

Both magnitudes of electric and magnetic flux densities \mathbf{D} and \mathbf{B} are directly related to the vectors \mathbf{E} and \mathbf{H} through the relations, specifically:

$$\mathbf{D} = \epsilon_0 \mathbf{E} + \mathbf{P}, \quad (2.8)$$

$$\mathbf{B} = \mu_0 \mathbf{H} + \mathbf{M}, \quad (2.9)$$

where ϵ_0 has already been described above as the vacuum permittivity, μ_0 refers to vacuum permeability, and \mathbf{P} and \mathbf{M} correspond to electric and magnetic polarizations. The optical fibers are made of silica, which is a nonmagnetic material, hence $\mathbf{M}=0$. The parameters μ_0 and ϵ_0 are constants, and their values are [20]:

$$\mu_0 = 4\pi \times 10^{-7} \text{ H/m}, \quad (2.10)$$

$$\epsilon_0 = \frac{10^{-9}}{36\pi} \text{ F/m}. \quad (2.11)$$

The Maxwell's equations gathered above can be used to define the wave equation describing light propagation in optical fibers where the electric and magnetic fields are simply two aspects of a physical phenomenon which is an electromagnetic field. The general form for the wave equation can be obtained by first taking the curl of Eq. 2.4 and using Eqs. 2.5, 2.8, and 2.9. This way, one can replace \mathbf{B} and \mathbf{D} with \mathbf{E} and \mathbf{P} and obtain:

$$\nabla \times \nabla \times \mathbf{E} = -\frac{1}{c^2} \frac{\partial^2 \mathbf{E}}{\partial t^2} - \mu_0 \frac{\partial^2 \mathbf{P}}{\partial t^2}, \quad (2.12)$$

where c corresponds to the speed of light in a vacuum. Here the relation between the constants μ_0 and ϵ_0 was implemented:

$$\mu_0 \epsilon_0 = 1/c^2. \quad (2.13)$$

This relation between the speed of light and the electric and magnetic properties of a material was one of the greatest achievements of Maxwell's theory. When regarding the constants' values from Eqs. 2.10 and 2.11, one can obtain the value for the velocity of light in a vacuum [20]:

$$c = 2.997924562 \times 10^8 \text{ m/s}. \quad (2.14)$$

Naturally, in any material, the velocity of propagating light is less than c . The *index of refraction*, n , is a parameter that describes the relation between the speed of light, c , and the velocity of light in the material, ν :

$$n = \frac{c}{\nu} = \sqrt{\frac{\epsilon\mu}{\epsilon_0\mu_0}} \quad (2.15)$$

The index of refraction from Eq. 2.15 stands for the real part of the complex description of the refractive index, which will be later discussed in Section 2.4. For the nonmagnetic

materials $\mu \approx \mu_0$, therefore, the index of refraction is determined mainly by the medium permittivity, ϵ , which is related to the electromagnetic wave frequency.

2.2.3 Fiber attenuation

The attenuation of the optical fiber is a crucial characteristic as it determines the information capacity in fiber optic telecommunication systems. When the power of the incident signal, P_0 , is launched to the fiber of a length L , the output power, P_t , is determined as:

$$P_t = P_0 \exp(-\alpha L), \quad (2.16)$$

where α represents the attenuation constant. The fiber attenuation is usually expressed in dB/km with the use of the relation:

$$\alpha_{\text{dB}} = -\frac{10}{L} \log \left(\frac{P_t}{P_0} \right). \quad (2.17)$$

For pure silica, the attenuation is below 1 dB/km in the wavelength range of 0.8-1.8 μm . Below 0.8 μm and beyond 1.8 μm , the attenuation significantly increases. The attenuation spectra for $\text{GeO}_2\text{-SiO}_2$ fiber is depicted in Figure 2.1. The attenuation minima are around 1.3 μm and 1.55 μm , the latter as low as 0.2 dB/km. These two spectral bands correspond to windows widely used in telecommunication systems.

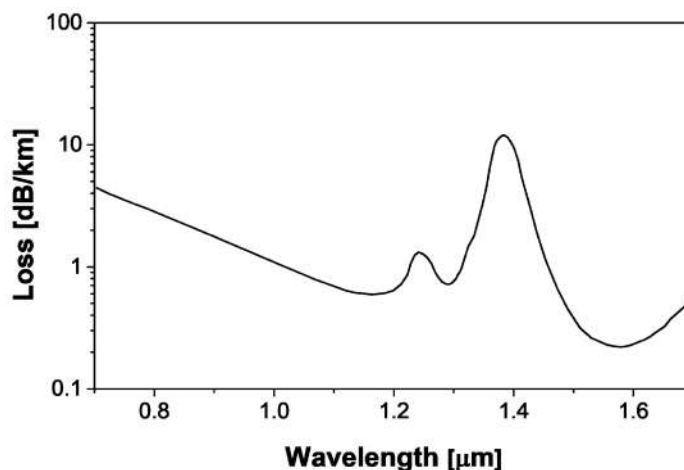


Figure 2.1: Spectral attenuation profile of a standard $\text{GeO}_2\text{-SiO}_2$ fiber [20].

There are several factors that contribute to fiber loss, whose spectrum is presented in Figure 2.1. The leading cause is material absorption and Rayleigh scattering. These effects are absorbed by silica glass, especially in the ultraviolet region and beyond the 2 μm due to the electronic and vibrational resonances of the silica. Nevertheless, even small impurities can lead to an increase in the absorption within the wavelength range of 0.5-2 μm . The Rayleigh dispersion is a consequence of variations in the material density. Consequently, random fluctuations of the refractive index arise, which lead to light scattering. The effect changes with λ^{-4} and is more significant for shorter wavelengths. The local attenuation

minimum at $1.55 \mu\text{m}$ is mostly a result of Rayleigh scattering.

Another loss contribution which is particularly hard to eliminate is the hydroxyl group, OH, which results from water vapor. The main water absorption peak is located at $2.73 \mu\text{m}$. The peak near $1.4 \mu\text{m}$, and the smaller around $1.23 \mu\text{m}$, which are visible in Figure 2.1, correspond to the higher harmonics of the OH-absorption peak. The fiber fabrication process is performed with special precautions to keep the OH-ion contribution at the level below one part in one hundred million [21].

2.2.4 Chromatic dispersion

When considering different phenomena and factors affecting the pulse in an optical fiber, dispersion would be by far the most important. The definition of chromatic dispersion describes it as a frequency (ω) dependence of a refractive index $n(\omega)$ that originates from an interaction between the electromagnetic wave and the bound electrons of a dielectric [22]. Dispersion is a critical factor, especially for ultrashort pulses, as it leads to the situation when different frequency components travel with different speeds (given by $c/n(\omega)$). Mathematically, the effect of chromatic dispersion on the propagating pulse can be explained by expanding the mode-propagating constant β into the Taylor series:

$$\beta(\omega) = n(\omega)\frac{\omega}{c} = \beta_0 + \beta_1(\omega - \omega_0) + \frac{1}{2}\beta_2(\omega - \omega_0)^2 + \dots, \quad (2.18)$$

where

$$\beta_m = \left(\frac{d^m \beta}{d\omega^m} \right)_{\omega=\omega_0} \quad (m = 1, 2, 3 \dots). \quad (2.19)$$

Terms β_1 and β_2 are directly associated with the refractive index through the relation:

$$\beta_1 = \frac{1}{\nu_g} = \frac{n_g}{c} = \frac{1}{c} \left(n + \omega \frac{dn}{d\omega} \right) \quad (2.20)$$

$$\beta_2 = \frac{1}{c} \left(2 \frac{dn}{d\omega} + \omega \frac{d^2 n}{d\omega^2} \right) \quad (2.21)$$

where symbols n_g and ν_g refer to group index and group velocity, respectively. The interpretation of the ν_g refers to the situation where the pulse envelope moves with the velocity of $\nu_g = c/n_g$, and the parameter β_2 accounts for the dispersion of the group velocity, named as Group Velocity Dispersion (GVD). The GVD usually serves as an individual parameter which is expressed in ps^2/km or fs^2/km . The GVD is associated with another dispersion parameter, D , widely used in optical communication systems:

$$D = -\frac{2\pi c}{\lambda^2} \beta_2, \quad (2.22)$$

where λ denotes the wavelength. The parameter D is usually expressed in $\text{ps}/\text{nm}\cdot\text{km}$. Both values, β_2 and D , reach zero for the wavelength of $\approx 1.31 \mu\text{m}$ (for standard telecommunication fiber, SMF28) and change sign for wavelengths above that value. This specific

wavelength is referred to as *zero-dispersion wavelength* (ZDW) and denoted as λ_D . For the wavelengths near to ZDW value, the dispersion impact on the pulse does not disappear. In this region, the impact of other term: Third-Order Dispersion (TOD) coefficient β_3 should be taken into account. The impact of the TOD and other higher-order dispersion parameters can include pulse distortions in both linear [22] and nonlinear [23] regimes, and it needs to be considered for the ultrashort pulses or in the vicinity of ZDW.

Total dispersion also includes the impact of the waveguide dispersion, which results from the difference between the refractive index of the core and the cladding. Because the contribution of the waveguide dispersion to the total dispersion depends on fiber design parameters (such as core radius or difference between the core/cladding refractive indexes), it can actually allow for changing the dispersion profiles, namely shifting the ZDW for longer wavelengths. This feature is widely used in fiber optic systems to manufacture fibers with dispersion tailored for specific applications. Fibers with the ZDW shifted to the 1.55 μm are called *dispersion-shifted fibers* (DSF) and are often employed for long-haul optical fiber systems. Fibers with large positive values of β_2 are called *dispersion-compensating fibers* (DCF) and are utilized, e.g., in optical amplifiers for dispersion compensation. The dispersion profiles (for both GVD and D) of SMF, DSF and DCF are presented in Figure 2.2.

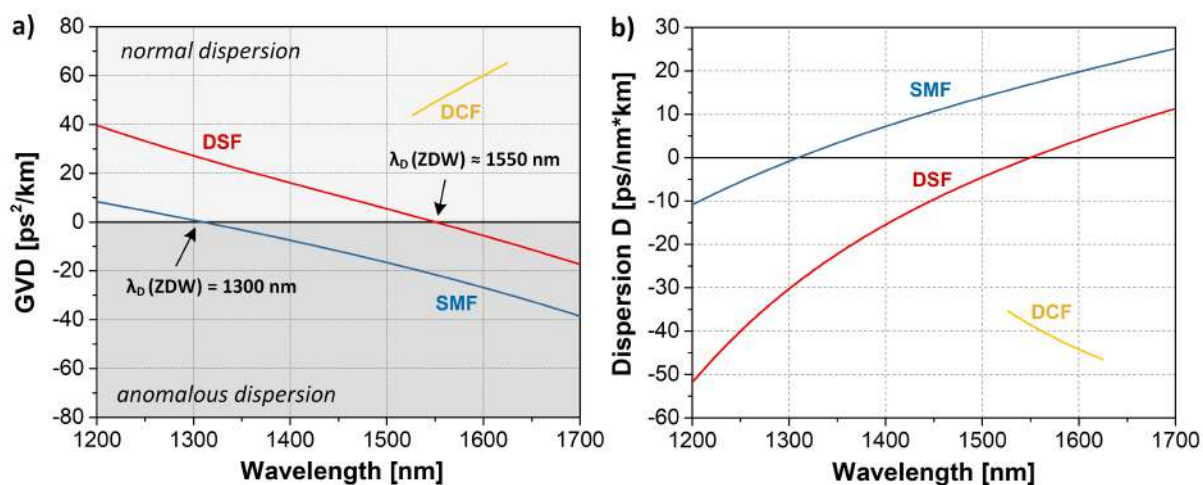


Figure 2.2: Examples of dispersion profiles for standard single-mode fiber (SMF), dispersion-shifted fiber (DSF) and dispersion-compensating fiber (DCF): (a) GVD parameter, (b) dispersion parameter, D . The anomalous dispersion regime corresponds to the region of $\text{GVD} < 0$, whereas the normal dispersion regime describes the wavelength region of $\text{GVD} > 0$.

The λ_D parameter is used to define two regions: *normal* and *anomalous* dispersion (or *positive* and *negative*) depending on the sign of the GVD parameter. The anomalous (negative) dispersion regime refers to the wavelength region below the λ_D , and the *normal* (*positive*) dispersion refers to the wavelengths above the λ_D . It can be observed from Equation 2.22 that D possesses the opposite value to β_2 .

In the presence of dispersion, namely GVD, different frequency components propagate at different speeds and hence, arrive at different times. The relative delay Δt_D , which

corresponds to the difference in arrival time of frequency components ω_1 and ω_2 after propagating distance z :

$$\Delta t_D = \frac{z}{\nu_g(\omega_1)} - \frac{z}{\nu_g(\omega_2)} = \frac{(d\nu_g/d\omega)(\omega_2 - \omega_1)z}{\nu_g^2} \quad (2.23)$$

Since β_2 can be described as:

$$\beta_2 = -\frac{d\nu_g/d\omega}{\nu_g^2}, \quad (2.24)$$

the delay time can be expressed as:

$$\Delta t_D = -\beta_2(\omega_2 - \omega_1)z. \quad (2.25)$$

Equation 2.25 indicates that the difference in arrival time of different frequency components is proportional to the group velocity dispersion, β_2 , the frequency difference $\omega_2 - \omega_1$, and the propagation distance, z . For $\beta_2 < 0$ (anomalous dispersion regime), higher frequency components arrive first, whereas in case of $\beta_2 > 0$ (normal dispersion regime), the situation is opposite. This effect is described as a *frequency chirp* that a pulse can acquire after propagating inside a fiber and is graphically described in Figure 2.3. After propagating in the fiber with an anomalous dispersion profile, the pulse acquires a negative chirp, whereas, in case of propagation in normal dispersion fiber, the acquired chirp is positive.

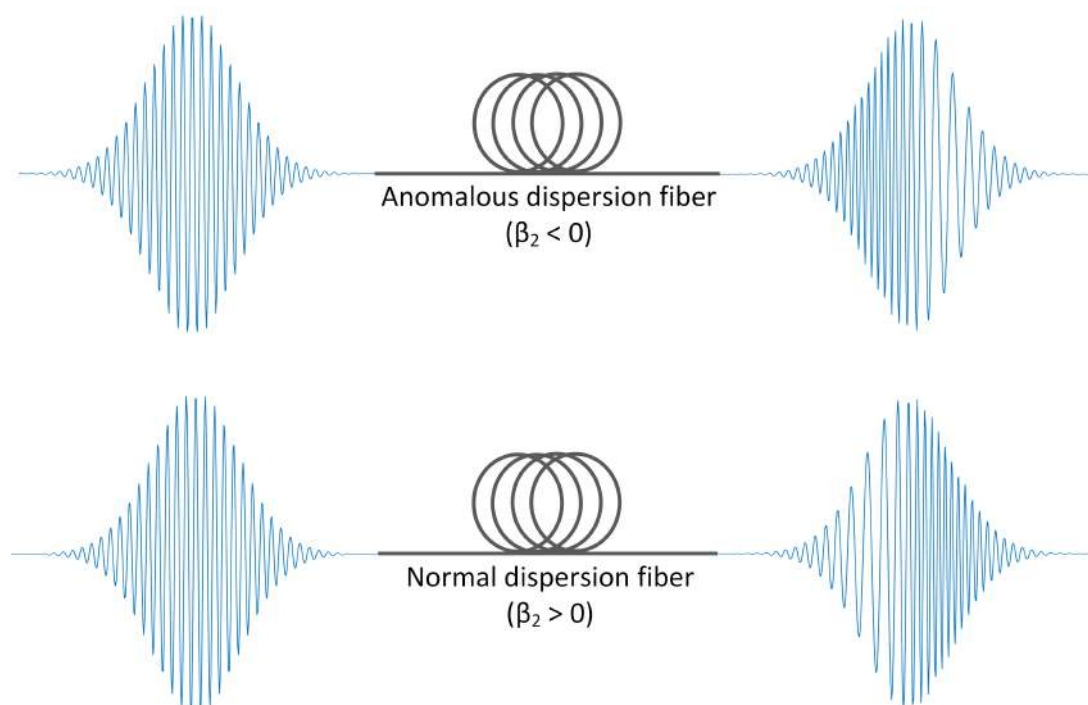


Figure 2.3: An illustration of acquiring chirp by the laser pulse after propagating in the fiber with anomalous and normal dispersion.

It will be described in the next Section that the impact of the nonlinear effects on the propagating pulse is strictly dependent on the GVD of the fiber. The anomalous dispersion regime has attracted attention due to the fact that this regime supports

soliton formation. Recently also the normal dispersion happened to become useful to adapt low-noise supercontinuum generation. Both these effects will be later analyzed comprehensively.

Dispersion compensation

As it has already been mentioned, standard SMF possesses zero dispersion wavelength at $1.33 \mu\text{m}$. Therefore, laser systems operating in the telecommunication window at $1.55 \mu\text{m}$ are characterized by negative dispersion, β_2 . In the presence of dispersion, the unchirped pulse gets broadened. When a pulse at $1.55 \mu\text{m}$ propagates in a conventional fiber characterized by anomalous dispersion ($\beta_2 < 0$), the pulse leading edge is blueshifted, whereas the trailing edge is redshifted (which corresponds to rising the instantaneous frequency with time). If such a pulse is launched to a fiber of adjusted length and a normal dispersion regime ($\beta_2 > 0$), the pulse can be compressed back to its original temporal duration. This process is known as *dispersion compensation*. This technique is widely used, e.g., in chirped-pulse amplification systems to stretch and compress laser pulses.

2.3 Generalized Nonlinear Schrödinger Equation

Studies on nonlinear effects that occur in optical fibers usually implement short laser pulses of a duration shorter than 10 ps. When such short pulses are provided to an optical fiber, they are affected by both dispersion of the fiber and nonlinear effects. The general equation that includes both linear and nonlinearities for pulse propagation is described as a Generalized Nonlinear Schrödinger Equation (GNLSE), and for ultrashort pulses (< 5 ps), it takes the form:

$$\frac{\partial A}{\partial z} + \frac{\alpha}{2}A + \frac{i\beta_2}{2} \frac{\partial^2 A}{\partial t^2} - \frac{\beta_3}{3} \frac{\partial^3 A}{\partial t^3} = i\gamma \left(|A|^2 A + \frac{i}{\omega_0} \frac{\partial}{\partial t} (|A|^2 A) - T_R \frac{\partial |A|^2}{\partial t} \right), \quad (2.26)$$

where A corresponds to a slowly varying pulse envelope, α describes fiber losses, terms: β_2 and β_3 represent chromatic dispersion coefficients, γ is a nonlinear coefficient, T_R defines Raman response function, and t and z refer to time and propagation distance, respectively. The GNLSE is a fundamental equation in nonlinear optics and has been widely used to study ultrashort pulse propagation in optical fibers, especially optical solitons [13, 24–27], that will be described better in the next Section.

For pulses of a duration $t_0 > 5$ ps, the parameters $(\omega_0 t_0)^{-1}$ and T_R/t_0 become negligible, and therefore the last two terms of the Eq. 2.26 can be eliminated. The contribution of third-order dispersion for longer pulses also plays a minor role (assuming that the operating wavelength is not in the close area of ZDW), therefore the equation can be simplified to a form:

$$i \frac{\partial A}{\partial z} + \frac{i\alpha}{2} A - \frac{\beta_2}{2} \frac{\partial^2 A}{\partial t^2} + \gamma |A|^2 A = 0. \quad (2.27)$$

Equation 2.27 is often called the Nonlinear Schrödinger Equation (NLSE), and is very useful for performing the investigation of third-order nonlinear phenomena in optical fibers.

The NLSE provides a general description of a pulse propagating in a fiber when being influenced by both GVD and fiber nonlinearities. To properly investigate these factors, a good way is to propose the approach of considering only one type of the phenomena (linear or nonlinear) and neglecting the latter simultaneously. The following subsections will consider and analyze particular versions of Eq. 2.27.

2.3.1 Pulse propagation in the presence of dispersion only

First, let us consider the NLSE by treating the fiber as a linear medium where there are no nonlinear effects. By also neglecting the fiber attenuation, Eq. 2.27 takes now the form:

$$i\frac{\partial A}{\partial z} - \frac{1}{2}\beta_2\frac{\partial^2 A}{\partial \tau^2} = 0. \quad (2.28)$$

The general solution to this equation is as follows:

$$A(z,t) = \int_0^\infty A(0,\omega)e^{i((1/2)\beta_2\omega^2z - \omega\tau)}d\omega, \quad (2.29)$$

where $A(0,\omega)$ refers to the frequency spectrum of the pulse. The equation above can be transformed to the form describing the electric field of a Gaussian pulse E of an amplitude E_0 , where each spectral component propagates over distance z with propagation constant $\beta(\omega)$ acquiring phase variation $\beta(\omega)z$. Therefore, at z , the electric field is:

$$E(z,t) = \int_{-\infty}^{+\infty} E(0,\omega)\exp\{i[\beta(\omega)z - \omega t]\}d\omega. \quad (2.30)$$

By providing the Taylor series expansion of the propagation constant $\beta(\omega)$ from Eq. 2.18 and keeping terms up to second order in the term $(\omega - \omega_0)$ it can be expressed as [20]:

$$E(z,t) = \frac{E_0}{(1 + \sigma^2)^{1/4}} \exp\left\{-\frac{(t - z/\nu_g)^2}{2t_p^2(z)}\right\} \exp\{i[\beta_0z - \phi(z,t)]\}, \quad (2.31)$$

where ν_g refers to group velocity, t_p describes the half-width of the pulse, and the phase shift ϕ can be expressed with the use of additional parameters: κ and σ :

$$\phi(z,t) = \omega_0 t + \kappa \left(t - \frac{z}{\nu_g}\right)^2 - \frac{1}{2}\text{tg}^{-1}(\sigma), \quad (2.32)$$

$$\kappa = \frac{\sigma}{2(1 + \sigma^2)t_0^2}, \quad (2.33)$$

$$\sigma = \frac{\beta_2 z}{t_0^2}, \quad (2.34)$$

$$t_p^2(z) = t_0^2(1 + \sigma^2). \quad (2.35)$$

Equation 2.32 indicates that the pulse phase is varied quadratically with time. Consequently, the instantaneous frequency, ω also varies across the pulse and differs from the central frequency ω_0 . The instantaneous frequency can be estimated by simply calculating the time

derivative of the phase:

$$\omega(t) = \frac{\partial \phi}{\partial t} = \omega_0 + 2\kappa\left(t - \frac{z}{v_g}\right). \quad (2.36)$$

The Equation above shows that the frequency varies linearly across the pulse and with the propagation in the fiber the pulse acquires linear frequency chirp. The chirp depends on the sign of β_2 . In the normal dispersion regime (when $\beta_2 > 0$, so $\kappa > 0$), the instantaneous frequency increases with time which corresponds to linear positive chirp. In case of anomalous dispersion ($\kappa < 0$), the situation is opposite.

In Eq. 2.35 the parameter t_0 corresponds to half-width at $1/e$ intensity point which is related to the FWHM as:

$$t_{\text{FWHM}} = 2(\ln 2)^{1/2} t_0 \approx 1.665 t_0. \quad (2.37)$$

Equation 2.35 indicates that half-width of the pulse $t_p(z)$ is proportional to the propagation distance z , and its increase is determined by the GVD parameter, β_2 . Here another parameter can be defined: a *dispersion length*, L_D , which corresponds to the distance over which a Gaussian pulse is broadened to $\sqrt{2}$ times the initial pulse width t_0 .

$$L_D = \frac{t_0^2}{|\beta_2|}. \quad (2.38)$$

The impact of the GVD on a laser pulse propagating inside the optical fiber is illustrated in simulation in Figure 2.4. To perform the numerical simulations, a split-step Fourier method was used, which is going to be more deeply described in Section 2.5. Let's consider a sech-shaped pulse of a duration of 5 ps propagating in a 25 km-length SMF fiber. To investigate the GVD impact on the pulse we neglect any nonlinearities and fiber loss. The initial peak power is 20 mW and the value of β_2 amounts to $-20 \text{ ps}^2/\text{km}$. Figure 2.4 presents the evolution of the pulse temporal shape (a) and frequency spectrum (b). It is observed that the GVD leads to pulse broadening without affecting pulse spectrum.

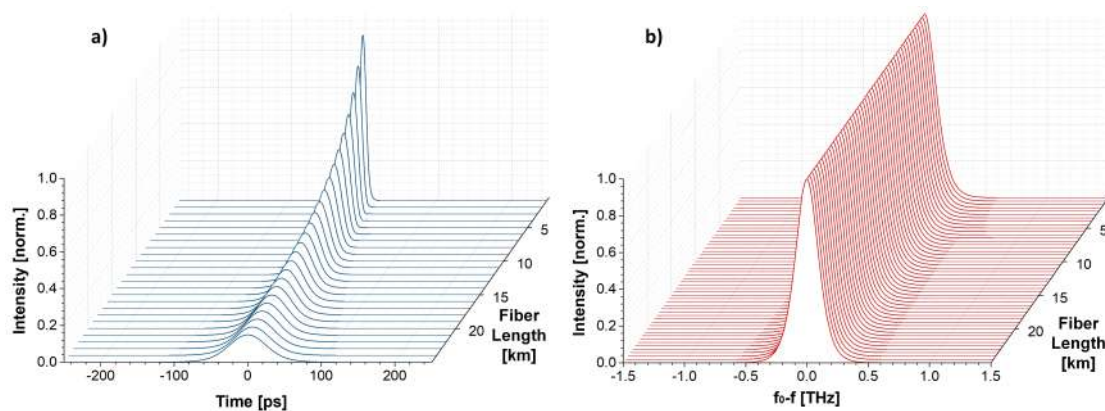


Figure 2.4: A pulse propagation in the optical fibers when neglecting the nonlinearities; (a) temporal pulse shape evolution, (b) pulse spectrum evolution.

2.3.2 Pulse propagation in the presence of nonlinearities only

In the situation where only fiber nonlinearities (represented by the nonlinear coefficient γ) are considered and other effects neglected, the pulse propagation can be described with a formula:

$$i\frac{\partial A}{\partial z} + \gamma|A|^2 A = 0. \quad (2.39)$$

By multiplying the above equation by A^* and its complex conjugate by factor A and eventually subtracting both equations, one can obtain [20]:

$$\frac{\partial|A|^2}{\partial z} = 0. \quad (2.40)$$

The general solution to the Eq. 2.40 is:

$$|A|^2 = f(\tau) = f(t - z/\nu_g). \quad (2.41)$$

These results demonstrate that if we neglect the linear effects and consider only fiber nonlinearity, the absolute square of the pulse envelope maintains its shape with propagation. Taking this into account, one can write Eq. 2.40 in the form:

$$A(z,t) = A_0(\tau)e^{i\phi(z,t)}, \quad (2.42)$$

where $A_0(\tau)$ and $\phi(z,t)$ are both real functions. From Equations 2.39 and 2.42, one can obtain:

$$\phi(z,\tau) = \gamma|A_0(\tau)|^2 z, \quad (2.43)$$

which shows that the fiber nonlinearity provides phase modulation, which is proportional to the intensity of the pulse and propagation distance. This phenomenon is known as *self-phase modulation* and will be described in Section 2.4.

Figure 2.5 presents the simulation of the pulse propagation inside an optical fiber when only nonlinearities affect the pulse (we neglect the dispersion). The variation in the pulse spectrum is clearly visible in Figure 2.5 b), whereas Figure 2.5 a) shows no change in the pulse's temporal shape. It can be easily noticed that the modulation of the spectrum induced by nonlinearities increases with the propagation length. As a consequence, new frequency components are generated along the propagation distance. The nonlinear effects, that can occur in an optical fiber, consist of a wide variety of phenomena, such as SPM (which is probably the most important one), modulation instability, cross-phase modulation, four-wave mixing, stimulated Raman scattering or stimulated Brillouin scattering. Some of them are going to be described in details in the next Section. A consideration of both, dispersion and nonlinearities, affecting the propagating pulse in a fiber is given in Section 2.4.2.

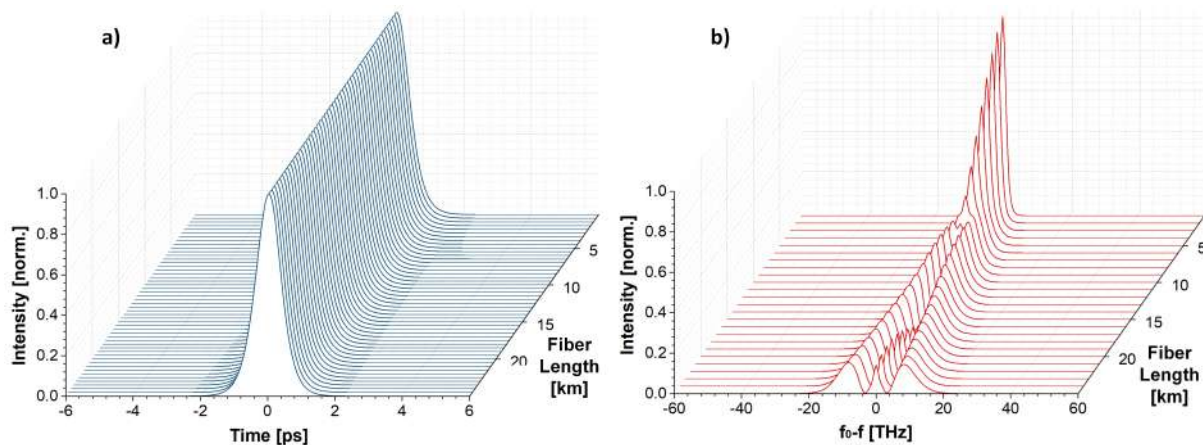


Figure 2.5: A pulse propagation in the optical fibers when neglecting the fiber dispersion; (a) temporal pulse shape evolution, (b) pulse spectrum evolution.

2.4 Fundamentals of nonlinear phenomena

A response to any electromagnetic field can become nonlinear for sufficiently high power levels of the signal. On the fundamental level, the nonlinear response originates from the anharmonic motions of bound electrons when the electric field is applied. As a consequence, the relation between the total polarization \mathbf{P} and the electric field \mathbf{E} becomes more complex as described with the formula [15, 28]:

$$\mathbf{P} = \epsilon_0(\chi^{(1)} \cdot \mathbf{E} + \chi^{(2)} \cdot \mathbf{E}\mathbf{E} + \chi^{(3)} \cdot \mathbf{E}\mathbf{E}\mathbf{E}), \quad (2.44)$$

where ϵ_0 describes vacuum permittivity and $\chi^{(n)}$ corresponds to n-th order susceptibility. Generally, $\chi^{(n)}$ is a tensor with a rank of $n+1$. The term $\chi^{(1)}$ represents the linear susceptibility and also determines the significant contribution to the polarization \mathbf{P} . The effects of $\chi^{(1)}$ manifest through the attenuation coefficient α and refractive index n . The second-order susceptibility $\chi^{(2)}$ accounts for nonlinear effects such as second-harmonic generation and sum-frequency generation [29]. It is also non-zero only for media that lack molecular symmetry. As the silica (SiO_2) is a symmetric molecule, optical fibers do not usually exhibit nonlinear effects related to second-order susceptibility. However, the second-order nonlinear effects can arise in the optical fiber under certain conditions induced by such events like electric quadrupole or magnetic dipole moments. They can also be generated by defects and colour centres in the fiber core.

Therefore, the nonlinear effects that generally are generated in optical fibers are usually related to third-order susceptibility $\chi^{(3)}$. These include nonlinear refraction, third-harmonic generation and four-wave mixing [29]. However, the third-harmonic generation and four-wave mixing require phase-matching, otherwise, they usually feature very low efficiency. Therefore, the majority of nonlinear effects originate from the nonlinear refractive index. The refractive index n can be described in the simplest form by a formula [6]:

$$n(\omega, I) = n(\omega) + n_2 I = n + n_2 |E|^2, \quad (2.45)$$

where $n(\omega)$ is a linear term, I describes an optical intensity that is directly associated with the electromagnetic field E , and n_2 refers to a nonlinear refractive index. The typical values of n_2 for silica fibers fall between $2.2 - 3.4 \times 10^{-20} \text{ m}^2/\text{W}$ [6]. This magnitude can change depending on the core doping or preserving linear polarization [30]. Comparing to other optical media, the values of the refractive index for silica fibers are much smaller (by two orders of magnitude or more). Despite such low values of n , relatively low power levels are sufficient to observe the nonlinear effects in the optical fibers. It is because optical fibers are characterized by small spot size (mode field diameter less than $10 \mu\text{m}$) and low loss transmission ($<1 \text{ dB/km}$).

2.4.1 Self-phase modulation

Equation 2.45 informs that the refractive index increases with the increase of the light intensity. Although the variation in the n value is extremely small, when a pulse propagates in the fiber over a long distance (even up to hundreds of kilometers), the effects resulting from this behaviour can be significant. Considering that the phase of the light beam depends on n and the light beam itself provides changes to n and therefore changes its own phase. This phenomenon is described as self-phase modulation because the phase change is self-induced.

SPM-induced Phase Shift

In order to mathematically describe the SPM effect in optical fibers, the numerical solution of the equation for pulse propagation from the previous Section is required. By assuming the pulse propagation length (fiber length) is much lower than the dispersion length L_D , one can neglect the dispersive term in Eq. 2.27 ($\beta_2 = 0$) and obtain the reduced form of the NLSE:

$$\frac{\partial A}{\partial z} = i\gamma P A, \quad (2.46)$$

where $P = |A|^2$ and represents the pulse power. If we neglect the fiber loss, then P corresponds to the pulse input power. The general solution for Eq. 2.46 at the fiber length L is:

$$A(L, \tau) = A(0, \tau) \exp[i\phi_{\text{NL}}(L, \tau)], \quad (2.47)$$

where $A(0, \tau)$ describes the input pulse envelope and ϕ_{NL} refers to the nonlinearity-induced phase variation, which can be described as:

$$\phi_{\text{NL}}(L, \tau) = \gamma P(\tau) L \quad (2.48)$$

Equation 2.47 shows that the SPM increases the intensity-dependent phase shift, but, at the same time, it does not affect the shape of the pulse.

By using Eq. 2.47, one can find the formula for the electric field propagated in the fiber:

$$E(L, t) = \frac{1}{2} [\hat{E}(0, \tau) \exp\{i[(\beta_0 + \gamma P)L - \omega_0 t]\} + c.c.], \quad (2.49)$$

where ω_0 corresponds to the central frequency of the pulse. Equation 2.49 describes the wave which phase is:

$$\phi = (\beta_0 + \gamma P)L - \omega_0 t. \quad (2.50)$$

The above equation shows that variation in the phase that is induced by the fiber nonlinearities depends on the power of the wave. If the incident pulse possesses power temporal profile $P(t)$, the variation in power leads to the modulation in the pulse's phase. Spectral changes that are caused by the SPM directly result from the time dependence of ϕ_{NL} . The instantaneous frequency of the pulse described by Eq. 2.49 is, as previously, a derivative of the pulse's phase:

$$\omega(t) = -\frac{\partial \phi_{\text{NL}}}{\partial t} = \omega_0 - \gamma L \frac{\partial P}{\partial t} \quad (2.51)$$

According to Eq. 2.51, the instantaneous frequency first decreases with the increasing power of the pulse. Next, for the pulse maximum, $\omega(t)$ reaches the central frequency, and eventually increases for decreasing values of pulse power. This time dependence of the frequency difference $\Delta\omega_{\text{SPM}} = \omega(t) - \omega_0$ is called *frequency chirping*.

Figure 2.6 presents an electric field variation of an optical pulse. The oscillations that are observed in the pulse result from the high frequency of the signal. It can also be noticed that the envelope of the pulse (which is defined as the pulse shape) possesses much lower variation in time. The intensity of the leading and trailing edge of the pulse is significantly

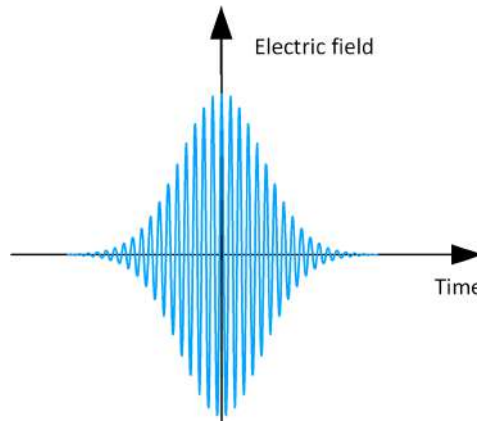


Figure 2.6: Pulse electric field.

smaller than the intensity at the centre of the pulse. Therefore, since the refractive index is intensity dependent, the centre of the pulse would exhibit a stronger variation of the refractive index than its trailing and leading edge. The response time of the medium to intensity changes is very short, almost instantaneous, therefore, the response time of the refractive index to the change in the intensity change is also extremely short. Taking into account that the speed of propagation in the optical fiber depends on the refractive index of the fiber, the centre of the pulse would experience slowing down when compared to pulse ends. As a consequence, the front end of the pulse exhibits a lower frequency, whereas the back end features a higher frequency. Such a pulse is called a *chirped pulse*.

The SPM effect on a pulse is demonstrated graphically in Figure 2.7. Figure 2.7 a)

presents the electric field of the optical pulse without the change in phase. Figures 2.7 b) and c) demonstrate the optical pulse after propagation through the nonlinear medium. It is observed that the optical pulse acquires nonlinear phase shift ϕ_{max} which magnitude is determined by the nonlinearity of the medium and the pump power [6]. It is easily noticed that the greater value of ϕ_{max} , the stronger frequency change between the pulse trailing and leading edge is observed.

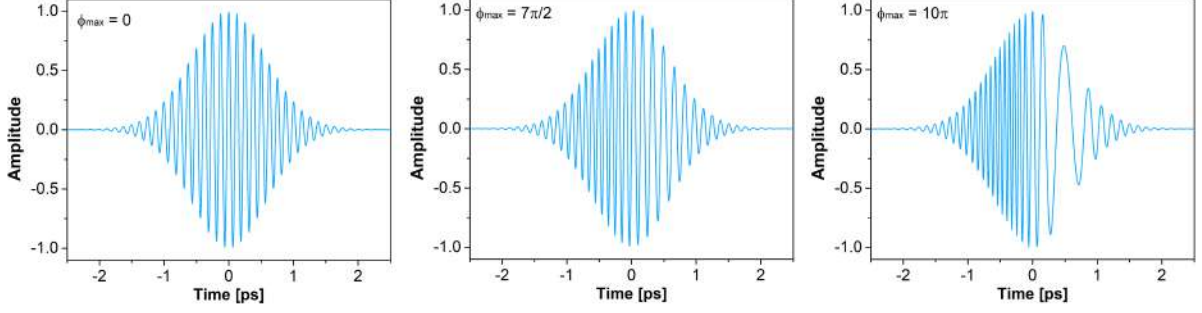


Figure 2.7: Pulse electric field: without phase change (a); with the phase change $\phi_{max} = 7\pi/2$ (b); with the phase change $\phi_{max} = 10\pi$ (c).

2.4.2 Soliton solution

In this Section, pulse propagation is considered for both dispersion and nonlinearities affecting the pulse. For this purpose, let us provide the normalized version of the NLS Equation (Eq. 2.27). For short segments of fiber, one can assume the neglect of the fiber losses ($\alpha = 0$) and provide a few new parameters:

$$U = \frac{A}{\sqrt{P_0}}, \quad \xi = \frac{z}{L_D}, \quad \tau = \frac{t}{t_0}, \quad (2.52)$$

where t_0 describes the initial pulse width, P_0 refers to pulse peak power, and L_D defines the dispersion length, which was already provided as: $L_D = t_0^2/|\beta_2|$. Now the NLS Equation takes the form:

$$i\frac{\partial U}{\partial \xi} - \frac{\delta_2}{2}\frac{\partial^2 U}{\partial \tau^2} + N^2|U|^2U = 0, \quad (2.53)$$

where $\delta_2 = \text{sgn}(\beta_2) = \pm 1$ and the parameter N is expressed as:

$$N^2 = \frac{L_D}{L_{NL}} = \frac{\gamma P_0 T_0^2}{|\beta_2|}. \quad (2.54)$$

Parameters L_D and L_{NL} define dispersion and nonlinear lengths, respectively. The nonlinear length, L_{NL} is the length of propagation required to provide a nonlinear phase change rotation equivalent to one radian at a power P_0 . L_{NL} is expressed as:

$$L_{NL} = \frac{1}{\gamma P_0} \quad (2.55)$$

These two length scales: L_D and L_{NL} , are characteristic distances over which the dispersive or nonlinear effects determine pulse evolution.

The analytical description and simulations of the pulse behaviour presented in previous sections concentrated on either the dispersion or the SPM effects separately. However, it is necessary to take into consideration both effects at the same time. First of all, both the spectrum and the pulse shape can change as the pulse propagates inside the fiber. The situation is different depending on the dispersion regime. When the fiber dispersion is normal ($\beta_2 > 0$), the pulse gets broadened with propagation. However, in the case of anomalous dispersion ($\beta_2 < 0$), under certain conditions of the pulse peak power and shape, the nonlinear effects are able to compensate for the dispersive effects, and the pulse propagates without change in shape and spectrum. Such a pulse is called a *soliton*. The term soliton refers to a wave packet that does not change its shape along the propagation.

To analyze the soliton formation, the parameter δ_2 should be set: $\delta_2 = -1$ ($\beta_2 < 0$) in Eq. 2.53 to provide an anomalous dispersion regime. The NLS equation can be solved with the inverse scattering method and for $N = 1$, the solution of the NLS takes the form:

$$U(\xi, \tau) = \eta \operatorname{sech}(\eta\tau) \exp(i\eta^2\xi/2), \quad (2.56)$$

where η corresponds to the arbitrary parameter, which describes both the soliton amplitude and its width. The above solution is a representation of a fundamental soliton. As the pulse width changes with η in a manner t_0/η , it is inversely proportional to the pulse amplitude. This relation between the pulse width and amplitude is a characteristic feature of fundamental solitons.

One can obtain the canonical form of the fundamental soliton by setting $\eta = 1$ so that the input field is:

$$U(0, \tau) = \operatorname{sech}(\tau). \quad (2.57)$$

Now, the pulse evolution can be described as:

$$U(\xi, \tau) = \operatorname{sech}(\tau) \exp(i\xi/2), \quad (2.58)$$

indicating that only the pulse phase is changed along the propagation, therefore, both the pulse spectrum and the temporal shape should remain the same. The peak power that is required for fundamental soliton (for which the soliton order, N , is set to 1) is determined by the formula:

$$P_0 = \frac{|\beta_2|}{\gamma T_0}. \quad (2.59)$$

Taking this into consideration, let us assume a fundamental soliton propagating in a 1 km fiber length. When considering typical values at 1.55 μm , $\beta_2 = -20 \text{ ps}^2/\text{km}$ and $\gamma = 1.3 \text{ W}^{-1}/\text{km}$, the required peak power is $\approx 15 \text{ W}$ for 1 ps pulse. The propagation of such a pulse is presented in Figure 2.8. One can quickly notice that neither the pulse shape nor the frequency spectrum gets changed along the propagation. The nonlinear phase shift provided by the SPM is cancelled by the linear phase shift caused by the GVD, which

results in an unperturbed propagation along the fiber.

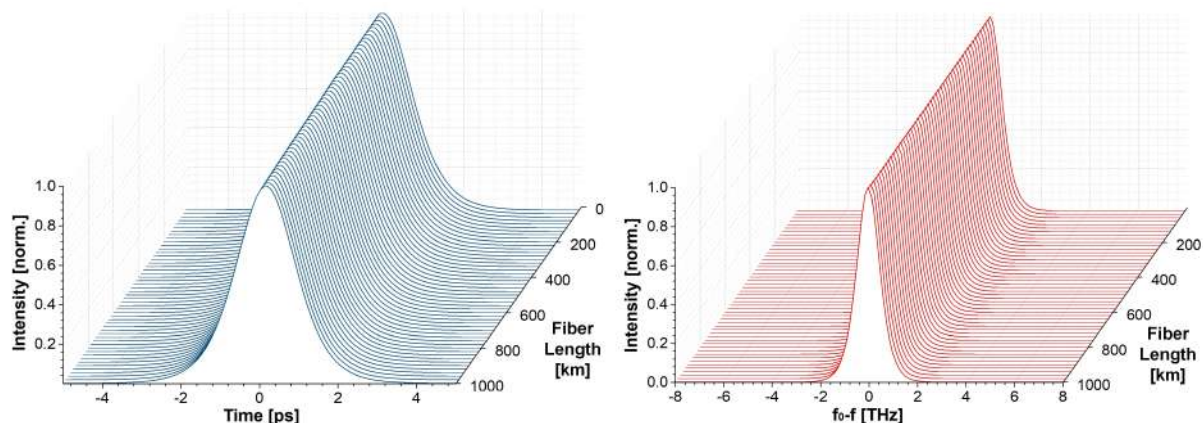


Figure 2.8: A soliton propagation in an optical fiber; (a) temporal pulse shape evolution, (b) pulse spectrum evolution.

Since the discovery, optical solitons have significantly impact optics. Solitons are widely used in optical fiber communication systems as they allow for the high information capacity of the system [31, 32]. They can also be utilized in mode-locked fiber lasers. The remarkable advantage of the soliton is its stability which is a consequence of the fact that the solutions to the nonlinear wave equations are, in general, very stable. Solitons travelling inside the optical fiber are prone to small perturbances that may affect it along the propagation. If the initial pulse shape or its power is not ideally matched (as in Equation 2.59) and the input pulse is not initially a fundamental soliton, it still can form into a soliton as long as the value of N is close to 1 and the pulse is bell-shaped. As a consequence, the pulse evolves gradually and adjusts the shape to the sech-shape of the soliton [6]. Specifically, the soliton forms when the N value is between 0.5 and 1.5 [16]. An interesting feature is that solitons can form even when the Kerr nonlinearity and dispersion appear in discrete forms in the fiber, and the energy inside the fiber varies as a result of pulse amplification and loss of other fiber components [33].

Dissipative solitons

A situation where the soliton is formed without the exchange of energy with the fiber is related to the so-called *conservative solitons*. However, localized solutions can occur even when dissipative effects arise. In fact, in the 1990s, scientist discovered that solitary waves could be formed in a wide variety of non-conservative systems [34]. These solutions, possible to be generated in nonlinear optical systems with different mechanisms based on nonlinear gain or loss, were later called *dissipative solitons*. In such systems, the balance between dispersive and nonlinear phenomena is being replaced by the balance of the effects including dispersion or diffraction, gain, loss and nonlinearity [35]. As a consequence, solitary waves can be found in systems with normal dispersion regime (so-called bright dissipative solitons) [36] or as multisoliton complexes known as soliton molecules [37].

Higher-order solitons

When the initial pulse energy is n ($n \geq 2$) times the energy of a fundamental soliton, the pulse is formed into a *higher-order soliton*. A higher-order soliton occurs for $N > 1.5$ and propagates by periodically changing its shape and spectrum. The example of propagation for second- and third-order soliton along two periods is presented in Figure 2.9. For $N = 2$, the soliton initially contracts, then it splits into two separate pulses, and eventually, it merges back and regains its original shape after one soliton period $\xi = \pi/2$. The pattern is repeated in the fiber over each segment of a length $(\pi/2)/L_D$. For $N = 3$, the soliton evolution is more complex and, in this example, the soliton undergoes splitting in a non-symmetrical pattern. Also, the pulse spectrum evolves into a multipeak structure at some distances. Higher-order solitons of a large number of N can be used to generate supercontinuum as a result of soliton fission in anomalous-dispersion fiber.

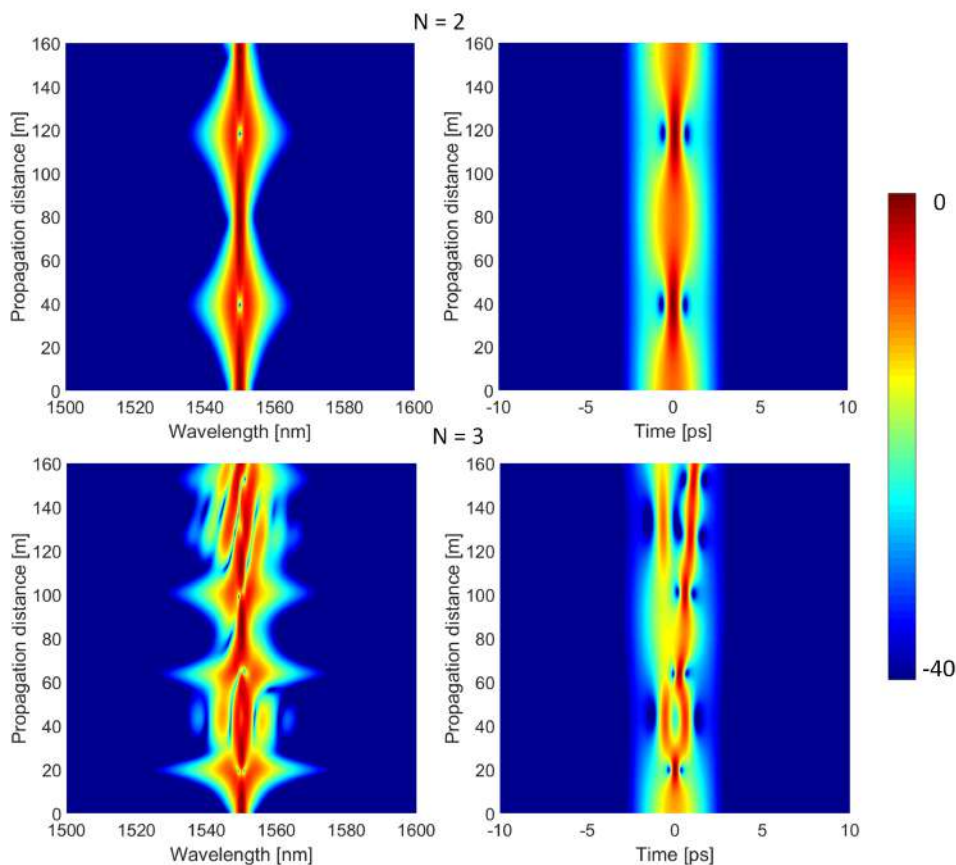


Figure 2.9: Spectral and temporal evolution of second- and third-order soliton. The colour scale describes the spectral density with a 40 dB dynamic range (as presented on the colour bar). Unless stated otherwise, the 40 dB scale applies to all colour scale density plots presented in this Chapter.

2.4.3 Modulation Instability

Nonlinear systems often feature instabilities that result from the interactions between dispersion and fiber nonlinearities. Such instabilities manifest in various spectrum modulations growth of the sideband components. This phenomenon is known as *modulation*

instability [38] and has been investigated since the 1960s in various fields, including nonlinear optics, plasma physics and fluid dynamics.

To mathematically describe this phenomenon, one can consider a one-dimensional light propagation in an optical fiber which was already given by NLS Equation 2.27. When neglecting losses, we can obtain [6, 39]:

$$i\frac{\partial A}{\partial z} = \frac{\beta_2}{2} \frac{\partial^2 A}{\partial t^2} - \gamma |A|^2 A, \quad (2.60)$$

as discussed in Section 2.3, $A(z,t)$ refers to the amplitude of the field envelope, β_2 represents the GVD parameter, and lastly, γ is a nonlinear coefficient responsible for the SPM. Based on this equation, it can be shown relatively simply, that a small perturbation (sinusoidal amplitude modulation) with frequency ω added to the steady state solution is amplified as long as $\beta_2 < 0$ (anomalous dispersion regime) and the perturbation frequency:

$$\omega < \omega_c \equiv \left[\frac{4\gamma P}{|\beta_2|} \right]^{1/2}. \quad (2.61)$$

In these conditions, the solution is unstable and the perturbations rise exponentially with z . This phenomenon is referred to as *modulation instability*.

The gain coefficient of modulation instability can be described as:

$$g(\omega) = |\beta_2 \omega| [\omega_c^2 - \omega^2]^{1/2}. \quad (2.62)$$

Figure 2.10 demonstrates gain spectra for three different optical power levels ($P = 1, 3,$ and 5 kW) for an optical fiber characterized with $\beta_2 = 5$ ps/km and $\gamma = 1.3$ W⁻¹km⁻¹. As can be seen from Figure 2.10, the gain of modulation instability depends on the incident optical power. What is more, the gain spectrum is clearly symmetrical with respect to $\omega = 0$, so that $g(\omega)$ vanishes for $\omega = 0$. The gain reaches a maximum for two frequencies ω_{\max} described as:

$$\omega_{\max} = \pm \frac{\omega_c}{\sqrt{2}} = \pm \left(\frac{2\gamma P}{|\beta_2|} \right)^{1/2}, \quad (2.63)$$

with peak value

$$g_{\max} = g(\omega_{\max}) = \frac{1}{2} |\beta_2| \omega_c^2 = 2\gamma P \quad (2.64)$$

In optical fibers characterized by anomalous dispersion, modulation instability can lead to spontaneous temporal modulation of the light and transforming it into a train of pulses. This phenomenon can also be seeded by the noise added by optical amplifiers. The amplification of this noise can significantly degrade the low-noise properties of the laser system.

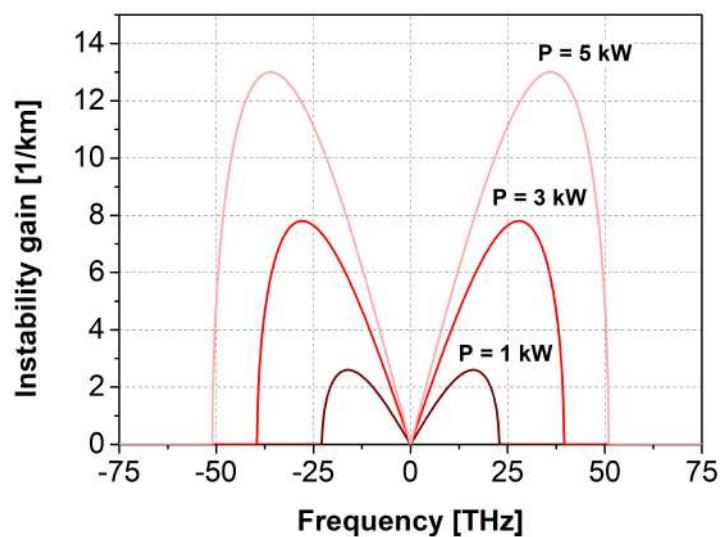


Figure 2.10: Gain spectra of modulation instability for different power levels.

2.4.4 Cross-Phase Modulation (XPM)

When different wavelengths propagate in an optical fiber, they can interact with each other. This feature results from the fact that the refractive index affecting these waves in the fiber depends not only on the intensity of that particular optical beam but also on the intensities of other copropagating waves. As a consequence, an optical beam propagating at one wavelength has an impact on the other optical beam propagating at a different operating wavelength. This phenomenon is known as cross-phase modulation (XPM) and can limit the performance of e.g. WDM (wavelength division multiplexer) systems.

Let us assume two optical fields, E_1 and E_2 , of frequencies ω_1 and ω_2 , polarized along the x -axis, propagating simultaneously inside a fiber. The total electric field \mathbf{E} will be described as [6]:

$$\mathbf{E} = \frac{1}{2} \hat{x} [E_1 \exp(-i\omega_1 t) + E_2 \exp(-i\omega_2 t + \text{c.c.})], \quad (2.65)$$

where the abbreviation c.c. means complex conjugate. The nonlinear phase shift ϕ_{NL} at the frequency ω_1 for the field is given by:

$$\phi_{\text{NL}} = \bar{n}_2 k_0 L (|E_1|^2 + 2|E_2|^2), \quad (2.66)$$

where the terms governing polarization at frequencies other than ω_1 and ω_2 are neglected. Both terms on the right-hand side of Eq. 2.66 result from the contribution of SPM and XPM, respectively. It can be noticed that, for optical field intensities at the same level, the impact of the XPM is twice as the SPM. In optical fibers, the XPM, in combination with SPM and GVD, can lead to asymmetrical spectral broadening or temporal modifications of the propagating pulse. The XPM-induced nonlinear coupling between two propagating beams can result in modulation instability, even in a normal dispersion regime. In WDM systems, XPM sometimes also leads to interchannel crosstalk. There are also techniques that benefit from the fact that XPM allows for interaction between laser beams which is

used, e.g., as quantum nondemolition (QND) measurements.

2.4.5 Stimulated Raman Scattering

Another important nonlinear process that has a strong impact on the ultrashort pulse is SRS. In general, the Raman scattering or the Raman effect describes the light-matter interaction (inelastic scattering), which involves energy exchange and change in the light direction. The Raman effect itself was discovered by a scientist named C. V. Raman in 1928, who got Nobel Prize in Physics for his research on Raman scattering [40]. Later, in the 1960s, the effect has been intensely studied in optical fibers.

The SRS occurs when the intensity of the light in the medium reaches a certain level (threshold). Then, the incident light (pump) induces molecular vibrations. The vibrations modulate the pump beam and generate frequency radiation which is called a *Stokes wave* [15]. It was studied that for high pump intensities, the nonlinear phenomenon of the SRS leads to the situation where the majority of power is transferred to the Stokes wave [41].

In both spontaneous and stimulated Raman effects, inelastic scattering of the pump beam is identified as either lower energy (red-shifted) or higher energy (blue-shifted) radiation. The energy processes that appear in spontaneous Raman scattering, SRS and coherent anti-Stokes Raman scattering (CARS) are compared in Figure 2.11.

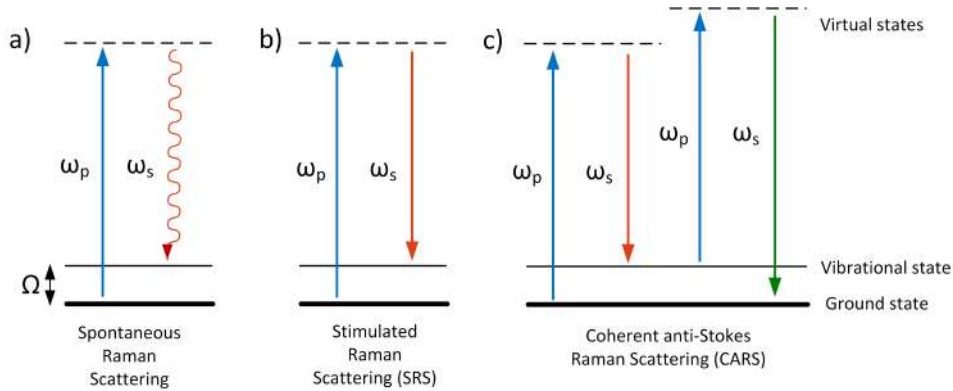


Figure 2.11: Schematic energy diagram for spontaneous Raman scattering (a), stimulated Raman scattering (SRS) (b) and coherent anti-Stokes Raman scattering (CARS) (c).

During spontaneous Raman processes, the pump beam (ω_p) generates the red-shifted radiation (ω_s) (Figure 2.11 a)). In SRS, two incident beams: pump (ω_p) and Stokes (ω_s), are used. When the difference between their frequencies ($\omega_p - \omega_s$) matches the molecular vibration frequency (Ω), the stimulated emission occurs (Figure 2.11 b)). The CARS process (presented in Figure 2.11 c)) is a more complex phenomenon that involves four-wave mixing [42] and is widely used as a biomedical imaging technique for cell and tissue imaging, and in material science [43–45].

The growth of the Stokes radiation wave is described by a formula:

$$\frac{dI_s}{dz} = g_R I_p I_s, \quad (2.67)$$

where I_s corresponds to the Stokes intensity, I_p represents pump intensity, and g_R is a Raman gain coefficient. The Raman gain coefficient, $g_R(\Omega)$, where Ω refers to the frequency difference between the pump and Stokes waves Ω , is the most critical parameter when analyzing the SRS effect. The Raman gain coefficient, which is presented as a function of frequency in Figure 2.12 (a), was measured for fused silica [46]. In general, g_R depends on fiber composition, the type of dopants used in the fiber, and the polarization in the fiber. The Raman response function, which is used in GNLSE, was calculated by Stolen and Gordon [7] and is presented in Figure 2.12 (b). In Figure 2.12 (a) the Raman coefficient is depicted for pumping wavelength $\lambda_p = 1 \mu\text{m}$. For other wavelengths, the Raman gain should be scaled inversely. By looking at Figure 2.12 (a), it can be noticed that the Raman gain can extend over a wide range of frequencies, up to 40 THz, with a peak around the frequency of 13 THz. These characteristics directly result from the amorphous nature of the silica, due to molecular vibrational frequencies overlapping and creating a continuum [47]. Therefore, contrary to many other molecular media where Raman gain appears only for discrete frequencies, in case of silica fibers, the Raman gain covers broad continuous range of frequencies making optical fibers broadband amplifiers.

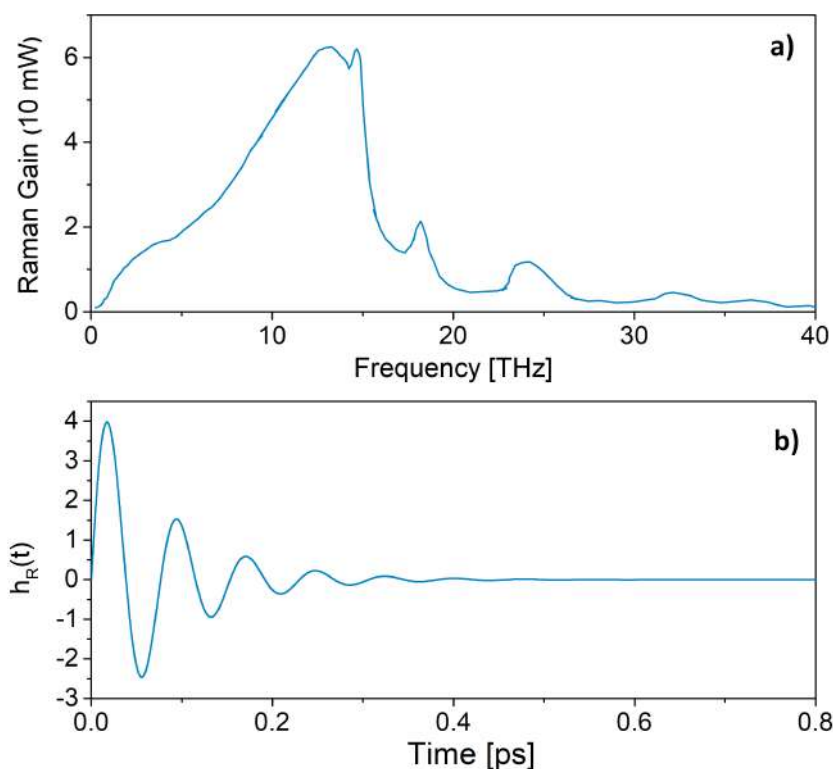


Figure 2.12: Raman gain for fused silica and Raman response function, adapted from [16].

To analyze the SRS effect, let us consider a CW pump that propagates inside an optical fiber. As long as the frequency difference $\Omega = \omega_p - \omega_s$ lies within the Raman-gain spectrum bandwidth, the pump beam will be amplified inside the fiber. The SRS generates photons over the entire bandwidth, therefore, all the frequency components will undergo amplification. However, the frequency component that corresponds to the maximum g_R

would be generated more rapidly. In case of silica fibers, the maximum Raman coefficient corresponds to the frequency difference $\Omega = 13.2$ THz, which means that it would amplify the frequency components which are downshifted by 13.2 THz from the pump frequency. For the $1.55 \mu\text{m}$ pump beam, the corresponding wavelength shift is ≈ 100 nm. The frequency shift is known as the Raman shift.

Soliton Self-Frequency Shift

An interesting consequence of the SRS in optical fibers is intrapulse Raman scattering. Among the higher-order nonlinear phenomena that can affect an ultrashort pulse in an optical fiber, it is by far the most important. It was first observed in 1985 by Dianov et al., who reported Raman pumping of Stokes frequency into a quartz SMF [48]. In 1986 Mitschke and Mollenauer demonstrated a continuous redshift of the centre frequency of a soliton pulse in standard polarization-maintaining (PM) single-mode fiber and named the effect as Soliton Self-Frequency Shift (SSFS) [49]. The phenomenon of SSFS is described as follows. Let us consider a subpicosecond pulse propagating in the optical fiber. In the frequency domain, the pulse possesses a broad spectrum, sufficiently broad to experience Raman gain. The consequence of stimulated Raman scattering is that one part of the spectrum serves as a pump for the other part of the pulse spectrum. Namely, the red portion of the spectrum exhibits gain at the expense of the blue portion of the spectrum. As a result, the pulse shifts towards longer wavelengths. The example of the SSFS effect simulated in a 100 m of PM-SMF is presented in Figure 2.13. In the simulation model, a single-mode fiber was pumped with a femtosecond pumping source at $1.55 \mu\text{m}$ operating wavelength. The duration of the input pulses was 50 fs, and the pulse's peak power was 18 kW. As it is presented in Figure 2.13 (b), when the peak power of the pulse is high enough, the pulse splits from the pump and, as the propagation increases, shifts further to the long-wavelength side. After 100 m of propagation, the pulse (now the optical soliton) reaches $2 \mu\text{m}$ wavelength (Figure 2.13 (a)). It is noticeable that the pulse shape is smooth and the soliton propagates without any disturbances.

Since its discovery, the SSFS effect has been reported in various optical fibers including standard single-mode fibers [50, 51], Thulium- or Holmium-doped gain fibers [52, 53], microstructured air-silica fibers (including Photonic Crystal Fiber (PCF)) [54–59], photonic bandgap fibers [60], and higher-order mode fibers [61, 62]. Due to their outstanding properties (smooth shape, undisturbed propagation at relatively low power levels, tuning possibility), solitons are highly desired in scientific and industrial applications. They can be used as seedings for Tm-doped fiber amplifiers [63] or in a frequency-comb generation [64]. As the soliton shift is a function of wavelength, this effect can be used to reach bandwidths outside the available gain media (such as Ytterbium, Erbium, Thulium and Holmium), e.g. the $1.3 \mu\text{m}$ bandwidth, which is of great interest of optical coherence tomography [65, 66] or $1.7 \mu\text{m}$ bandwidth which can be utilized for biomedical imaging [67–69].

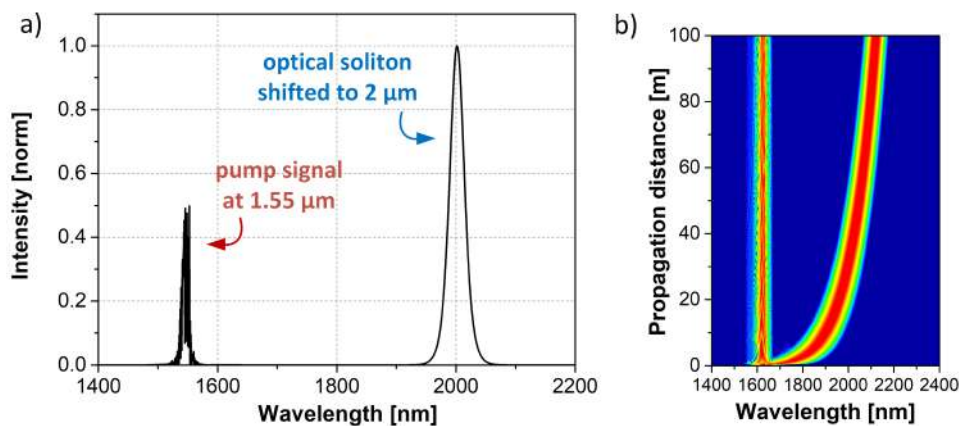


Figure 2.13: Simulated effect of SSFS in PM-SMF: soliton shifted from 1.55 μm to 2 μm (a); propagation of the spectrally shifted soliton in 100 m of PM-SMF. The simulations were performed for the 50 fs duration of the input pulse and the 18 kW of the peak power.

2.4.6 Four-Wave Mixing (FWM)

Four-Wave Mixing is another nonlinear process that arises from third-order optical nonlinearity described by $\chi^{(3)}$ coefficient. In this process, four waves or photons interact together due to material nonlinearity. As a consequence, when a number of frequencies $\omega_1, \dots, \omega_n$ are transmitted simultaneously through a nonlinear medium (such as optical fiber), a refractive index of this material can cause not only a phase shift (as discussed earlier), but it also leads to generating new frequencies such as $2\omega_j - \omega_j$ or $\omega_i + \omega_j - \omega_k$ [20]. Figure 2.14 presents the example of FWM for two incident optical waves generating other two frequencies. For three incident waves, the number of generated new frequencies by FWM is nine. And for a WDM system consisting of ten channels, hundreds of new waves can arise this way. In general, for M possible channels in the WDM system, there exist N possible mixing products, which is given by [70]:

$$N = \frac{1}{2}M^2(M - 1) \quad (2.68)$$

The efficiency of the FWM process depends mainly on phase-matching conditions (the interaction between frequencies depends on their relative phases), but other factors are also important, including: channel spacing, fiber length and chromatic dispersion. The phase matching is satisfied when the spacing between the frequencies involved in the process is very low or for a suitable dispersion profile of the fiber. In fact, the efficiency of the FWM process is much higher in dispersion-shifted fiber when comparing to standard SMF due to the lower values of dispersion for DSF. For a strong phase mismatch, the FWM is effectively suppressed.

The FWM effect is similar to the SRS phenomenon discussed in the previous section due to the fact that both these processes require phase-matching condition. However, in case of SRS, the phase matching is basically automatically fulfilled, whereas for FWM, the phase matching requires specific fiber parameters and a particular choice of input

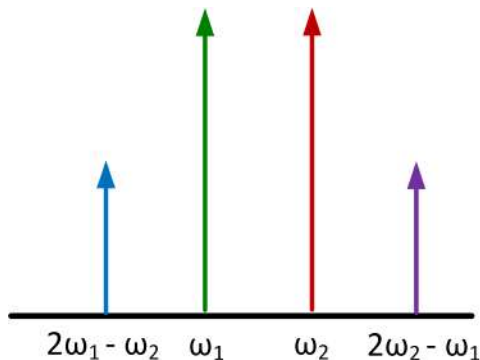


Figure 2.14: Schematic illustration of FWM process for two incident frequencies ω_1 and ω_2 generating other two optical waves: $2\omega_1 - \omega_2$ and $2\omega_2 - \omega_1$.

frequencies for high efficiency of the process.

2.5 Numerical methods for simulating pulse propagation

The GNLS Equation (2.26), which describes, in general, an ultrashort pulse propagation inside an optical fiber, is a nonlinear differential equation that, due to its complexity, cannot be solved with a straightforward analytical method. Therefore a numerical approach is needed. Numerous techniques were introduced for this purpose [71–76]. They usually can be included into one of the two main groups: finite difference and pseudospectral methods. One of the methods that is widely utilized for simulating pulse propagation is called the split-step Fourier method [71, 72]. In this method, Equation (2.26) is written in simplified as:

$$\frac{\partial A}{\partial z} = (\widehat{D} + \widehat{N})A \quad (2.69)$$

where A , as previously, describes the slowly-varying envelope of the pulse, and \widehat{D} and \widehat{N} refer to linear and nonlinear coefficients. The linear operator includes fiber attenuation and dispersion, and the latter governs nonlinear phenomena such as SPM, self-steepening and Raman scattering. Both these individual terms can be expanded as:

$$\widehat{D} = \frac{-i\beta_2}{2} \frac{\partial^2}{\partial T^2} + \frac{\beta_3}{6} \frac{\partial^3}{\partial T^3} - \frac{\alpha}{2}, \quad (2.70)$$

$$\widehat{N} = i\gamma \left(|A|^2 + \frac{i}{\omega} \frac{1}{A} \frac{\partial}{\partial T} (|A|^2 A) - T_R \frac{\partial |A|^2}{\partial T} \right). \quad (2.71)$$

Equation 2.69 divides the linear and nonlinear effects affecting the pulse. This procedure is the approximation used by the split-step Fourier method. In this technique, the length of pulse propagation (fiber length) is split into very short segments in which either dispersion or nonlinearities are considered and, simultaneously, other effects are neglected. The method is graphically demonstrated in Figure 2.15. The pulse propagates from one

segment to another and the FFT algorithm is used to calculate the optical field $A(z,T)$ over a small distance of $h/2$ with dispersion only, then the optical field is multiplied by the nonlinear term (that represents the nonlinear effects over h distance) and finally, the pulse propagates over the remaining distance $h/2$.

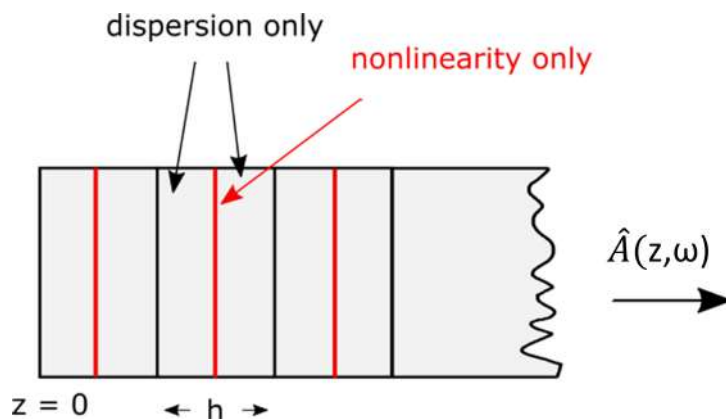


Figure 2.15: Schematic demonstration of the split-step Fourier method.

Although for large numbers of iterations that are necessary for complex systems, the split-step Fourier method becomes time-consuming, it is still often used and is a powerful tool when calculating pulse behavior in optical fibers. It has been widely utilized for investigating the nonlinear phenomena affecting ultrashort pulses in the fibers [23, 77–80], and for such applications, the algorithm can be optimized to perform with fast execution. Recently, AI-based techniques of pulse propagation simulations have been proposed to predict pulse behaviour without the information on the NLS Equation [81]. The split-step Fourier method was used for all simulations that are going to be presented in this dissertation by the Author.

2.6 Microstructured optical fibers (MOF)

2.6.1 Historical perspective and the idea of the MOF

Although silica as a material features a relatively low nonlinear susceptibility, the silica fibers emerged as outstanding nonlinear media because of their small effective area and low losses. However, the efficiency of the nonlinear effects in silica fibers is often limited by the dispersion. A solution to this was demonstrating a new type of fibers: air-silica Microstructured Optical Fiber (MOF), also named as PCF. A MOF is, by definition, any optical fiber in which an air-hole structure is induced in the cladding region and extended in the whole length of the fiber [82–86]. A concept of such fiber was discovered in Bell Labs company not much later than the standard silica optical fiber communication [82]. The development of the MOF technology has been driven by its potential application in optical communication, frequency metrology, fiber-based sensing and optical coherence tomography. The examples of the cladding structure of a MOF include various shapes and sizes, some of them gathered in Figure 2.16. The first realization was demonstrated

by Kaiser et al. in 1974 [82] introducing low-loss fiber entirely from silica. The structure is presented in Figure 2.16 (a). Later, Russel et al. presented a photonic crystal MOF with a structure presented in Figure 2.16 (b). Such a fiber possessed periodic air-holes incorporated in the cladding region. This discovery led to enormous interest in MOF technology and to the development of photonic bandgap MOF (currently known as hollow-core fiber), first demonstrated by Cregan et al. [87]. In these fibers (which structure is presented in Figure 2.16 (c)) light can propagate in an air-core region due to coherent Bragg scattering of the air-holes cladding structure. [86]. A new class of MOF is defined by fibers that incorporate very small core and, due to the proper design of the periodic air-holes in the cladding, are able to provide unique properties of dispersion. An example of such fiber is presented in Fig 2.16 (d).

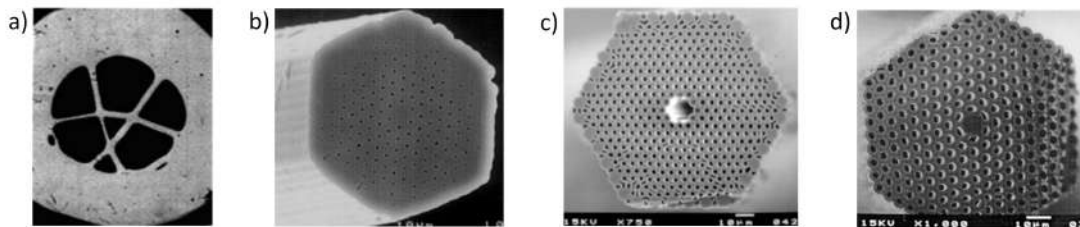


Figure 2.16: Examples of historical MOF structures : (a) first air-silica MOF by Kaiser et al. [82]; (b) photonic crystal MOF demonstrated by Russel et al. [88]; (c) Photonic bandgap MOF by Cregan et al. [87]; (d) dispersion compensating MOF by Ranka et al. [89].

2.6.2 Fiber structure

MOFs are sometimes called *nonlinear fibers* due to their possibility for observing nonlinear effects. However, they differ significantly from commercially available highly nonlinear fibers (HNLF). A comparative illustration of the SMF's, HNLF's and MOF's cross-sections is presented in Figure 2.17. Whereas in conventional fibers (SMF), light is propagated in the core (as a result of total internal reflection) by simply providing a difference in refractive indexes in the core and the cladding, the situation in case of HNLF and MOF is more complex. The HNLFs are designed to possess a high value of the nonlinear coefficient. It can be done by either using a different type of glass (such as chalcogenide glass or modified types of silicate glass, e.g. with germania which increases the nonlinear index), or way more common, to design the fiber for a small value of effective mode area. Here, one way is to provide a design with an index-depressed cladding (fluorine-doped), the other is to provide a depressed *trench* (ring) around the core. In case of air-silica MOF, the cladding region contains a uniform air-hole structure. The removal of the air-hole in the centre of the fiber provides a defect which is considered as a local increase in the refractive index. Therefore light can be guided in this region through the equivalent of the total internal reflection [88].

Although the light guidance mechanism can seem similar to standard fibers, air-silica MOFs contain additional degrees of freedom due to the design possibilities. By modifying

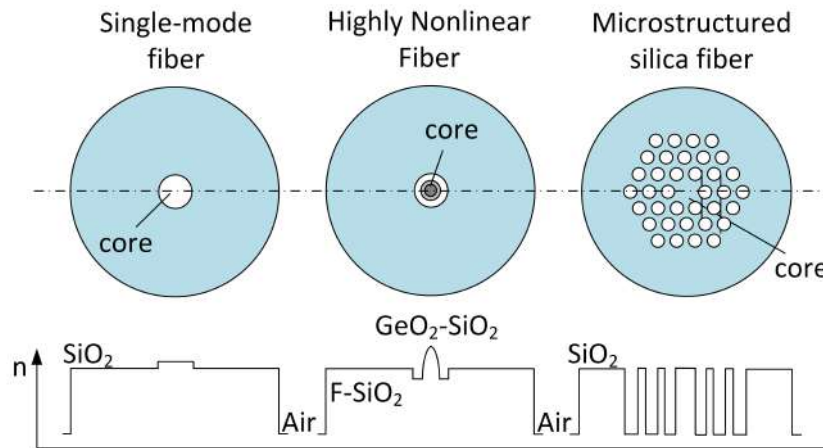


Figure 2.17: The example cross-section of an SMF's (single-mode fiber), HNLF's (highly nonlinear fiber) and MOF's (microstructured optical fiber) structure.

the air-hole structure design, one can affect the parameters of the fiber in a way that is not possible with conventional fibers. In particular, it was reported that a proper design of a MOF can lead to a ZDW shift towards shorter wavelengths than the standard value of $1.3 \mu\text{m}$ for silica fibers [90]. What is more, separately from this research work, it has been proved that the MOF design can enhance the Kerr nonlinearity due to the reduced effective area when compared to standard SMFs [91]. These two discoveries make the MOF technology such an attractive tool for nonlinear optics.

Figure 2.18 presents the schematic representation of an example MOF structure. As it is observed, the fiber consists of a periodic array of air-holes that propagate along the fiber length. The right part of Figure 2.18 shows the detailed view of the cross-section of the same fiber with two important parameters: Λ (pitch) and d , where Λ describes the distance between two neighbouring air-holes and d is the air-hole diameter.

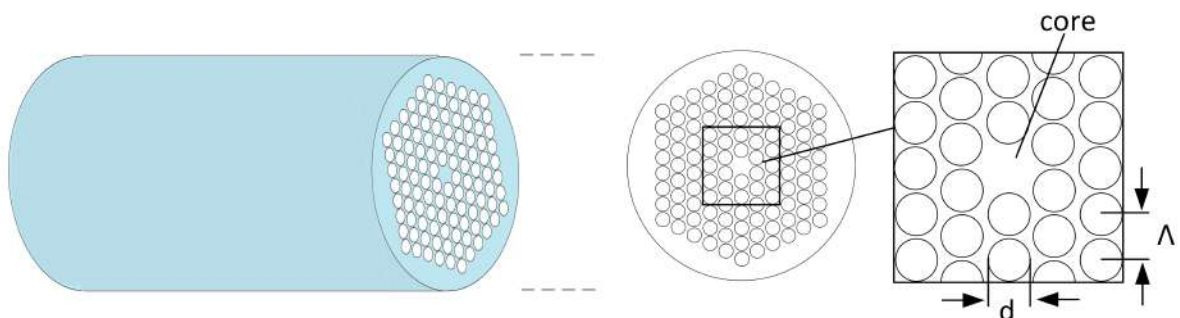


Figure 2.18: The cross-section of a MOF structure.

Air-silica MOFs also benefit from other features, such as: the ability to provide for endlessly single-mode behaviour [88] and the possibility to maintain birefringence [92–94]. These advantages, together with the possibility to modify the dispersion in the fiber and high nonlinearity, made the air-silica microstructured fibers a platform for a variety of applications including studies on new nonlinear effects [95], optical fiber sensing [96, 97],

high-power laser systems [98], and optical telecommunication [99, 100].

2.6.3 SSFS effect in air-silica MOF

One of the nonlinear effects widely studied in air-silica microstructured fibers is SSFS. This effect has already been described in the previous section. When considering simulations of the nonlinear phenomena in the microstructured fiber, in which the effective mode area A_{eff} is much smaller than for the standard fibers, higher-order dispersion needs to be considered. The time window needs to be adjusted for the pulse duration. Let us consider the GNLSE calculations of the SSFS phenomenon in a 1 m of a microstructured silica fiber when pumping the with ultrashort pulses at 1550 nm wavelength. The dispersion profile of the fiber is presented in Figure 2.19. The ZDW of this MOF is ≈ 1240 nm, and the GVD at 1550 nm is -33 ps²/km. The negative sign of the GVD parameter indicates that the dispersion is anomalous for the 1550 nm pumping.

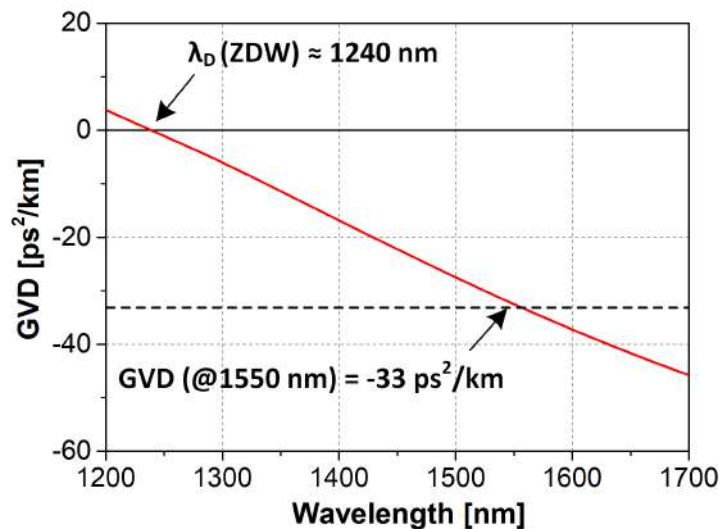


Figure 2.19: Dispersion profile of an SSFS fiber.

The exact values of the fiber dispersion coefficients β up to 7th order are presented in Table 2.1. These coefficients are usually given truncated at β_{10} in the literature [101]. However, since the impact of higher-order betas decreases with the increase of the dispersion order, the Author decided to include only the first seven terms. The fiber's A_{eff} amounts to $10.8 \mu\text{m}^2$ and the nonlinear parameter $\gamma = 9.8 \text{ W}^{-1}\text{km}^{-1}$.

The initial pulse used for launching the fiber possesses a hyperbolic secant field profile that can be described as: $A(0,T) = \sqrt{P_0} \text{sech}(T/T_0)$, where the peak power P_0 is 10 kW and T_0 is 50 fs. The value of T_0 corresponds to the intensity FWHM with a formula: $\Delta\tau = 2 \ln(1 + \sqrt{2})T_0 = 88$ fs [101]. The laser pulse used for the simulation is centred at 1550 nm.

Table 2.1: Taylor series dispersion coefficients.

$\beta_2 = -33.074 \text{ ps}^2/\text{km}$
$\beta_3 = 12.452 \times 10^{-2} \text{ ps}^3/\text{km}$
$\beta_4 = -1.675 \times 10^{-5} \text{ ps}^4/\text{km}$
$\beta_5 = -11.584 \times 10^{-7} \text{ ps}^5/\text{km}$
$\beta_6 = -61.709 \times 10^{-10} \text{ ps}^6/\text{km}$
$\beta_7 = 11.264 \times 10^{-13} \text{ ps}^7/\text{km}$

Figure 2.20 presents the evolution of the pulse spectrum and the pulse temporal shape for different propagation distances in the MOF. The maximum shift reached by the soliton is 2000 nm. Figures (a) and (b) present the optical spectra and temporal pulse shapes for six different distances of propagation. These Figures directly correspond to the spectrograms in Figures 2.20 (c) and (d), which demonstrate the pulse evolution in both wavelength and temporal domains. The spectral evolution shows that in the first 10 cm of the fiber, the pulse spectrum exhibits broadening, followed by spectral separation of two main fields: the pump and the long-wavelength component. Further propagation involves continuous redshift of the optical soliton. Figures 2.20 (b) and (d) indicate that in the temporal domain the pulse is also separated into two distinct peaks. It is observable that the intensity of the spectrally-shifted soliton is at a similar level compared to the 1.55 μm pump, which is a major advantage of this phenomenon and makes it so widely applicable.

It can be easily noticed that, comparing to the results from Section 2.4.5, when the Author discussed simulations for the soliton propagating in the SMF, both values of the peak power and the propagation distance were significantly higher. In fact, the same results were obtained for 100 m of the SMF, where we need only 1 m of the microstructured fiber. It is due to the significantly higher value of the nonlinear coefficient for the MOF.

The corresponding N value for the parameters used in the simulations presented above is 2.7. As discussed in Section 2.4.2, the soliton order depends on the peak power of the pulse launched into the fiber. By increasing the incident power, the soliton order of the propagating pulse also increases. For sufficiently large values of N , the pulse can be perturbed and, as a result, generates numerous sub-pulses of lower amplitude. This process is known as *soliton fission* and is the dominant effect responsible for supercontinuum generation.

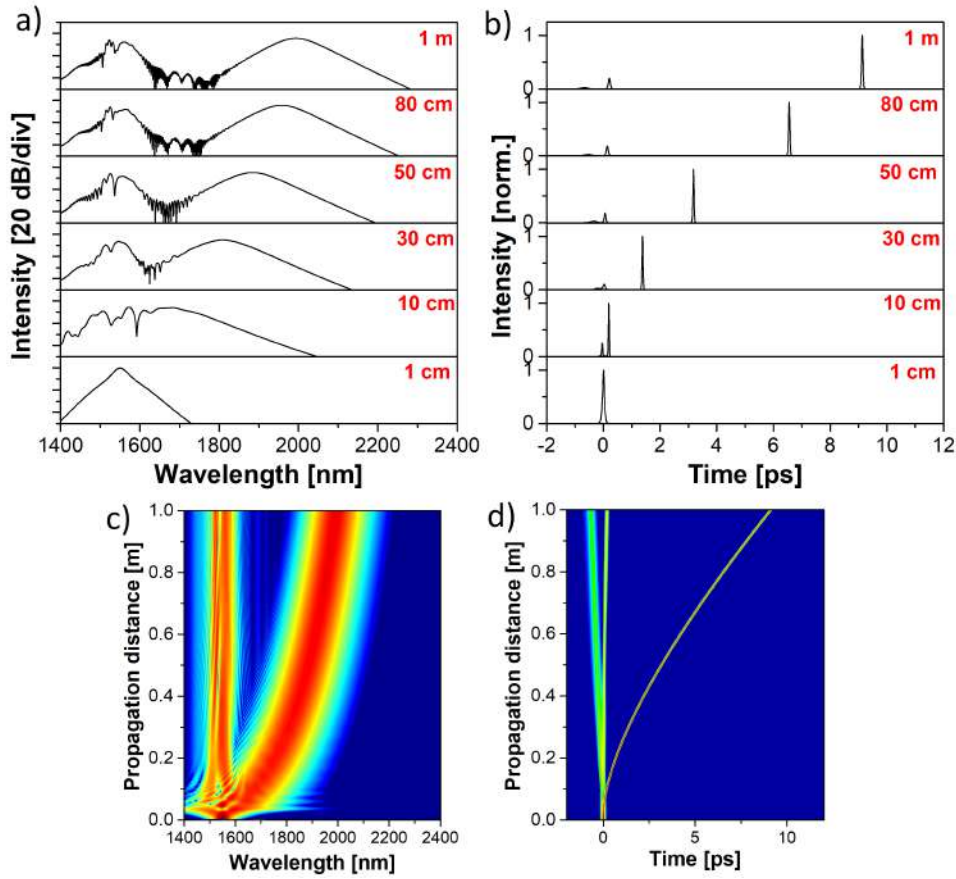


Figure 2.20: Results of the numerical simulations of the SSFS effect in a 1 m of MOF pumped with 50 fs pulse of 10 kW peak power: spectral (a) and temporal (b) evolution of the pulse for selected propagation distances; spectrograms of the spectral (c) and temporal (d) evolutions in the entire propagation distance.

2.6.4 Supercontinuum generation

When ultrashort pulses with sufficiently high power are provided to a highly nonlinear fiber, their spectra can exhibit intense broadening resulting in an output spectrum of bandwidth exceeding 100 THz [16]. The resulting broadened spectra are called *supercontinuum*. The phenomenon of supercontinuum has already been studied in the 1970s [102, 103]. However, the interest in this phenomenon rapidly increased after 2000 when Ranka et al. generated SC in anomalous-dispersion air-silica microstructured fiber [95]. The design possibilities of the MOF technology allowed for the generation of supercontinuum with much broader bandwidths than it was ever possible with bulk media. Nowadays, supercontinuum finds applications in spectroscopy, tunable ultrafast laser sources, pulse compression, optical coherence tomography, and optical frequency metrology. We can distinguish two regimes in which supercontinuum can be generated depending on the sign of dispersion in the fiber. The origins of these two phenomena differ fundamentally.

2.6.5 Supercontinuum in the anomalous dispersion regime

The first results of supercontinuum generated in air-silica microstructured fiber by Ranka et al. were obtained in an anomalous dispersion regime. As it is the same dispersion regime where the solitons are generated, the origins of the SC generation are dominated by the solitons dynamics. In fact, the SC arises as a result of soliton fission. Namely, when initial pulses possess enough power that N is a large value (> 10), their spectra exhibit broadening and the resulting spectrum can extend over an extremely wide range. To better understand these dynamics, let us perform simulations with the use of fiber from the previous example of SSFS in a MOF.

Soliton fission

Figure 2.21 illustrates the spectral and temporal evolution of four pulses of different soliton order: 1.5, 2.7, 6 and 14 in a MOF. The fiber parameters used for this simulation were maintained the same as in the previous Section. 1 m of fiber was pumped with the same 50 fs pumping laser at 1550 nm. It is observed that for $N = 1.5$ (Figure 2.21 (a)), the soliton stretches spectrally but is still attached to the main pump. The pulse also begins to slightly separate temporally. For $N = 2.7$ (Figure 2.21 (b)), the evolution is identical to the example discussed in the previous Section. The pulse is spectrally redshifted with the propagation, it also separates temporally into more distinct peaks. The spectral evolution shows that a small part of the spectrum is blueshifted, generating a so-called *dispersive wave*. Figure 2.21 (c) shows that with further increase of N value ($N = 6$), more sub-pulses appear on both sides of the spectrum. The temporal shape of the pulse consists of several distinct peaks, above which one possesses high intensity and is the only visible one in the linear scale graph depicted on the top in Figure 2.21 (c). In Figure 2.21 (d), for large values of $N = 14$, the pulse spectrum is very broad as it extends beyond 2600 nm. Also, the pulse is not uniform spectrally and it consists of several peaks that correspond to the maxima visible in the spectrogram. The temporal shape of the pulse is broken up into numerous peaks.

Supercontinuum generated in an anomalous dispersion fiber is usually characterized with an unsymmetrical spectrum that contains lots of peaks and modulations. The pulse shape is not maintained as it gets temporally separated into distinct peaks. In this dispersion regime, when $\beta_2 < 0$, two dominant mechanisms are responsible for supercontinuum generation: Raman scattering and higher-order dispersion [101]. These effects cause perturbation of the pulse evolution and lead to pulse breakup due to soliton fission. Actually, it has been reported that, the fact that the broadening mechanism relies on the soliton fission made it sensitive to initial pulse fluctuations and shot noise of the seed source [101, 104, 105], which significantly limits the possibility to use the supercontinuum-based sources for applications that require good stability and noise properties. What is more, the modulation instability, that arise in anomalous dispersion regime, can be responsible for white-noise fluctuations of both the amplitude and phase of the source [101, 105, 106]. To address this issue, numerous studies were devoted to investigate a different regime of generating the supercontinuum, which potentially would feature much better

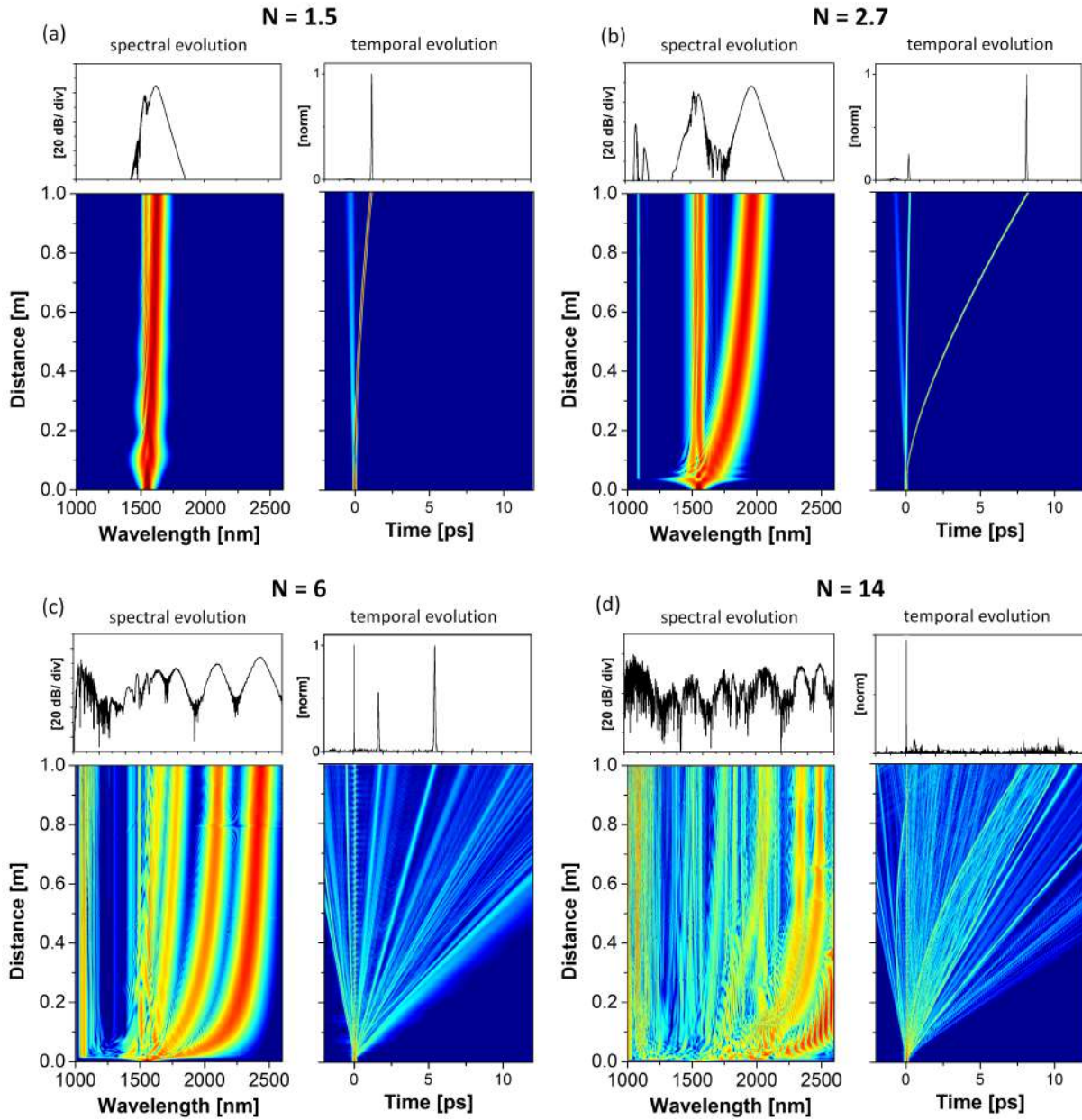


Figure 2.21: Results of the numerical simulations of the supercontinuum in a 1 m of MOF pumped with a 50 fs pulse for four different soliton orders: $N = 1.5$ (a), 2.7 (b), 6 (c), 14 (d): output spectra (top right of each subfigure) and output temporal shape of the pulse (top left), and spectrograms of the spectral (bottom right) and temporal (bottom left) evolutions the pulse propagation inside the MOF.

properties.

The simulations demonstrated in Figure 2.21 show the evolution of the pulse for increasing soliton order, which directly corresponds to the increase of the incident power. To properly analyze the supercontinuum effect itself, it is useful to perform simulations in a shorter segment of the same fiber, where the nonlinear and dispersive effects start to appear. Figure 2.22 presents the simulation results for 15 cm of a MOF pumped with 50 fs laser pulses at 1550 nm wavelength. Figures 2.22 (a) and (b) demonstrate the optical spectra

and temporal pulse shapes for six different propagation distances, respectively. These Figures correspond to the spectrograms presented below: Figures 2.22 (c) and (d) that show the spectral and temporal evolution of the pulse, respectively. It can be noticed that the pulse spectrum broadens rapidly in the first 0.2 cm of the fiber. Within this distance, the broadening is almost symmetrical. Then, other new spectral components appear, mostly on the long-wavelength side of the spectrum. As the propagation distance increases (> 0.5 cm) the spectrum becomes more modulated. When it comes to the temporal pulse evolution, as it has already been mentioned, the pulse shape is not preserved, as it consists of several distinct peaks, above which one is of high intensity.

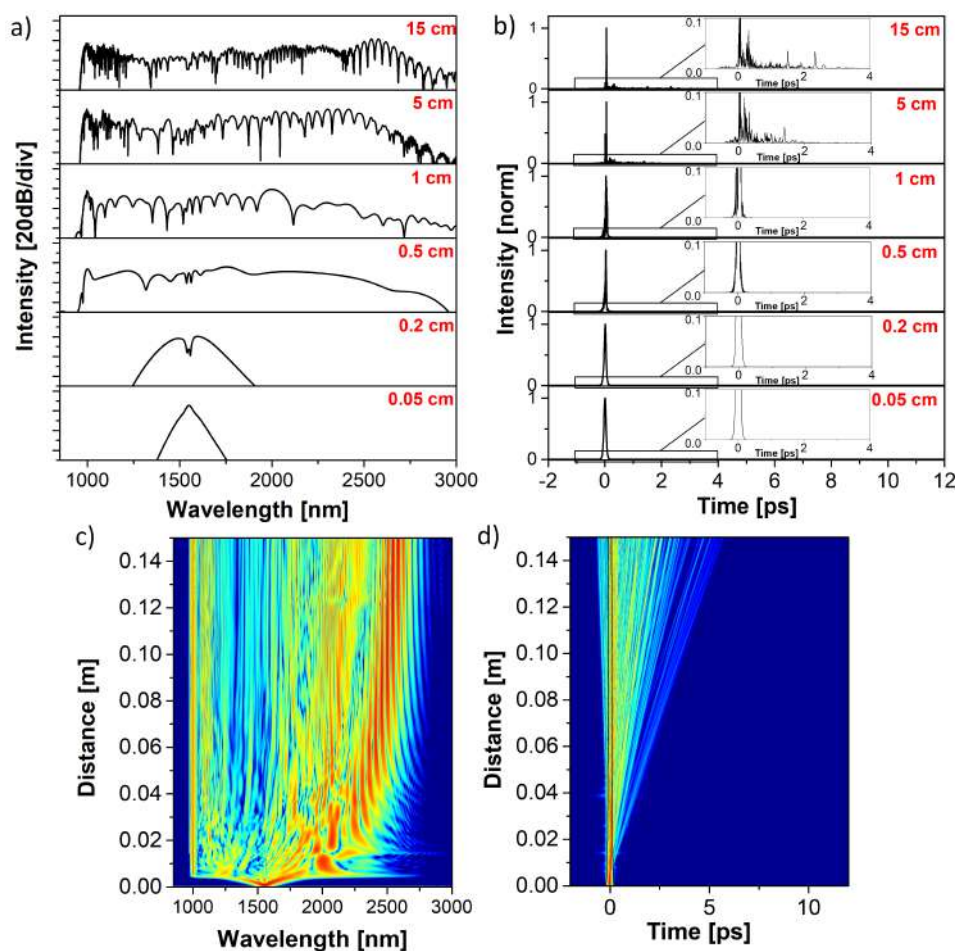


Figure 2.22: Results of the numerical simulations of the supercontinuum in a 0.15 m of MOF pumped with a 50 fs pulse of 260 kW peak power: spectral (a) and temporal (b) evolution of the pulse for selected propagation distances (with zoom to the low intensity peaks); spectrograms of the spectral (c) and temporal (d) evolutions in the entire propagation distance.

2.6.6 All-Normal Dispersion (ANDi) supercontinuum

Recent research works by Heidt et al. [107, 108] have demonstrated that supercontinuum can arise in a normal-dispersion MOF with a suitable design. Such fibers are characterized by low and flat dispersion that is achieved by dispersion-engineered air-hole structure

[109] and are known as all-normal dispersion (ANDi) fibers. ANDi fibers have emerged as potentially low-noise waveguides for supercontinuum generation.

To analyze the supercontinuum phenomenon generated in a fiber with a positive dispersion profile, as previously, one can perform numerical simulations. In this model, a 50 cm-long fiber was pumped with the hyperbolic secant pulses at 1550 nm wavelength, and their FWHM is 50 fs. Figure 2.23 presents the GVD dispersion profile of the fiber. The value of β_2 is 1.28 ps²/km. The fiber possessed no ZDW in the wavelength range of 1200-1700 nm, thus, the dispersion was normal in the entire operating range.

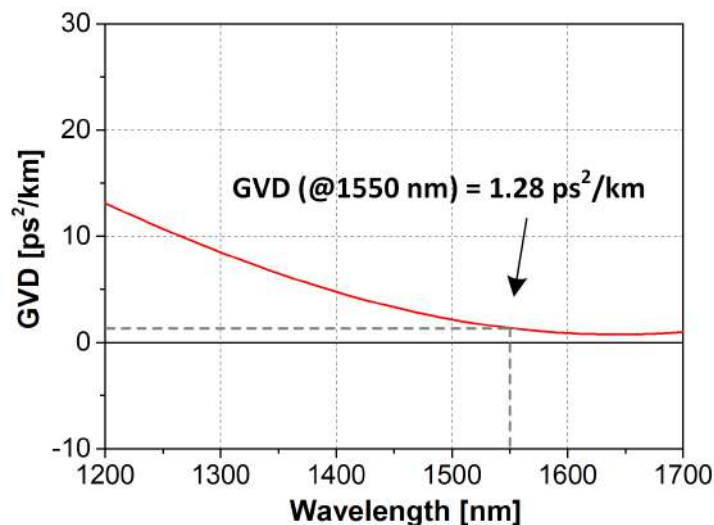


Figure 2.23: Dispersion profile of an SSFS fiber.

Magnitudes of corresponding dispersion coefficients up to the 7th order are demonstrated in Table 2.2. The fiber parameters are: $A_{\text{eff}} = 13.7 \mu\text{m}^2$ and γ amounts to $7.7 \text{ W}^{-1}\text{km}^{-1}$.

Table 2.2: Taylor series dispersion coefficients for normal dispersion fiber.

$\beta_2 = 1.28 \text{ ps}^2/\text{km}$
$\beta_3 = 1.13 \times 10^{-2} \text{ ps}^3/\text{km}$
$\beta_4 = 2.62 \times 10^{-4} \text{ ps}^4/\text{km}$
$\beta_5 = -1.62 \times 10^{-7} \text{ ps}^5/\text{km}$
$\beta_6 = -7.13 \times 10^{-9} \text{ ps}^6/\text{km}$
$\beta_7 = 1.91 \times 10^{-10} \text{ ps}^7/\text{km}$

The spectral and temporal dynamics of the supercontinuum generated in a fiber with a normal dispersion profile are presented in Figure 2.24. Comparing to the anomalous-dispersion fiber case, in this situation, the spectra (depicted in Figure 2.24 a)) are much more flat and smooth. Also, the spectrum is more symmetrical, however, still the majority is in the long-wavelength part. The temporal dynamics are presented in Figure 2.24 b). The pulse's temporal shape gets slightly broadened after 10 cm of the fiber, however, with preserving the uniform profile. It is also a significant difference from the previous example of supercontinuum, when the pulse temporally fell apart into several distinct peaks.

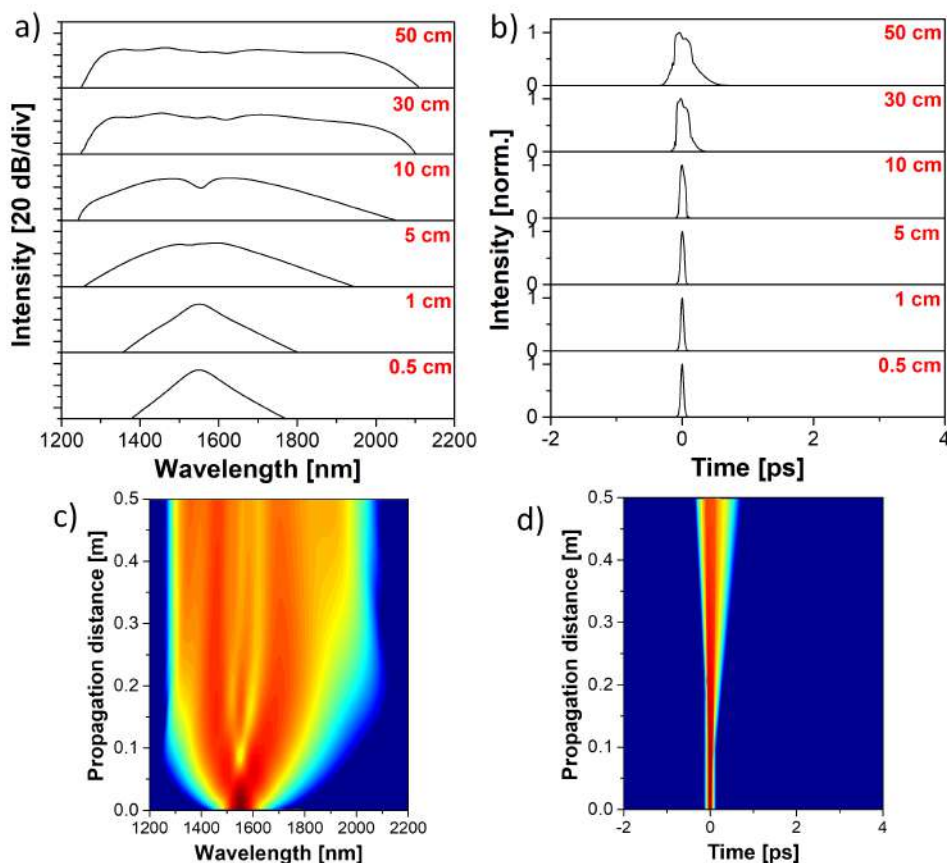


Figure 2.24: Results of the numerical simulations of the supercontinuum effect in a 50 cm of MOF with an anomalous dispersion profile, pumped with 50 fs pulse of 10 kW peak power: spectral (a) and temporal (b) evolution of the pulse for selected propagation distances; spectrograms of the spectral (c) and temporal (d) evolutions in the entire propagation distance.

Supercontinuum in anomalous dispersion fiber vs ANDi fiber

Although both effects discussed earlier have the same definition, they differ significantly in terms of generation mechanism and resulting properties. The broadening mechanism for the supercontinuum formed in an optical fiber with negative dispersion is dominated by the soliton dynamics, in particular a soliton fission which has been described in Section 2.6.4. As a consequence, an ultrabroad supercontinuum features a complex temporal profile, as well as numerous intensity variations with fine-scale structure [110]. Also, it has been reported that the generation of highly coherent supercontinuum is nontrivial when pumping is in an anomalous dispersion regime [111] because of the amplification of noise by modulation instability [112]. These are main factors that made supercontinuum generated in anomalous dispersion regime unsuitable for many applications. Especially the applications implementing supercontinuum spectrum for time-resolved measurements require coherent flat spectrum as well as conservation of a single ultrashort pulse temporal profile. Here, these applications can benefit from the properties offered by ANDi-fibers. It has been proven that spectral broadening generated in normal dispersion fibers can exhibit much better noise properties when compared to the supercontinuum in an anomalous

dispersion regime. Specifically, ANDi-SC often features higher coherence [108, 113], lower amplitude noise level (so-called *relative intensity noise*) [114] and is less likely to produce additional white noise from the Er-doped seed sources. This can be a consequence of different origins for the ANDi-SC generation. In case of ANDi-SC, the processes responsible for the broadening are SPM which is followed by optical-wave breaking (OWB) [107, 115]. As a result, the normal-dispersion spectral broadening is reported to possess a higher threshold (up to 50) for noise-driven decoherence when comparing to the same effect generated in anomalous dispersion fiber [116], also it can minimize the timing jitter between the spectral components [117], and can lead to generating stable and smooth spectra which later can be compressed to obtain high-quality pulses [118, 119].

The previous Sections proved the better performance of ANDi-SC over supercontinuum in anomalous dispersion. However, the question that has been risen, is, whether the SSFS effect, which is also generated in anomalous dispersion regime, is also susceptible to possible excessive noise amplification resulting from the nonlinear processes as in the case of supercontinuum. The Author of this dissertation claims otherwise, and provides the evidence in Chapter 4.

2.7 Pulse characterization methods

In the literature, different techniques are utilized to measure the noise characteristics of the nonlinear phenomena. Nonlinear effects can be investigated in terms of temporal lapping of the consecutive pulses, shot-to-shot stability and amplitude and phase noise relating to the signal itself. Below, some of the methods are being described. The results of the measurements are provided in the next Section.

2.7.1 Dispersive Fourier Transform (DFT)

One of the main challenging problems when it comes to the field of measurements and instrumentation is to measure rapid, short-term phenomena in real-time. Not only in case of the femtosecond laser, but these issues also arise in optical sensing, imaging and spectroscopy. A standard way to perform sensing measurements is to use a spectrometer. However, the scan rate of these instruments is very limited and too long for the span of life of physical processes. Other instruments, such as spectral phase interferometry for direct electric-field reconstruction (SPIDER), do not perform pulse-resolved measurements in real time.

Dispersive Fourier transform (DFT) is a very useful measurement technique that emerged as a way to overcome speed limitations of standard optical instruments and that allows for continuous single-shot measurement [120]. A schematic illustration for the DFT measurement is presented in Figure 2.25. When an input pulse is provided to a dispersive medium, its spectrum is mapped to a temporal shape due to the high GVD of the dispersive medium. The pulse's temporal shape is stretched in time, and therefore it is slow enough for the photodetector. It also enables for measurement of the optical spectrum in the

time domain directly. The analogue-to-digital converter (ADC) that operates in real-time, samples the spectrum by sampling the temporal waveform. This way, the sampling rate is significantly improved when compared to standard spectrometers based on fiber gratings. The DFT technique has found applicability in many areas, including spectroscopy, fast continuous imaging, and to build laser scanners used for optical coherence tomography and high-speed surface vibrometry.

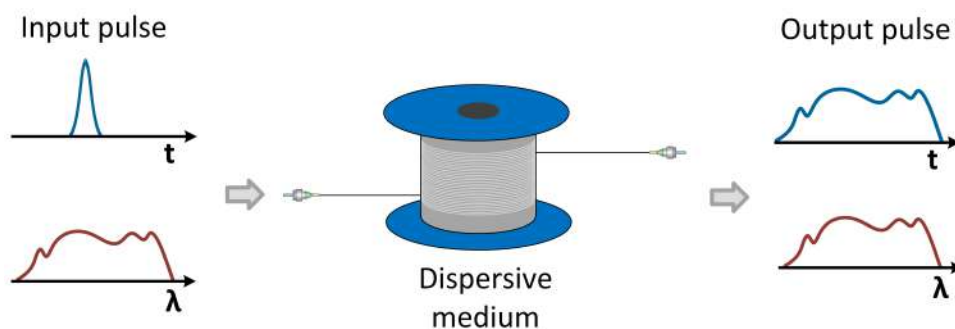


Figure 2.25: The general schematic of the dispersion Fourier transform idea.

In order to measure properties of the pulses generated from the nonlinear fibers with the DFT technique, the train of optical pulses from the nonlinear fiber is provided to a temporally-stretching fiber. The illustration of this method is presented in Figure 2.26. The fiber should possess a large GVD to serve as a dispersive medium. The temporally dispersed pulses are then recorded by the oscilloscope and optical analyzer to verify whether the temporal waveform mimics the spectrum.

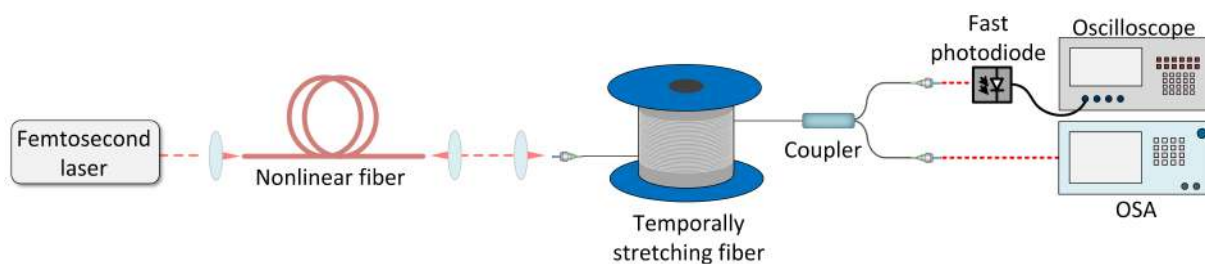


Figure 2.26: The schematic of the dispersion Fourier transform measurement.

The time-wavelength mapping $T(\omega)$ in the far-field approximation is given by [121]:

$$T(\omega) = \sum_{m=1}^{\infty} \frac{\beta_{m+1} \cdot z}{m!} (\omega - \omega_0)^m, \quad (2.72)$$

where β_m corresponds to the m -order dispersion of the stretching fiber and z represents the propagation distance. The data recorded by the oscilloscope is then used in post-processing, that includes the implementation of a computer algorithm in order to obtain intensity correlation maps. Such an intensity correlation measurement is used to determine the energy transfer between different spectral components. This technique has already been used to investigate intensity fluctuations of various nonlinear effects, e.g. soliton collision

[122], or intermodal correlation between the modulation instability sidebands [123]. If we consider time series of intensities $I(\lambda)$ (ensemble) at a wavelength λ in the measured signal from the ensemble, the spectral intensity correlation between two wavelengths λ_1 and λ_2 is given by the formula [124, 125]:

$$\rho(\lambda_1, \lambda_2) = \left| \frac{\langle I(\lambda_1)I(\lambda_2) \rangle \langle I(\lambda_1) \rangle \langle I(\lambda_2) \rangle}{\sqrt{(\langle I^2(\lambda_1) \rangle - \langle I(\lambda_1) \rangle^2)(\langle I^2(\lambda_2) \rangle - \langle I(\lambda_2) \rangle^2)}} \right|, \quad (2.73)$$

where the angle brackets correspond to the average of the ensemble. The correlation value varies over the range $-1 < \rho < 1$ with a colour scale in the graphical illustration corresponding to the degree of correlation. The example of a correlation map from [124] is presented in Figure 2.27. Positive correlation occurs for $\rho > 0$, and is represented by shades of red in the correlation map figure. In this situation, intensities at two wavelengths λ_1 and λ_2 increase or decrease at the same time. The ideal case (when $\rho = 1$) occurs for $\lambda_1 = \lambda_2$. The negative correlation, on the other hand, happens when $\rho < 0$ and is represented by the colour blue in the correlation map illustration. In this scenario, when the intensity at one wavelength, λ_1 increases, the other intensity at λ_2 decreases and vice versa. The correlation maps obtained with the use of experimental data are often displayed together with numerical simulations to identify any unconverted pump radiation.

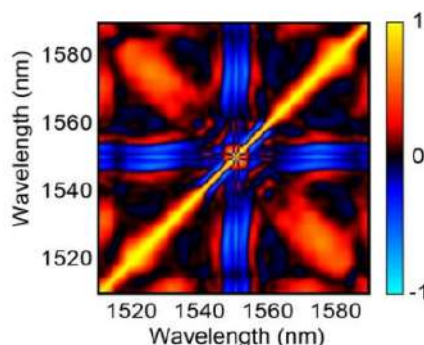


Figure 2.27: Correlation map adapted from [124]. The colour scale presented on the right indicates that positive correlation corresponds to yellow colour, negative refers to blue, and black colour describes a lack of correlation.

The DFT technique is indeed a powerful method to analyze the fluctuations in the pulse spectrum in real-time and with the use of standard laboratory equipment. However, the measurement does not provide the information about the pulse phase. What is more, the spectral resolution of the DFT spectra δ is determined by a few factors, including: oscilloscope bandwidth (B), dispersion of the stretching fiber (D_s), and the stretching distance z as follows: $\delta = (BD_s z)^{-1}$ [126], and therefore it can be limited. Also, the dynamic range is usually smaller than the resolution of the optical spectrum analyzer and, as a consequence, the absolute value of the signal-to-noise ratio is limited. Lastly, the time-wavelength mapping used by the DFT technique provides ambiguity for spectral components near zero-dispersion wavelength [127]. It means that two wavelengths are mapped onto the same delay within the range specified by the ambiguity area.

2.7.2 Pulse-to-pulse coherence

The ability to maintain the coherence by the investigating source, namely to interfere independently, is critical for applications such as frequency metrology, where it is crucial to preserve the phase relation between the optical pulses in the pulse train. Degradation of coherence can lead to amplitude fluctuations and increased timing jitter [128].

The idea of pulse-to-pulse coherence measurement is to split the signal into two branches, among which one possesses a delay, and then measure the interference between two consecutive electric fields. This measurement has already been performed in bulk media (Bellini and Hansch [129]) as well as in an all-fiber setup with a fiber interferometer (Nicholson and Yan [130]). The latter approach can be very useful and has been applied for both soliton and supercontinuum investigations. The schematic illustration of the measurement is demonstrated in Figure 2.28. The effects generated in a nonlinear fiber as a result of pumping by a fs laser source, are provided to an unbalanced Michelson interferometer. The length of one arm is fixed, as the fiber connector is ended with a golden-coated mirror to provide the reflection. The other arm possesses a delay line to provide delay by exactly half of the repetition rate f_{rep} of the pulses train. The second arm is also ended with a mirror placed on a translation stage for the precise length adjustment. The consecutive pulses are then overlapped and the resulting interference pattern can be recorded by the Optical Spectrum Analyzer (OSA) on the output arm of the interferometer.

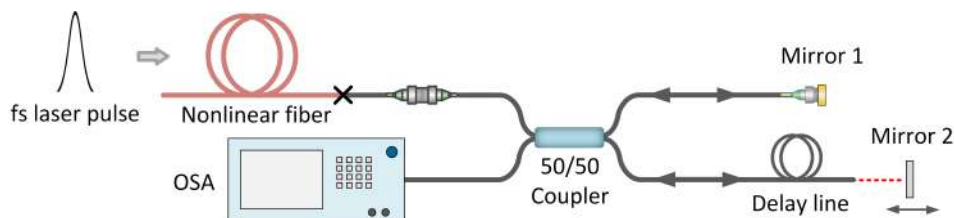


Figure 2.28: Coherence measurement setup.

To numerically estimate the coherence degree of two independent electric fields we can implement the fringe visibility function V that is expressed as:

$$V(\lambda) = \frac{I_{\max}(\lambda) - I_{\min}(\lambda)}{I_{\max}(\lambda) + I_{\min}(\lambda)}, \quad (2.74)$$

where I_{\max} and I_{\min} correspond to maximum and minimum intensities of the signal measured by the detector. The examples of possible results of coherence measurement for different scenarios are given in Figure 2.29. For the ideal case, the parameter $V = 1$, it means that the signal is fully coherent and the output signal resembles Figure 2.29 (a). Usually, there is at least slight coherence degradation and $V < 1$, then the pulse is partially coherent (Figure 2.29 (b)). No coherence occurs for $V = 0$ (Figure 2.29 (c)).

The method has already been used for the coherence measurement of oscillators [131], optical solitons [64], and supercontinuum [132].

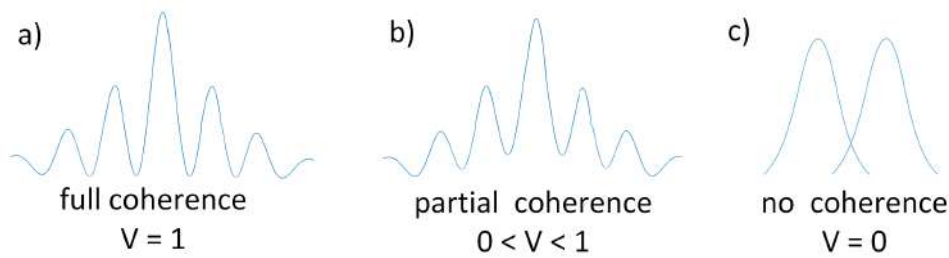


Figure 2.29: Examples of coherence measurement results: full coherence occurs for $V = 1$ (a), for $0 < V < 1$ the pulse is partially coherent (b), and for $V = 0$ there is a lack of coherence (c).

2.7.3 Frequency Resolved Optical Gating (FROG) measurements

A FROG is a measurement technique used for determining a complete characterization of a pulse [133, 134], including its optical spectrum, pulse temporal shape, temporal phase and spectral phase. A reference pulse is not required in this technique, as the measurement involves the interaction of the pulse and the relative delay of a replica of the pulse. A nonlinear medium is utilized here to produce the signal when both pulses are matched temporally (so-called *optical gating*).

A general setup of the FROG technique is presented in Figure 2.30. Input pulses are split by the beam splitter into two separate beams that meet at the nonlinear medium (e.g. nonlinear crystal). The setup resembles the autocorrelator but here the spectrometer is used instead of a photodetector. In both these techniques a nonlinear effect is used to generate the signal. The autocorrelator measures the intensity of the pulse field and assumes the pulse shape, thus does not provide the information about the pulse phase. On

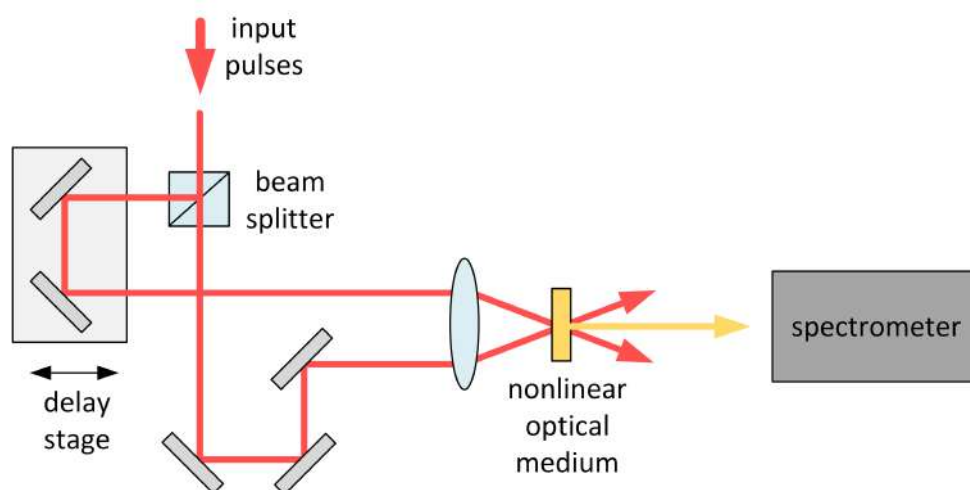


Figure 2.30: The schematic of the FROG measurement.

the other hand, the FROG extends the idea significantly, since it performs the analysis of the pulse spectrum at each delay, creating, as a result, a spectrogram of the pulse which is the pulse intensity as a function of the frequency and time delay, displayed with

a colour scale. Then, an iterative algorithm is used to reconstruct the pulse shape from the spectrogram (the FROG trace).

FROG became a standard technique for pulse measurements as it provides detailed information on pulse spectral and temporal characteristics. It can be used to measure pulses of a duration from nanoseconds to femtoseconds and is suitable for both simple pulse measurements as well as quite complex pulses.

2.7.4 Relative Intensity Noise (RIN)

Other noise that arises within the nonlinear phenomena, and can limit the measurement precision in potential applications, originates from power fluctuations of a laser source. White noise, which is generated through spontaneous emission in the mode-locking process, can be amplified and transferred to the next stages of the laser system. A common way to describe the instability of a laser source is to specify its *relative intensity noise* (RIN) [135, 136]. The value of optical power of the laser P can be expressed as a sum of average power P_{avg} and fluctuating quantity $\Delta P(t)$:

$$P(t) = P_{avg} + \Delta P(t). \quad (2.75)$$

In general, RIN is defined as a ratio of the mean square power noise and the average power of the laser [137]:

$$\text{RIN} = \frac{\langle \Delta P(t)^2 \rangle}{P_{avg}^2}. \quad (2.76)$$

Thus, the relative intensity noise is a measure used to describe fluctuations in an average power of a recorded signal (e.g. optical pulse train) over a given measurement time span, and it represents the stability of the signal's average power. The optical power of the laser signal is first identified with a fast photodetector, therefore, the fluctuations of the optical power are transformed to the electrical power, and the electrical power fluctuations are measured by the oscilloscope or an electrical spectrum analyzer. The electrical power $P_E(t)$ is proportional to the power intensity, which is determined as the squared optical power:

$$I = P(t)^2 \propto P_E(t). \quad (2.77)$$

Therefore RIN parameter can now be expressed through corresponding electrical measures:

$$\text{RIN} = \frac{\Delta P_E(t)}{P_{Eavg}}. \quad (2.78)$$

The noise power from Eq. 2.76 can also be represented in the Fourier frequency domain by a power spectral density (PSD) :

$$S_{\text{RIN}}(f) = \int_{-\infty}^{+\infty} \frac{\langle \Delta P(t) \Delta P(t + \tau) \rangle}{P_{avg}^2} e^{-j2\pi f \tau} d\tau \quad (2.79)$$

$$= \lim_{T \rightarrow \infty} \frac{1}{T} \left\langle \left| \int_{-T/2}^{+T/2} \frac{\Delta P(t)}{P_{\text{avg}}} e^{-j2\pi ft} dt \right|^2 \right\rangle, \quad (2.80)$$

where the first relation (Eg. 2.79) comes from a Wiener-Khinchin theorem which says that the PSD refers to a Fourier transform of the autocorrelation function when the process is random and wide-sense stationary (it means that its mean function and the correlation function do not vary by shifts in time) [138]. The second equation (Eq. 2.80) is a result of the Parseval theorem, and indicates that the PSD can be obtained by taking the average of the power of Fourier-transformed fluctuations measured in the time domain.

By calculating the integration of the RIN PSD, one can obtain a root mean square value of RIN from Eq. 2.76, which is known as integrated RIN and expressed in %. The integrated RIN is then calculated as:

$$\text{RIN} = \int_{1/T}^{f_{\text{rep}}/2} S_{\text{RIN}}(f) df. \quad (2.81)$$

where $f_{\text{rep}}/2$ refers to the Nyquist frequency of the signal (the pulse train). In practice, the RIN PSD at higher Fourier frequencies is much lower, therefore, most of the studies report the measured RIN PSD and integrated RIN up to ~ 100 kHz or to ~ 20 MHz ranges. The conceptual illustration of the RIN definition in the time and frequency domain is presented in Figure 2.31.

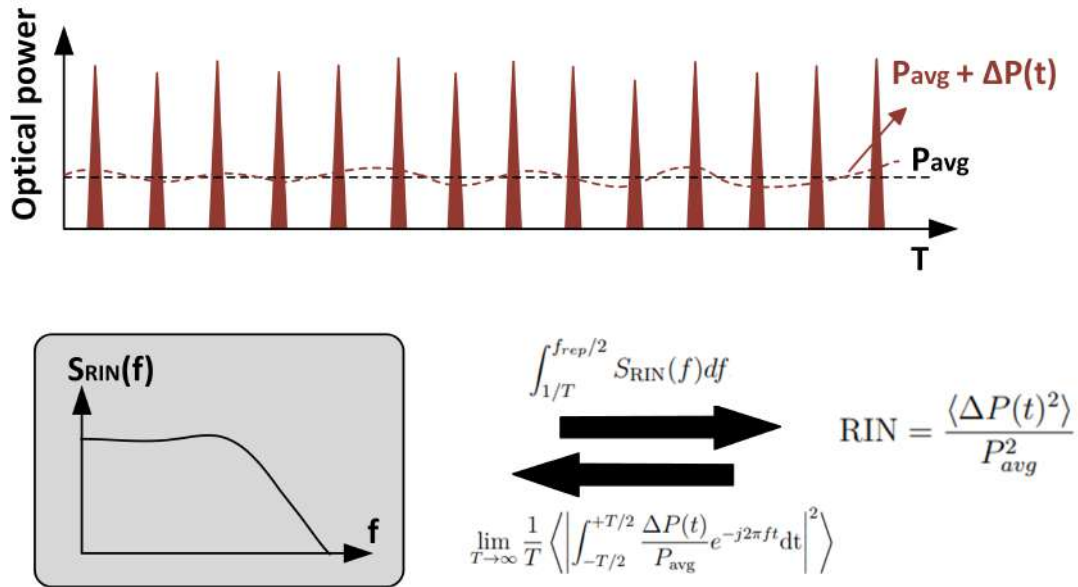


Figure 2.31: Relative intensity noise of a mode-locked laser output.

The units of the RIN are Hz^{-1} but it is usually expressed as 10 times the logarithm (to the base of 10) of the measured quantity, and the units are dBc/Hz. An example of a schematic of the RIN measurement is demonstrated in Figure 2.32. The laser signal is first attenuated by the neutral density (ND) filter to avoid detector saturation and ensure the linear response of the detector. The optical signal is then detected by the fast photodiode, and goes through a low-pass filter (LPF). The output laser signal needs to be spectrally

filtered to isolate particular spectral components, therefore, either a photodetector followed by the LPF or a low-bandwidth photodetector is required. Eventually, the electrical signal is recorded by the oscilloscope including both DC and AC components. The DC level of the signal is necessary for normalization purposes, and the AC component is recorded and used in post-processing. The computer analysis includes averaging, window sampling, FFT calculation, normalization and lastly, calculating the integration over the required frequency interval.

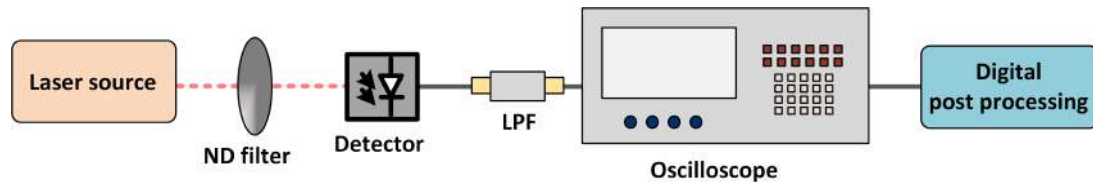


Figure 2.32: The schematic of the RIN measurement. ND: neutral density; LPF: low-pass filter.

In general, the intensity noise in femtosecond lasers is a result of quantum sources (including ASE noise and fluctuation in vacuum noise) as well as the contribution of external technical noise (such as pump drivers, power supply connected to the pump driver, and the intensity noise of the pump laser itself). RIN measurements have recently become quite popular as they emerged as a suitable method to directly compare different laser systems. Especially the integrated RIN is treated as a comparative measure as it allows to quantitatively describe different laser setups. However, it is worth noting that RIN measured over different frequency ranges can result in values that are unlike, therefore, it is crucial to provide the integration range together with the result of RIN in %. As the technique is quite universal, it has been implemented to analyze the contribution of the noise by the nonlinear effects, including both SSFS and supercontinuum.

Chapter 3

Dual-wavelength pumped highly birefringent microstructured silica fiber

3.1 Introduction

The discovery of the SSFS effect opened a new platform for a variety of applications, such as mid-infrared optical frequency comb generation [139], three-photon microscopy for deep tissue imaging [67], or seed sources for fiber amplifiers [58]. The SSFS phenomenon enables continuous broad wavelength tuning of ultrashort laser pulses with an efficiency up to 97% [140]. Spectral conversion can be successfully implemented in standard single-mode silica fibers, however, with nonlinear coefficient and dispersion properties limited to certain levels. The first pumping of the Stokes frequency by the input source in a single-mode quartz fiber was reported in 1985 by Dianov et al. [48]. The SSFS was first officially discovered one year later, in a PM SMF [49] where Mitschke and Mollenauer observed a 75 nm shift from 1.5 μm pumping. Later, Beaud et al. demonstrated a soliton shift from 1.36 to 1.54 μm [50], and Nishizawa presented soliton generation up to 2.03 μm from 1.5 μm pumping [51]. Since the dispersion of the silica fiber is anomalous and has a ZDW $\approx 1.3 \mu\text{m}$, the soliton propagation in the SMF is narrowed to the region of $\lambda > 1.3 \mu\text{m}$. Compared to the standard silica fiber, a MOF possesses design flexibility which allows for improving the tuning range of the ultrashort pulses with maintaining the high birefringence. Air-silica microstructured fibers have proved to be a great medium for the generation and observation of the spectral conversion of optical solitons. The structure of a MOF, however, can be designed so that the zero-dispersion wavelength (ZDW) is shifted to shorter wavelengths, allowing the use of Yb-doped lasers for soliton generation. In [54], Washburn et al. demonstrated the SSFS effect in a MOF with wavelength tunability of 0.85-1.05 μm . In [55], Cormack et al. achieved SSFS up to 1.26 μm from 0.8 μm pumping. Other studies reported achieving the spectral tuning of the optical solitons in a MOF within a wavelength range between 0.6 μm and 1.7 μm [56, 57, 141–144], however, still with the use a microstructured fiber optimized for only one pumping source.

In this chapter, an analysis of the SSFS effect in a microstructured silica fiber which can be pumped by two different wavelengths is going to be presented. A full characterization of the fiber is provided, including fiber dispersion profile and details of the structure design. The numerical simulations are presented together with the experimental results obtained for two pumping schemes. Eventually, the analysis including a degree of coherence and polarization extinction ratio (PER) for the fabricated fiber is performed. The research has been conducted in cooperation with the Faculty of Fundamental Problems of Technology from our University, the Laboratory of Optical Fiber Technology in Lublin and the Department of Physics from Umeå University in Sweden. To our knowledge, there was no example in the literature of using any kind of fiber which would be suitable for two pumping wavelengths simultaneously. The results of this work were published in [59]. We believe that such microstructured silica fiber would become a versatile tool for numerous MIR systems.

3.2 Microstructured silica fiber

3.2.1 The aim of the study

A motivation for this research has been to propose a microstructured silica fiber that would be suitable for two very common pumping wavelengths: $1\ \mu\text{m}$ and $1.5\ \mu\text{m}$. By properly selecting the fiber parameters one is able to shift the ZDW to the shorter wavelengths, enabling pumping with desired sources. These parameters are: a lattice pitch (Λ), which corresponds to the distance between two neighbouring air holes, and air filling factor $ff = d/\Lambda$, where d describes the air hole diameter in the cladding. The MOF with an optimal fiber design would then be drawn in the Laboratory of Optical Fiber Technology in Lublin and investigated in experiment with the use of femtosecond lasers. Since most of the examples in the literature concentrate on scaling up the powers, shortening the output pulse duration, and extending the covering bandwidth, the other issues concerning coherence degree or polarization are often neglected. However, to ensure the demonstrated setup would be suitable for real-life applications, it is often crucial to possess a high degree of coherence and high-quality linear polarization. Our goal was to verify these properties.

3.2.2 Description of the fiber structure

The microstructured fiber has been designed and modelled by the Optics and Photonics Group in the Faculty of Fundamental Problems at the WRUST. The final parameters of the designed MOF structure are as follows:

- the pitch distance $\Lambda = 2.7\ \mu\text{m}$
- the diameter of the small holes $d_s = 1.44\ \mu\text{m}$ ($ff_s = 0.53$)
- the bigger holes' diameter $d = 2.2\ \mu\text{m}$ ($ff = 0.81$)

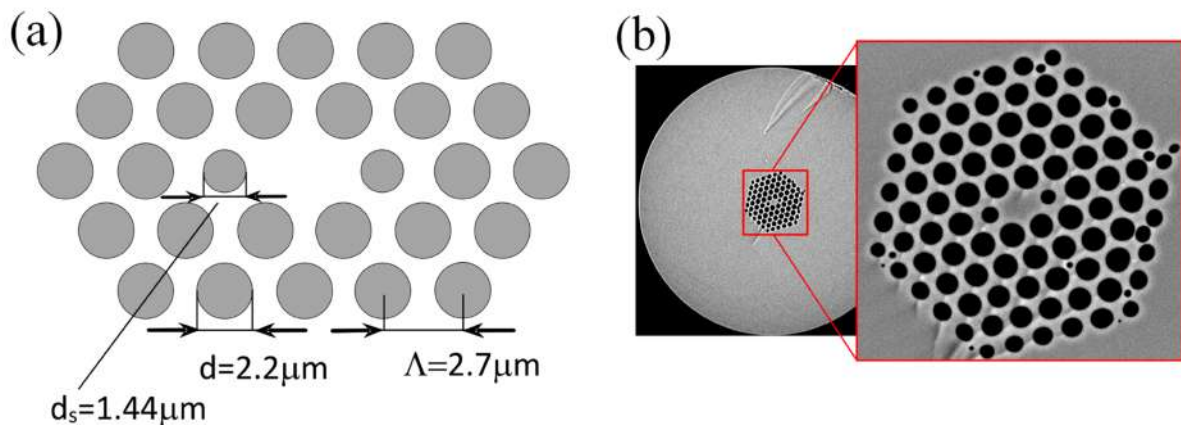


Figure 3.1: (a) Design parameters of the MOF structure: lattice pitch (Λ), d – diameter of cladding holes, d_s – diameter of small holes adjacent symmetrically to the core; (b) Scanning electron microscope image of the fiber cross-section.

The transmission loss spectrum of the MOF is presented in Figure 3.2. In the considered range ($1.2 - 2.0 \mu\text{m}$) the transmission is maintained below 0.1 dB/m with the exception of the wavelengths covering the OH absorption bands.

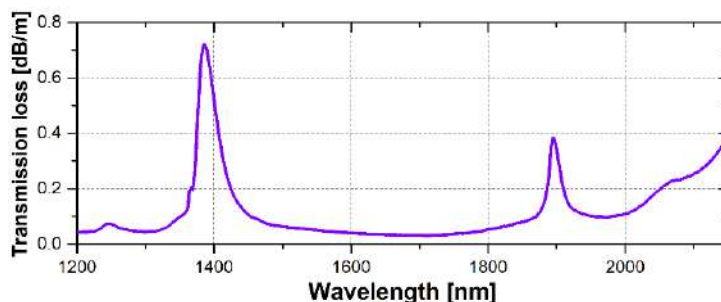


Figure 3.2: Transmission loss spectrum of the fabricated MOF.

The spectral dependence of chromatic dispersion for both polarization modes in the $0.85 - 2 \mu\text{m}$ spectral range is illustrated in Figure 3.3. Here, the measured and calculated spectral dependence of dispersion is depicted for two polarization modes: LP_{01}^X , LP_{01}^Y . The ZDW amounts to 932 nm and 945 nm for the modes LP_{01}^X , LP_{01}^Y , respectively. Two arrows in Figure 3.3 indicate the pump wavelengths: $1.04 \mu\text{m}$ and $1.56 \mu\text{m}$.

3.3 Experimental results of the SSFS generation in the MOF

The experimental setup is presented in Figure 3.4. Two different types of pumping sources have been used for this experiment. One of them was a commercial Ytterbium-doped fiber laser (YDFL) system (Orange-HP, Menlo Systems) that emitted 60 fs pulses centred at $1.04 \mu\text{m}$ with 125 MHz repetition rate. The other one was an in-house built Erbium-doped fiber laser (EDFL) delivering 25 fs pulses at $1.55 \mu\text{m}$ with 45 MHz repetition

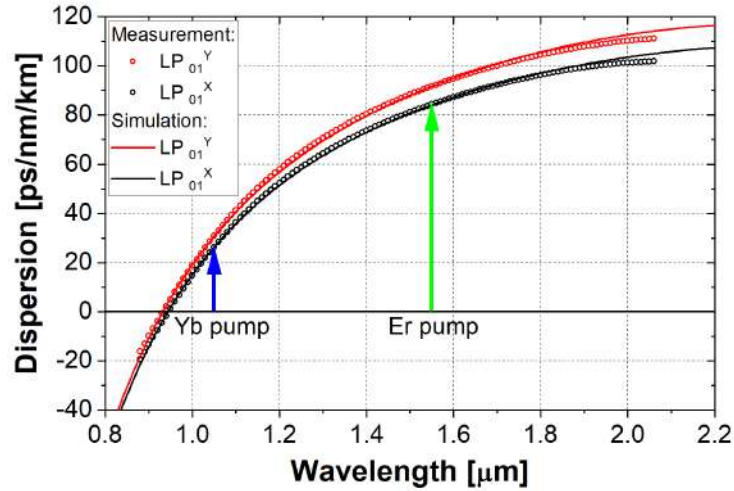


Figure 3.3: Measured (dots) and calculated (solid line) dispersion profiles of the fabricated MOF for two orthogonal polarization modes. The arrows indicate the pumping wavelengths.

rate (explained in details [145]). The laser beam was coupled to the SSFS fiber via an aspheric lens (AL) with a focal length of 3.1 mm. The half-wave plate (HWP) together with the polarizing beam-splitter (PBS), served as an attenuator of the input power. The other HWP was used to adjust the proper input polarization to the nonlinear fiber. The second aspheric lens was used to collimate the output laser beam from the fiber and the bandpass filter (F) was utilized to cut the residual pump out which allowed for measurement of the power stored in the solitons. The laser beam from the fiber output was then provided to the optical spectrum analyzer (OSA) for the measurements.

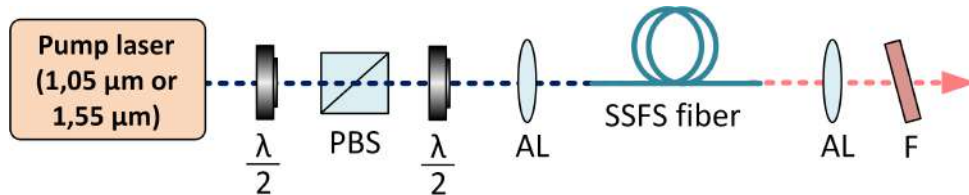


Figure 3.4: Experimental setup for SSFS generation; $\frac{1}{\lambda}$: half-wave plate, PBS: polarizing beam-splitter, AL: aspheric lens, F: bandpass filter.

The experimental spectra generated in the 1.5 m long fiber pumped with 1.04 μm and 1.55 μm are presented in Figure 3.5. All the spectra were recorded with the polarization aligned to the slow axis of the fiber. The spectra in Figure 3.5 (a) were registered with the use of a home-built Fourier spectrometer, whereas the spectra in Figure 3.5 (b) were recorded with the use of OSA (Yokogawa AQ6375). The spectral tuning of the solitons was obtained by simply changing the laser power coupled to the fiber, stated as P_{in} in Figure 3.5. For the 1.04 μm pumping the input power was changed from 100 to 275 mW, and the achieved spectral range of the shifted solitons was 1.42–1.67 μm . In case of 1.55 μm pumping, the input power varied between 58 to 107 mW, and the soliton shift covered the wavelength range of 1.70–1.95 μm .

The experimental results of the generated solitons presented in Figure 3.5 were plotted together with the simulated solitons' spectra. The numerical model was based on the General Nonlinear Schrödinger Equation solver [146]. The solver was adjusted to include the Raman response function [46], the dispersion of the effective mode area [147], and wavelength-dependent attenuation [148]. It has also been verified that the scalar approach is actually comparable to the vector approach with the Raman response function [149].

The simulations were performed for both pumping sources: YDFL and EDFL, over a propagation distance of 1.5 m. The power levels which were considered in the simulation model are described as P_{exp}^{sol} and presented in Figure 3.5. They were corrected with respect to the coupling efficiency calculated from the experiment: 47% for the YDFL pumping and 50% for the EDFA pumping. The initial pulse of the pumping laser was combined of three hyperbolic sech pulses to imitate the experimental pulse autocorrelation as described in [46].

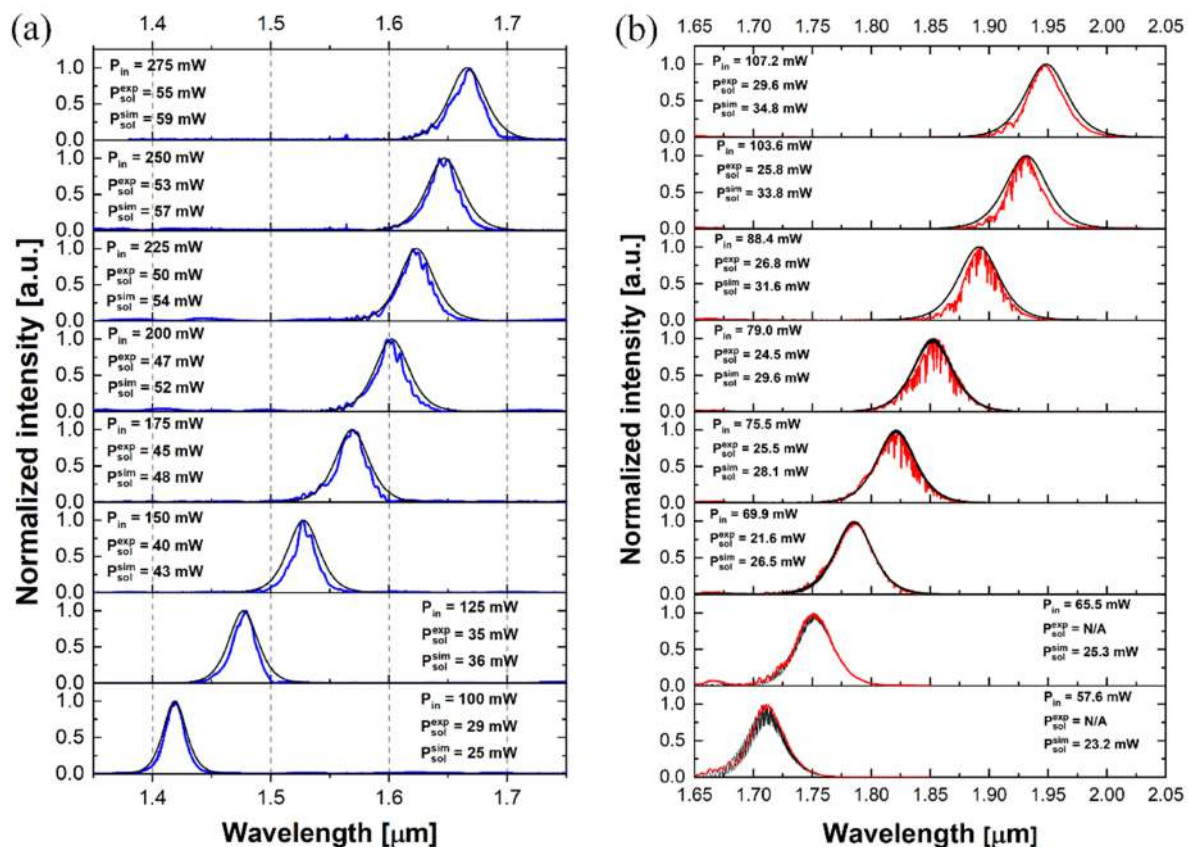


Figure 3.5: Experimental (coloured lines) and numerical (black lines) optical spectra of SSFS generation for the 1.5 m long SSFS fiber for YDFL (a) and EDFL (b) pumping.

Figure 3.6 gathers the magnitudes of power levels stored in the solitons, the conversion efficiency and the central wavelengths of the solitons as a function of pumping power for both YDFL (a) and EDFL (b) laser sources. The average optical powers stored in the tunable solitons were measured with a power meter with a thermal sensor and the use of a long-pass filter with 1.35 μm cut-off wavelength (Thorlabs FELH1350). In case of YDFL, the measured power was between 29 mW (for the shortest-wavelength soliton) and 55 mW (for the longest-wavelength soliton). The achieved power levels stored in the solitons correspond to the power conversion efficiency in the range of 20-28%. For the 1.55 μm pumping, the average optical power stored in the solitons was measured with the same thermal power meter and a filter with the transmission band of 1750-2250 nm (Thorlabs FB2000-500). The average power stored in the solitons was in the range of 21.6 mW (for the soliton centred at 1786 nm) and 29.6 mW (for the soliton at 1948 nm). The power conversion efficiency for these solitons was in the level of 27-33%.

It has to be pointed out that the conversion efficiency measurements were performed with respect to the laser powers in front of the fiber end. Therefore, the efficiency values also included coupling efficiency to the fiber, which was in the range of 47-58%. These results are similar to the outcomes from the literature: 22% in [150], 10% in [58], 35% in [151, 152].

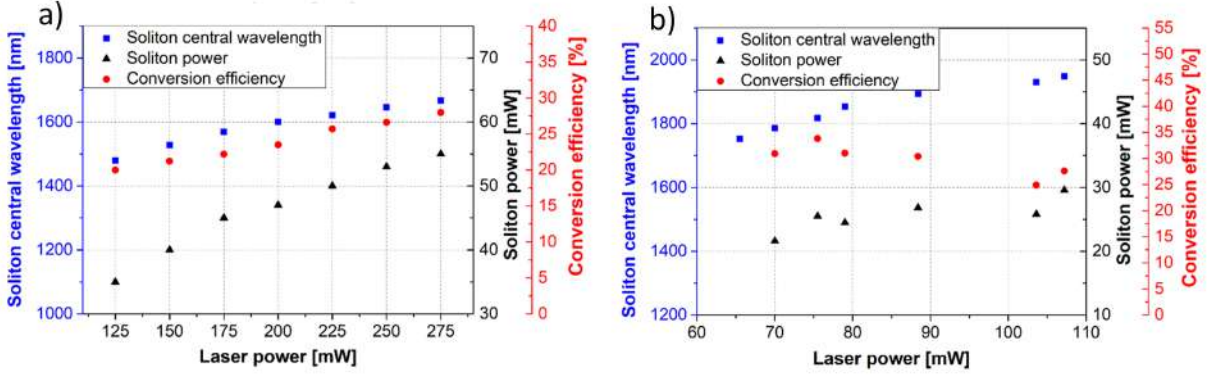


Figure 3.6: Soliton central wavelength (blue squares), power stored in the soliton (black triangles), and conversion efficiency (red dots) as a function of the power of the laser for YDFA (a) and EDFA (b) pumping.

3.3.1 Coherence measurements

Coherence measurements for the fabricated MOF have been performed in a manner that has already been described in Chapter 2. Therefore, for this purpose a home-built fiber interferometer was used based on the Michelson scheme. Figure 3.7 presents the results of the coherence measurement for both, $1.04 \mu\text{m}$ (a) and $1.55 \mu\text{m}$ (b) pumping. For the YDFL pumping, the $V(\lambda)$ is at the level of $0.7 - 0.9$ for the solitons between 1.4 to $1.7 \mu\text{m}$ wavelength, whereas for EDFA pumping the coherence degree reaches up to even 0.9 . The results confirm the high coherence of the shifted solitons for both pumping sources. In Figure 3.7 (b), one can notice a slight degradation in the range of $1.77 - 1.87 \mu\text{m}$ wavelength. However, the origins are not fully understood and it requires further research on the subject.

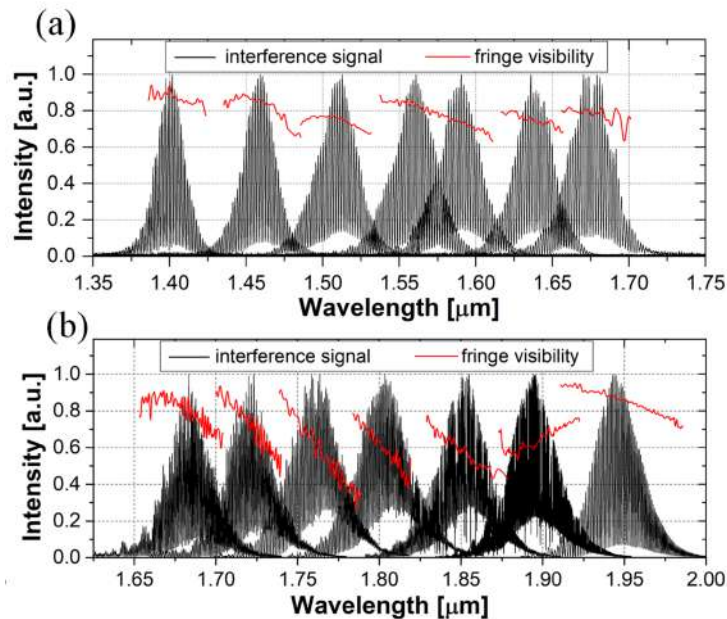


Figure 3.7: The results of coherence measurements for solitons generated in a MOF in case of YDFA (a) and EDFA (b) pumping.

3.3.2 SSFS for different MOF segments

The maximum possible soliton shift was also verified for different lengths of the MOF fiber. Five different segments of the fiber: 150, 180, 210, 230 and 275 cm were pumped with the EDFA laser in order to verify the maximum spectral soliton shift for maximum pumping power (107.2 mW) of the laser. The results are plotted in Figure 3.8 (a) together with the numerical simulations. They confirm that a longer propagation distance allows for further soliton shift, up to 2.07 μm for the MOF length of 275 cm. For each segment, the coherence degree has been measured with the same method as previously. The results are depicted in Figure 3.8 (b). As the length of the fiber increases, a coherence degradation is observed. This interesting observation leads to a conclusion, that since the fiber length can be adjusted for desired spectral soliton shift, the pulse properties, such as coherence, can be negatively affected. Therefore, for the applications in various laser systems, it would be a good idea to use as short segment of a MOF as possible.

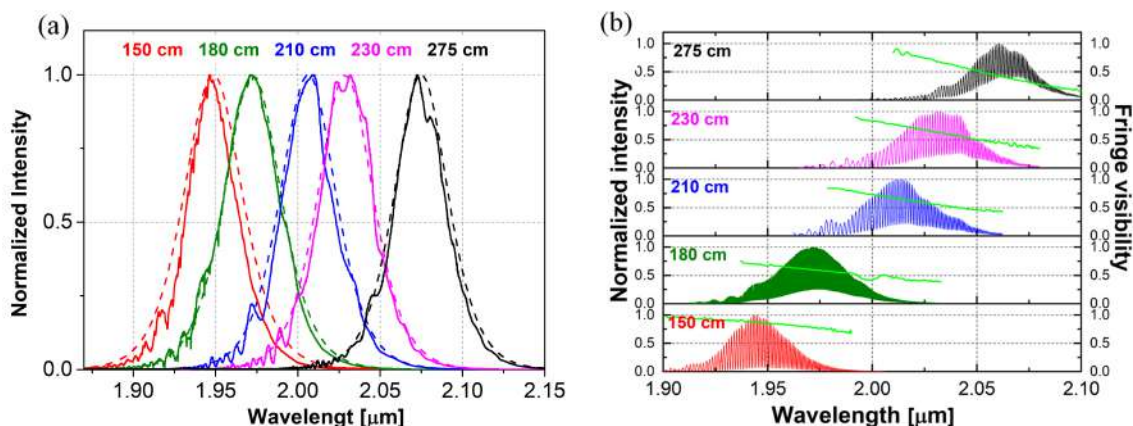


Figure 3.8: The spectral soliton shift as a function of fiber length for five different propagation distances in case of 1.55 μm pumping (solid lines) together with the numerical results (dashed lines) (a); coherence measurements for corresponding propagation lengths (b).

3.3.3 Polarization extinction ratio measurements

A useful measure, widely implemented to estimate how well the light is confined in a principal polarization linear mode, is a polarization extinction ratio (PER) parameter [153, 154]. For a polarized light signal that is transmitted onto a polarized filter and an analyzer, PER can be defined as the power of the signal when the two polarization axes are aligned ($P_{\text{pass axis}}$) compared to the power of the signal measured when the axes are crossed ($P_{\text{cross axis}}$):

$$\text{PER}(\text{dB}) = 10 \log_{10} \left(\frac{P_{\text{pass axis}}}{P_{\text{cross axis}}} \right) \quad (3.1)$$

In case of coupling the light to the birefringent fiber, as it has already been mentioned, the light is adjusted to be coupled to the slow axis of the fiber. However, there is usually a small polarization cross-talk and some amount of power is excited in the fast axis. In

this case PER is defined as the ratio between the amount of power in the slow axis to the light excited in the fast axis:

$$\text{PER}(\text{dB}) = 10 \log_{10} \left(\frac{P_{\text{slow axis}}}{P_{\text{fast axis}}} \right) \quad (3.2)$$

For the ideal system the PER value is infinite. However, usually, the value of this parameter for high birefringent systems is in the range of 20-30 dB. The experimental setup consisting of a half-wave plate (HWP), two aspherical lenses (AL), a MOF fiber and a polarizer (P) is presented in Figure 3.9. The position of the HWP was adjusted to match the slow or fast axis of the fiber. One of the aspheric lenses was used to couple the light into the fiber and the other to collimate the light from the fiber. The polarizer can be aligned to propagate the light in either a slow or fast axis. The spectra were recorded with the OSA.

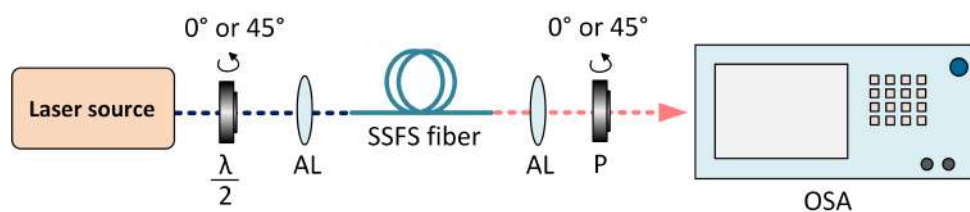


Figure 3.9: Experimental setup for polarization extinction ratio (PER) measurement. AL: aspherical lens, P: polarizer, OSA: optical spectrum analyzer.

The recorded spectra of the PER measurement for the YDFL pumping are presented in Figure 3.10. The measurements were performed for three different laser power levels, so that the solitons were centred at three chosen wavelengths: 1460, 1540 and 1640 nm. This procedure allows for spectral dependence investigation of the soliton's PER. PER measurements were performed for slow and fast axis. A blueshift of the solitons is observed in case when the fast axis is excited, and therefore the solitons are centered at 1440, 1490 and 1550 nm. In case of alignment to the slow axis (subfigures a, c, e), the PER magnitude increases with the spectral redshift, from 11 dB at 1460 nm, reaching 14 dB at 1640 nm. In the situation where the input polarization is aligned to the fast axis (subfigures b, d, f), the values of PER are 1-2 dB lower for each corresponding soliton, reaching 13 dB at maximum for soliton at 1550 nm.

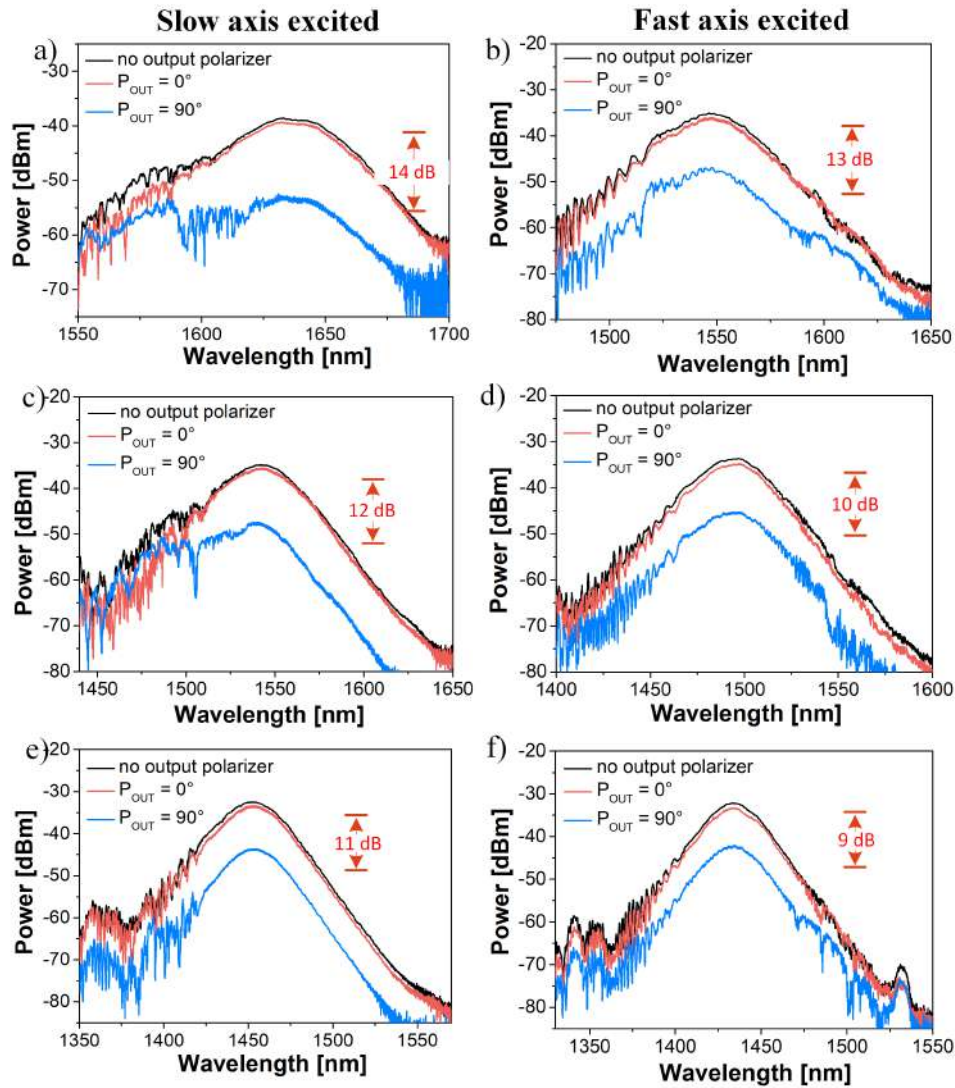


Figure 3.10: PER measurement results of the fabricated MOF under YDFL pumping for three soliton wavelengths: 1460 (a, b), 1540 (c,d) and 1640 nm (e,f). Left column shows the results for slow axis alignment, right column presents spectra for fast axis. Black lines correspond to the spectra measured without the polarizer. Blue and red lines represent the spectra registered with the polarizer aligned for transmission and blocking, respectively. The angles are with respect to the fiber slow axis.

The spectra of the PER measurement for the EDFL pumping are depicted in Figure 3.11. It is observed that in this case the PER values are significantly higher, namely in the range of 25-26 dB for polarization alignment in the slow axis and in the range of 24-27 for the fast axis. The spectra recorded when the slow axis is excited are presented in Figures 3.11 a, c, and e, whereas the results for the fast axis are gathered in the right column, in Figures 3.11 b, d, and f. In Figures on the right, when the fast axis is excited, an additional spectral component is observable in the long-wavelength part of the soliton spectrum. This feature is known as *soliton trapping*, and can be a consequence of a difference in group velocities of slow and fast modes in a MOF.

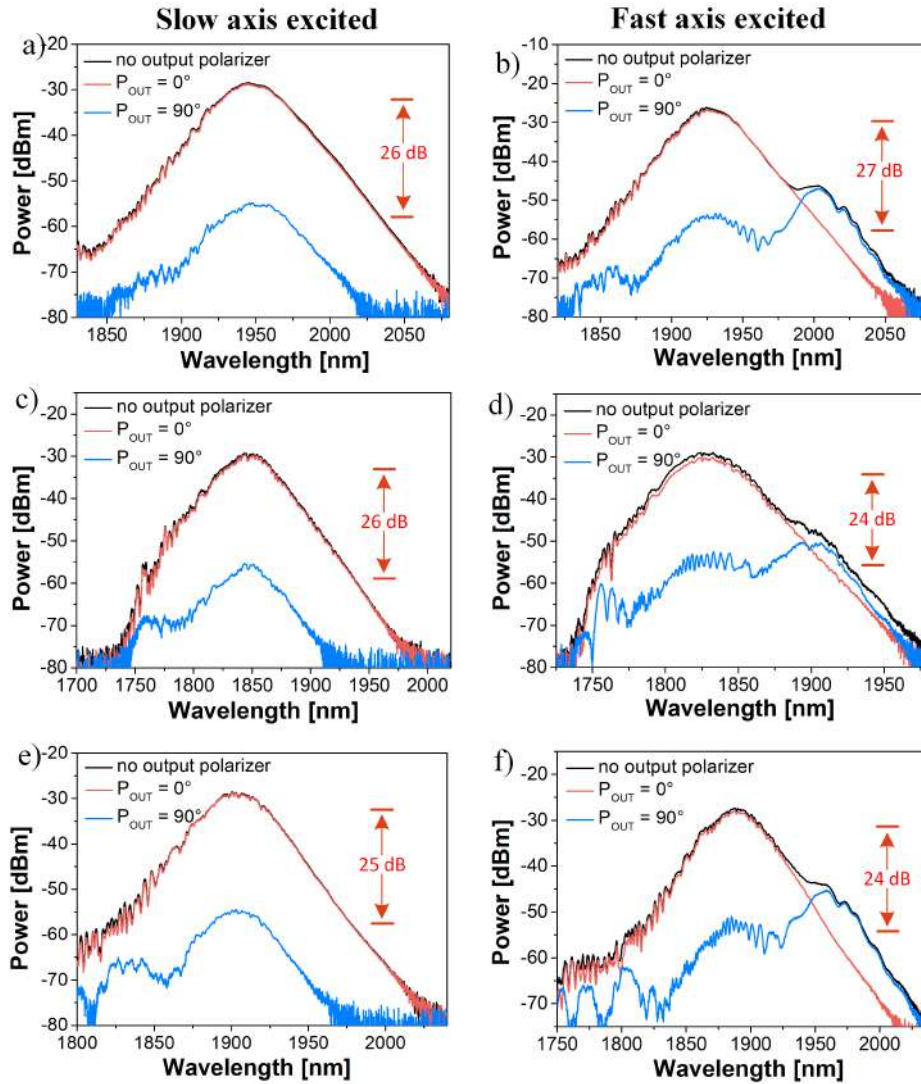


Figure 3.11: PER measurement results of the fabricated MOF under YDFL pumping for three soliton wavelengths: 1900 (a, b), 1850 (c, d) and 1800 nm (e, f). Left column shows the results for slow axis alignment, right column presents spectra for fast axis. Black lines correspond to the spectra measured without the polarizer. Blue and red lines represent the spectra registered with the polarizer aligned for transmission and blocking, respectively. The angles are with respect to the fiber slow axis.

3.4 Conclusions

In this Chapter, the SSFS effect generated in a microstructured silica fiber for two pumping laser sources: $1.55 \mu\text{m}$ and $1 \mu\text{m}$ has been demonstrated. The frequency-shifted solitons were widely tunable up to $1.67 \mu\text{m}$ when pumped with YDFL at $1 \mu\text{m}$ and up to $1.95 \mu\text{m}$ when using EDFL operating at $1.55 \mu\text{m}$. It was verified that using longer segments of the MOF, the spectral shift can be enhanced up to $2.05 \mu\text{m}$. When pumped with YDFL, the generated spectral bandwidth covers the $1.3 \mu\text{m}$ band, which is of interest of OCT and the $1.55 \mu\text{m}$ band, which covers the bandwidth of Erbium gain media. For EDFL pumping, the generated optical solitons cover the wavelength range between 1.65

and $1.95 \mu\text{m}$, which also stands for the bandwidth of the Thulium gain media, therefore, they can be used as seed sources For Tm-doped fiber amplifiers. In both pumping schemes, the conversion efficiency for the generated solitons was higher than 20%. What is more, it was verified that both, the coherence and the polarization extinction ratio parameter for the Raman solitons were high enough to use the fabricated fiber in setups for tunable sources used in various areas, including spectroscopy, imaging, frequency-combs or as seedings for fiber amplifiers.

Chapter 4

ANDi supercontinuum and SSFS as seed sources for Thulium-doped fiber amplifiers

4.1 Introduction

Recently, ultrafast lasers operating in the $2\ \mu\text{m}$ regime have attracted attention due to their potential as sources for multiphoton microscopy [155], mid-infrared frequency combs [156], absorption spectroscopy [157] and microsurgery [158]. The applications involving $2\ \mu\text{m}$ sources are very demanding as they require wide spectral bandwidth, proper stability, satisfactory noise properties, and high coherence. The common way to obtain a laser source in this wavelength range is through direct emission, namely, to combine the Tm or Ho gain media with various mode-locking techniques, e.g. graphene [159], carbon nanotubes [160], semiconductor saturable absorber mirrors (SESAMs) [161], or nonlinear polarization evolution [162]. Although these sources can reach kilowatt peak power levels, they usually feature limited spectral bandwidth. What is more, such sources do not offer tunability, and the cost of components is usually very high. The alternative approach includes utilizing nonlinear effects such as supercontinuum and SSFS with widely used and affordable mode-locked Erbium-doped (Er) fiber lasers. A number of research studies is currently devoted to analyzing noise properties, such as Relative Intensity Noise (RIN) of the assembled sources. Simultaneously, the supercontinuum generated in all-normal dispersion fibers (so-called ANDi-SC) emerged as a potential low-noise seeding solution. However, the discussion of whether nonlinear dynamics (including spectrally-shifted solitons) generated in the anomalous dispersion regime lead to significantly higher sensitivity and quantum noise when compared to ANDi-SC is still ongoing.

In this Chapter, a comprehensive study on the stability, noise properties and coherence of both the SSFS and SC effects is presented. The generation of the spectrally-shifted solitons and supercontinuum in optical fibers with different dispersion regimes is described with the demonstration of the numerical simulations of both effects. Eventually, the experimental work is shown and the comparison between these two different types of

ultrashort sources is discussed. The emphasis is put on the comparison of different types of nonlinear fibers in terms of their stability and noise properties.

4.2 Spectral conversion for 2 μm laser sources: SSFS and ANDi-SC

The principles of the SSFS phenomenon have already been described in Section 2. Due to the stimulated Raman scattering, one part of the ultrashort pulse spectrum can experience gain at the expense of the other part. As a result, the pulse traveling in an optical fiber, can shift towards longer wavelengths in the form of an optical soliton. To obtain soliton at 2 μm one can simply use a relatively well-known Er-doped fiber laser at 1.55 μm and pump the optical fiber with an ultrashort pulse. The possibility to employ a nonlinear fiber for SSFS allows for using a shorter segment of the fiber in the laser system, even below 1 m when compared to at least several meters of SMF. The air-silica microstructured fibers are birefringent can even be spliced with standard SMFs with the splice loss reduced to 0.4 dB [163]. The example of the SSFS effect generated in a MOF is presented in Figure 4.1 (a). Since the soliton tuning is a function of the input power, by simply changing the laser power to the fiber (P_{in}) we can set the wavelength position of the optical soliton.

The tunable solitons generated through the SSFS effect proved to maintain coherence [58, 64] and can serve as seedings for Thulium-doped fiber amplifiers [58]. They were also reported to exhibit high performance when considering other noise dynamics, such as relative intensity noise (RIN). The values of RIN for soliton seedings are usually between 0.2-0.7% [164, 165]. In [164], Coluccelli et al. demonstrated a high-power frequency comb seeded by frequency-shifted solitons. The setup featured 0.3% RIN integrated over the frequency range of 1 Hz-10 MHz which was 2 times larger than the RIN of the seed. In [165], Authors presented a Tm-Ho-doped amplifier fiber operating at 1.9 μm seeded by Raman solitons that exhibited RIN values of 0.6% (integrated over 1 Hz-1 MHz) which claimed to be 4 times higher than RIN of the seed.

Whereas the mechanism of the SSFS is quite straightforward and related directly to the stimulated Raman scattering, the origins of the supercontinuum are more complex which has already been described in Chapter 2. Although the generation of supercontinuum allows for obtaining source at wide range of wavelengths, its applicability can often be reduced due to modulation instability (MI) that arise in anomalous dispersion regime. The noise performance of the sources based on SC generated in anomalous dispersion fibers is significantly degraded when compared to Er-doped fiber lasers that serve as seeds. It is due to the induction of the excess amplitude and phase noise during the nonlinear broadening process, and then further increasing this noise in the amplifier stage. A few years after Ranka's demonstration, a novel version of supercontinuum was demonstrated in a MOF with normal dispersion profile [166]. The example of the ANDi-SC phenomenon generated in a MOF is presented in Figure 4.1 (b).

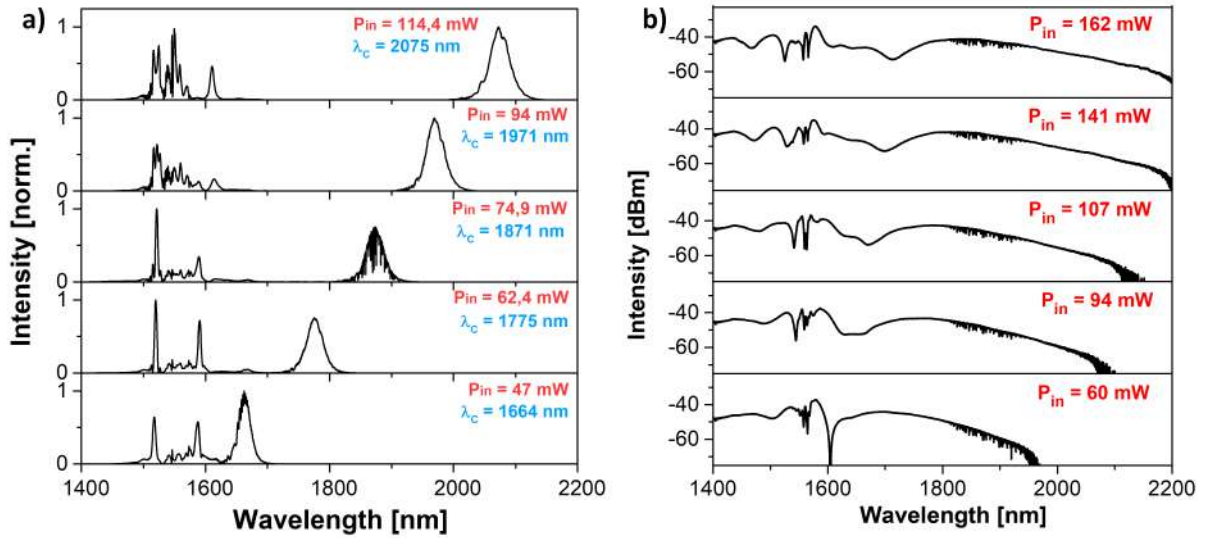


Figure 4.1: The example of an SSFS (a) and an ANDi-SC (b) generated in a MOF.

First works on ANDi-SC have already proved that it exhibits a higher degree of coherence and lower RIN when compared to the anomalous dispersion regime [166, 167]. This can be the result of different origins than for the SC in anomalous dispersion domain. In case of an ANDi fiber that is pumped by femtosecond laser pulses, the SPM and optical wave-breaking (OWB) are the main effects responsible for spectral broadening [107].

Due to its excellent properties, the supercontinuum generated in normal-dispersion fiber has also emerged as a suitable low-noise seed source for Tm-doped amplifiers [168, 169]. In [169], Authors demonstrated Tm/Ho-doped fiber amplifier seeded by ANDi-SC that exhibited 0.07% integrated RIN over the frequency range of 10 Hz-20 MHz which corresponded to only a 1.5 noise amplification factor. In [168], Rampur et al. showed 0.047% integrated RIN over the frequency range of 10 Hz-10 MHz for a Thulium-doped fiber amplifier seeded by ANDi supercontinuum.

Although these two nonlinear phenomena, SSFS and supercontinuum, have different origins, both have been proved to be successfully used as seedings for fiber amplifiers operating at 2 μm regime. And, since a number of research studies was devoted to investigate noise properties of the ANDi-SC comparing to SC in anomalous dispersion regime, a possible conclusion would be, that in general, normal dispersion domain provides more suitable sources for high-demanding applications, such as spectroscopy and precision measurements. However, this should not be exactly truth. In fact, for Tm-doped fiber amplifiers purposes, frequency-shifted solitons seem to be more suitable as they can provide a high degree of coherence and a smooth spectral shape. What is more, they offer easy wide tuning, therefore, they easily match the required spectral range so that one can benefit from the highest gain of the amplifier.

The general idea of the comparative study on SSFS and ANDi-SC

The results of the study that is going to be presented in this Chapter have been

published in [63]. As there had been no direct comparison between the SSFS effect and ANDi-SC in the literature, our goal was to fill this gap. All experimental measurements were performed by the Author, and the numerical part of the experiment was done in a collaboration with the Faculty of the Fundamental Problems of Technology from our University. The nonlinear fibers that were used for this experiment were produced by our collaborators from the Laboratory of Optical Fiber Technology in Lublin.

Specifically, the aim of this experiment was to quantitatively compare two different types of nonlinear effects generated in the $2 \mu\text{m}$ wavelength range. For this purpose, two nonlinear fibers were used. Both fibers were air-silica microstructured fibers that were fabricated from a very similar preform and made from the same glass composition, but drawn at the tower with different parameters. In both cases, the cladding consisted of an air-hole structure with bigger air-holes on the both sides of the core. The structure of each fiber is presented in Figure 4.2. The nonlinear fibers feature the same core diameter of $2 \mu\text{m}$, but they differ in fiber nonlinearity. The nonlinear coefficient, γ amounts to $7.7 \text{ W}^{-1}\text{km}^{-1}$ for the SSFS fiber (the cross-section presented in Figure 4.2 a), and $9.8 \text{ W}^{-1}\text{km}^{-1}$ for the ANDi fiber (cross-section shown in 4.2 b)).

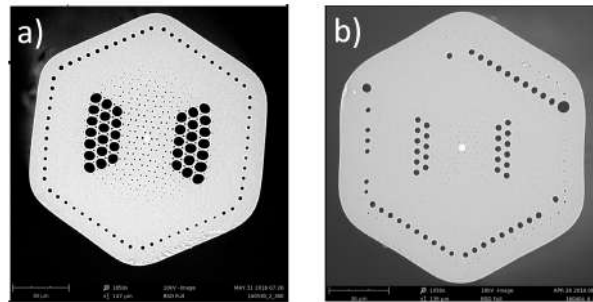


Figure 4.2: The fibers' cross-section (SEM images): (a) the SSFS fiber, (b) the ANDi-SC fiber.

Such a design of the fiber structure provides polarization-maintaining inside the fiber and also the proper dispersion characteristics. Dispersion profiles of the fibers are presented in Figure 4.3. The nonlinear fiber adjusted for the SSFS effect (its dispersion is presented in Figure 4.3 a)) possesses the ZDW at $1.3 \mu\text{m}$. Therefore, for $1.55 \mu\text{m}$ pumping it provides the anomalous dispersion regime (D coefficient > 0 , $\beta_2 < 0$). When it comes to the other nonlinear fiber, with dispersion profile presented in Figure 4.3 b), one can easily notice that there is no ZDW and the entire dispersion curve is in the normal dispersion regime (D coefficient < 0 , $\beta_2 > 0$).

4.3 Experimental setup

The experimental setup is presented in Figure 4.4. The Er:doped oscillator generating 335 fs pulses at 125 MHz repetition rate serves as a seed source. The laser has been built in our laboratory, based on passive mode-locking with the use of graphene. The details of the setup are in the work [126]. The femtosecond pulses from the oscillator are then

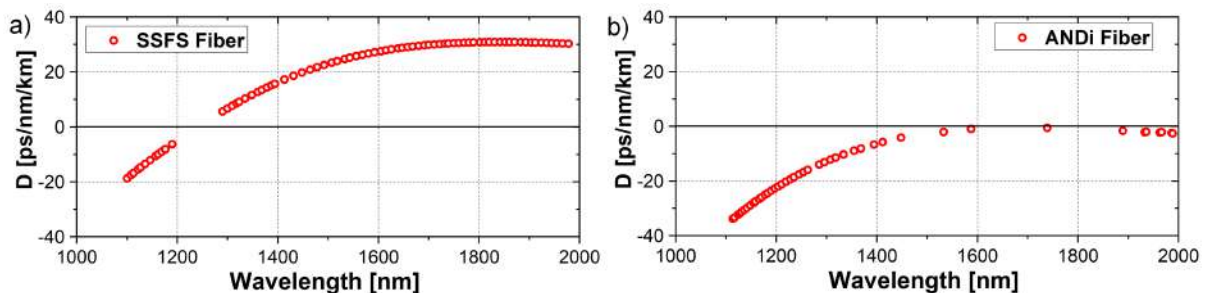


Figure 4.3: The measured dispersion profiles of the nonlinear fibers used in the experiment: (a) the SSFS fiber, (b) the ANDi-SC fiber.

provided through a 99/1 optical coupler to the polarization-maintaining Er-doped fiber amplifier (PM-EDF) which was built in the chirped-pulse amplification scheme. In such configuration, mode-locked pulses are first stretched in a normal dispersion fiber (here, a gain fiber), then amplified in an Er-doped amplifier, and eventually are compressed in the SMF that possesses an anomalous-dispersion profile. The amplifier consists of two filter-type WDMs, and a 131 cm-long Er-doped fiber (nLight Liekki Er80-4/125-PM-HD). Two single-mode 980 nm diode pumps were used to pump the gain fiber. In the final stage, the pulse was compressed in a short segment of PM-SMF (Coherent PM-1550 XP), which features anomalous dispersion.

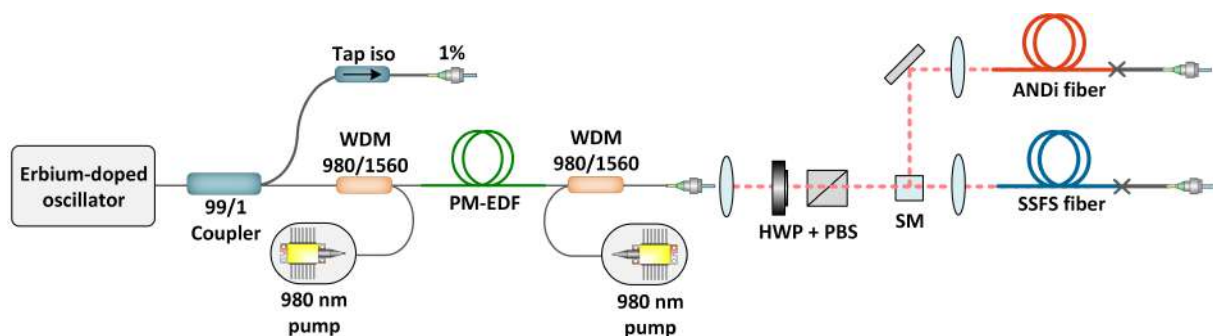


Figure 4.4: Experimental setup for ANDi-SC and SSFS characterization (WDM: wavelength division multiplexer, PM-EDF: polarization-maintaining Erbium-doped fiber, HWP: half-wave plate, PBS: polarizing beam-splitter, SM: switchable mirror); (b) cross-section image of the ANDi and (c) SSFS fiber.

The characterization of the output pulses from the amplifier is presented in Figure 4.5. The autocorrelation presented in Figure 4.5 (a) indicates that the source laser generated a sech^2 -shaped pulses with low-intensity side lobes and the pulse duration was 50 fs. The optical spectrum of the laser amplifier presented in Figure 4.5 (b) shows that the bandwidth of the pulse spectrum was 61.6 nm. The RF spectrum is depicted in Figure 4.5 (c) with the first harmonic at 125.0275 MHz presenting that the signal-to-noise ratio is 65 dB. Figure 4.5 (c) also presents the 7 GHz span of the RF spectrum indicating the stable mode-locking of the laser source.

The laser beam was then provided via aspheric lenses to both nonlinear fibers. The

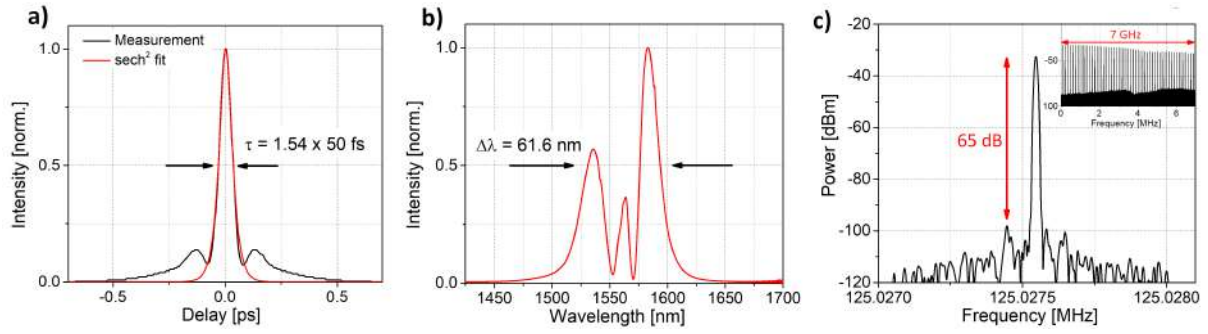


Figure 4.5: Autocorrelation of the laser pulse (a), the pulse optical spectrum (b), and the radio-frequency spectrum with the first harmonic and the 7 GHz span (c).

combination of a half-wave plate (HWP) and polarizing beam-splitter (PBS) played role of an attenuator. A switchable mirror (SM) was used to switch between two nonlinear fibers. In case of both nonlinear fibers a fiber connector was spliced to the fiber end. It is important to mention that both nonlinear fibers were placed at the same optical table and mounted on identical optomechanical stages (Thorlabs MAX313D), therefore, the measurements in case of both fibers were performed in the same laboratory conditions.

The generated spectra from both nonlinear fibers are presented in Figure 4.6, together with the numerical simulations. In the numerical model, as previously, the GNLS Equation was used to perform the calculations of the pulse propagating along the both fibers length. The initial pulse profile was retrieved from the actual autocorrelation measurement to reflect the experiment. The values of the effective mode-area for the ANDi fiber was $13.8 \mu\text{m}^2$ and the nonlinear parameter was $\gamma = 9.8 \text{ W}^{-1}\text{km}^{-1}$, whereas in case of the SSFS fiber it was $10.8 \mu\text{m}^2$, and $\gamma = 7.7 \text{ W}^{-1}\text{km}^{-1}$. Figure 4.6 demonstrates generated spectra in ANDi fiber (a) and SSFS fiber (b) for power levels varying from 60 mW to 162 mW. It can be noticed that the spectral coverage of both effects reaches up to 2200 nm.

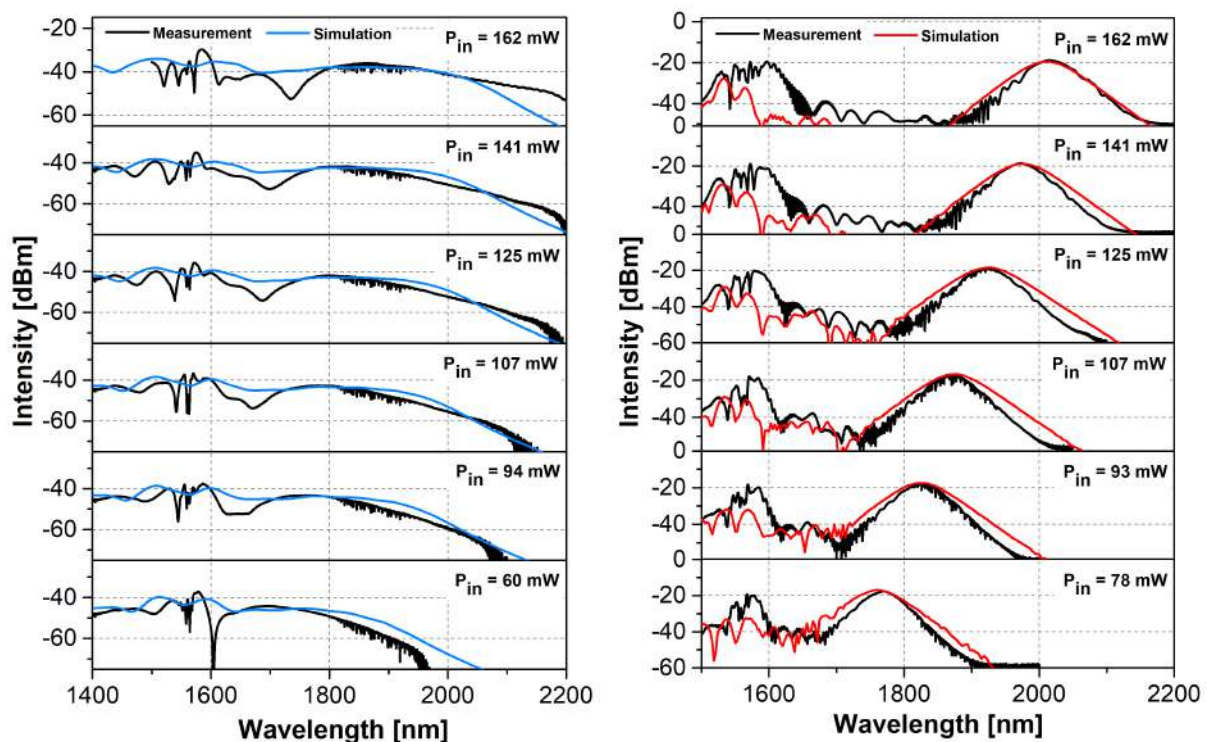


Figure 4.6: Measured and simulated spectra of the ANDi-SC (a) and SSFS (b) in both nonlinear fibers.

4.3.1 Measurement results

The next step was to investigate the noise properties of both nonlinear effects. The outputs of the fibers were provided to different setups built for this experiment. The results of the coherence measurements and DFT are presented below. Then, the setup of the Tm-doped fiber amplifier seeded with both effects is presented and temporal and spectral characteristics obtained from FROG measurement are discussed. The last part contains the RIN measurements which includes the amplitude noise investigation of each stage of the setup.

Coherence

The first property to investigate was the coherence of the output pulses from both nonlinear fibers. This property was measured with a fiber-based Michelson interferometer and the procedure was the same as presented in Figure 2.28, in Chapter 2, Section 2.7.2. The interferometer employed a 50/50% coupler (similar as in [131]) and was adapted to the 125 MHz repetition rate of the source. The difference in the arm length was 80.8 cm. The interference pattern was recorded with the use of an optical spectrum analyzer (Yokogawa AQ6375, OSA) with the resolution of 0.05 nm. The results of the coherence measurements for the ANDi fiber (a) and SSFS fiber (b) are presented in Figure 4.7. It can be noticed that the coherence is very high for both effects. In case of ANDi fiber, the V parameter is between 0.8 and 1 in the entire wavelength range, whereas for solitons it is around 0.9 up to 1900 nm. For longer wavelengths the coherence slightly degraded but the

V parameter is still very high: 0.8 for soliton at 1975 nm and between 0.6-0.8 for soliton at 2025 nm. The measurement revealed, that the SSFS is comparable to ANDi-SC in terms of coherence, and the anomalous dispersion of the fiber does not lead to coherence degradation of the frequency-shifted solitons.

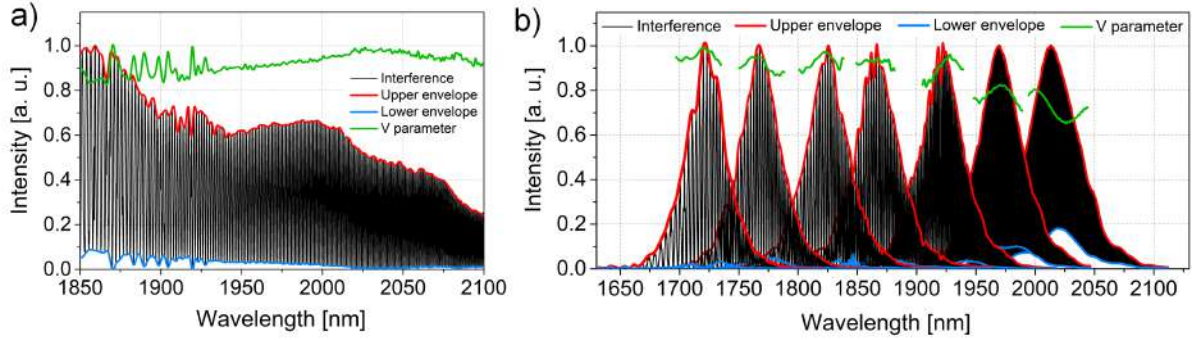


Figure 4.7: Coherence measurement results for ANDi (a) and SSFS (b) fiber.

DFT

To investigate the stability of both types of pulses, a DFT technique was employed. The measurement procedure was the same as described in Chapter 2, Section 2.7.1. In this scheme, a 487 m long SM1950 fiber (Fibrain Sp. z o.o.) was used as a stretcher. The fiber provided time-wavelength mapping which is graphically presented in Figure 4.8. Pulses from the dispersive fiber were detected by the photodetector (Discovery Semiconductors DSC2-50S) and recorded by the 6 GHz bandwidth oscilloscope (Agilent Infinium DSO90604A). At the same time, pulses were recorded with the optical spectrum analyzer to verify whether the temporal shape mimics the spectrum.

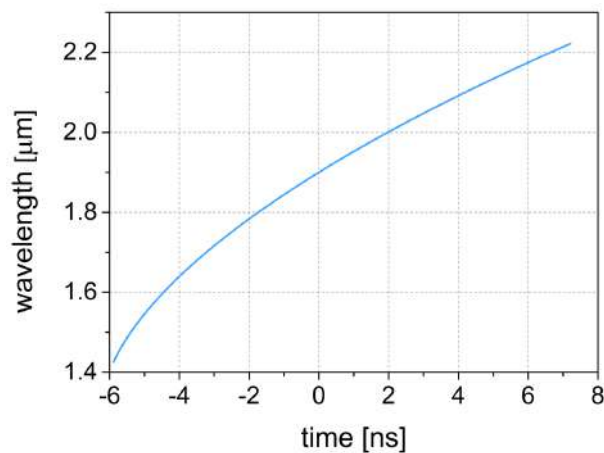


Figure 4.8: Time-wavelength mapping curve used for the DFT measurements of both ANDi-SC and SSFS.

With the use of 5000 traces and the time-wavelength mapping as presented in Figure 4.8 it was possible to obtain spectra demonstrated in Figure 4.9 and 4.10. By taking into account that the zero-dispersion wavelength of the used fiber is near $1.3 \mu\text{m}$, and the

time-wavelength mapping is not exactly determined for the wavelengths near that region, the spectra are limited to $1.65 \mu\text{m}$ on the short-wavelength side. The DFT was performed for the ANDi-SC and five different solitons centred at: 1858, 1894, 1925, 1953, and 1975 nm. Each trace was transformed to the wavelength domain (grey dots in the middle column of the Figure) and was drawn together with the spectrum obtained from the OSA (solid blue line). The averaged spectra (red line) are in an excellent agreement with the optical spectra registered from the OSA, which confirms the validity of the method of time-wavelength mapping.

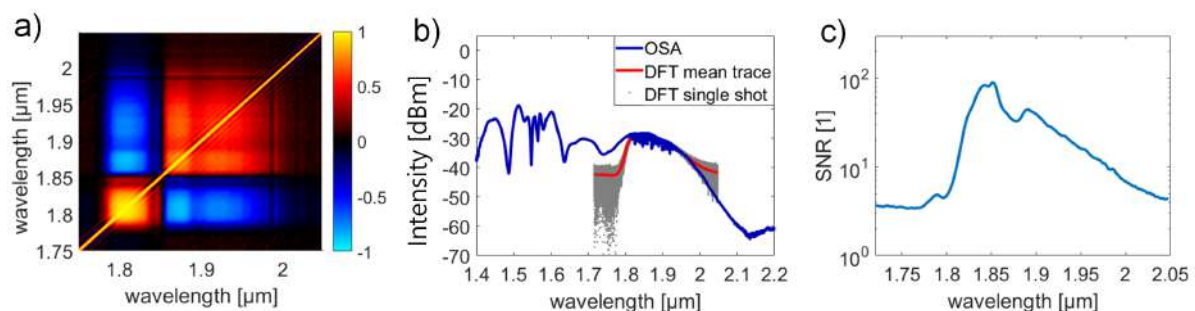


Figure 4.9: The results of the DFT measurements performed for ANDi-SC: correlation map (a); optical spectra from the OSA (blue line) and retrieved from the DFT: single shot measurements (grey dots) and the mean spectrum (red line) (b); the calculated SNR (c).

To compare the SNR for ANDi-SC and SSFS, a standard deviation of the intensity has been calculated for each case. The signal-to-noise ratio has been expressed as the ratio of the mean to the standard deviation and is presented in the right column in Figures 4.9 and 4.10. The resulting SNR for the ANDi-SC amounts to 90 at a maximum around $1.85 \mu\text{m}$. For the solitons in all cases the SNR is higher, for some of them exceeding even 200.

Lastly, the spectral correlation maps were calculated and the results are presented in the left column in Figures 4.9 and 4.10. The spectral correlation maps are used to estimate the timing jitter. When a pulse is shifted towards longer wavelengths from the central wavelength position, spectral intensities are changed as follows: they are increased at longer wavelengths and decreased at shorter wavelengths. The situation is the opposite when the pulse shifts towards shorter wavelengths. This mechanism can be expressed as a positive and negative correlation. Here, the contrast of the correlation maps is limited by the contribution of the random noise. There is also a difference between the SC and solitons' correlation maps, as the solitons possess narrower spectra than the supercontinuum. Therefore, the regions of the spectral correlations are also narrower in these cases.

The DFT investigation results indicate that both nonlinear effects are characterized by excellent shot to shot stability, despite different dispersion characteristics of the fibers. What is more, it was not observed that the Raman solitons suffered from an excessive shot-to-shot noise, which was previously observed in case of supercontinuum generation in anomalous dispersion fiber and linked to the particular dispersion regime [170]. Therefore,

we can conclude that the SSFS effect can generate pulses of as high stability as the pulses generated from the ANDi-supercontinuum.

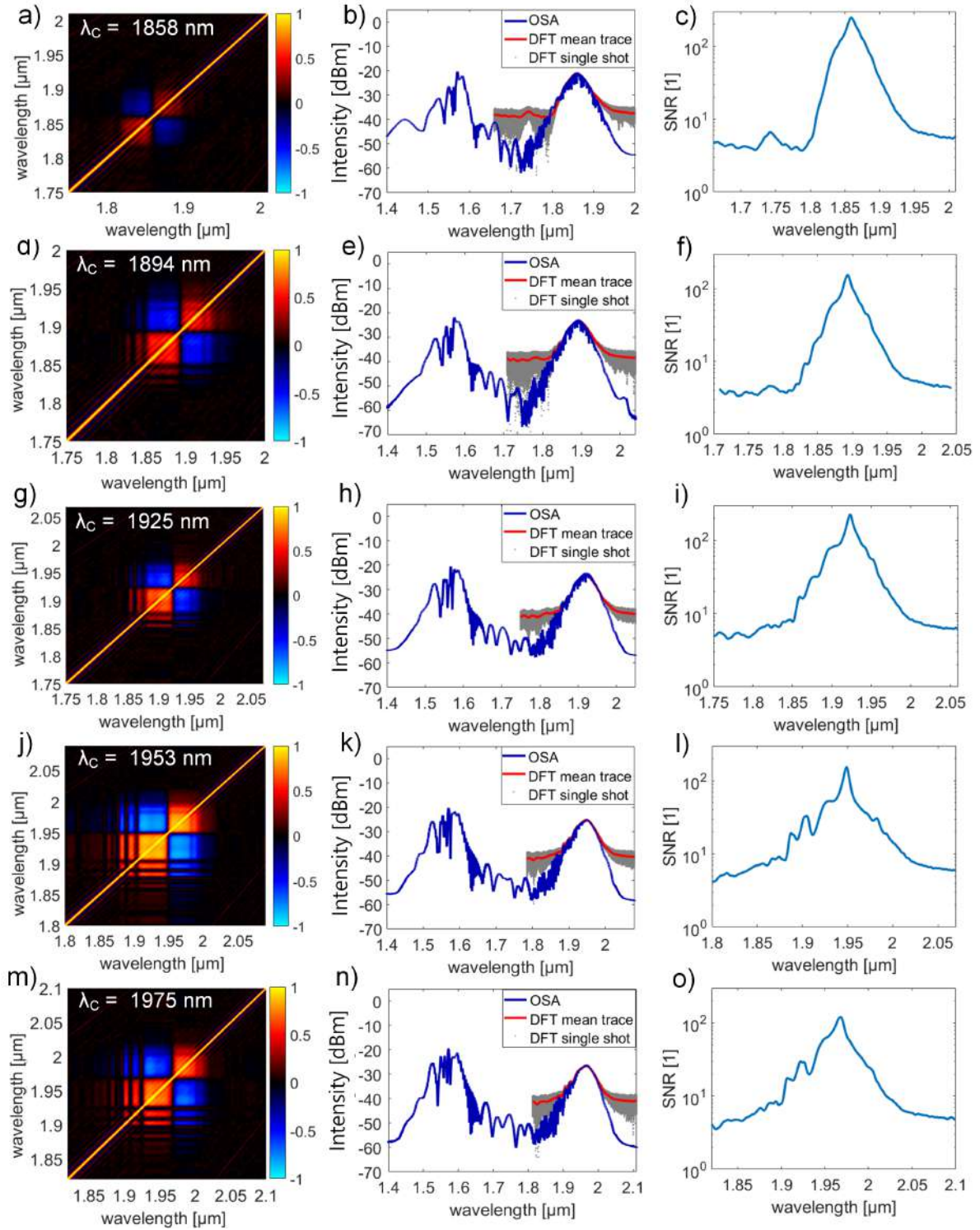


Figure 4.10: The results of the DFT measurements performed for the SSFS, for solitons centred at 1858, 1894, 1925, 1953, 1975 nm: correlation map (a), (d), (g), (j), (m); optical spectra from the OSA (blue line) and retrieved from the DFT: single shot measurements (grey dots) and the mean spectrum (red line) (b), (e), (h), (k), (n); the calculated SNR (c), (f), (i), (l), (o).

4.3.2 Tm-doped fiber amplifier seeded with ANDi-SC and SSFS

In the next step, both sources were utilized as seeds for a Thulium-doped fiber amplifier. The setup is presented in Figure 4.11. The amplifier was built in the chirped pulse amplification (CPA) regime. In the current setup, pulses are first stretched in a PM dispersion-compensating fiber (PM-DCF). The DCF possessed a value of the second-order dispersion β_2 of $0.075 \text{ ps}^2/\text{m}$ at 1950 nm . A 3 m -long DCF was used for the configuration with the SSFS fiber, and a 2 m -long segment for the setup with ANDi-SC fiber. The temporally-stretched pulses are then amplified in a Tm-doped fiber amplifier, where the Tm-doped fiber is pumped by a 1565 nm continuous-wave (CW) Erbium/Ytterbium-doped-fiber laser. The pump laser is provided to the amplifier through a $50/50$ optical coupler (OC) and two filter-type PM WDMs. Lastly, the pulses are compressed in a segment of PM-SMF (Coherent PM-1550 XP). A 94 cm -long segment of PM SMF was used to compress the pulse in the configuration with ANDi-SC, and segments of PM-SMF optimal for the Raman solitons were between 81 - and 134 -cm long. All fibers used in the Tm-doped fiber amplifier were polarization-maintaining. The output pulses from the amplifier were provided to the OSA (Yokogawa AQ6375B) and FROG (FROG Scan Ultra2, Mesa Photonics) for further analysis.

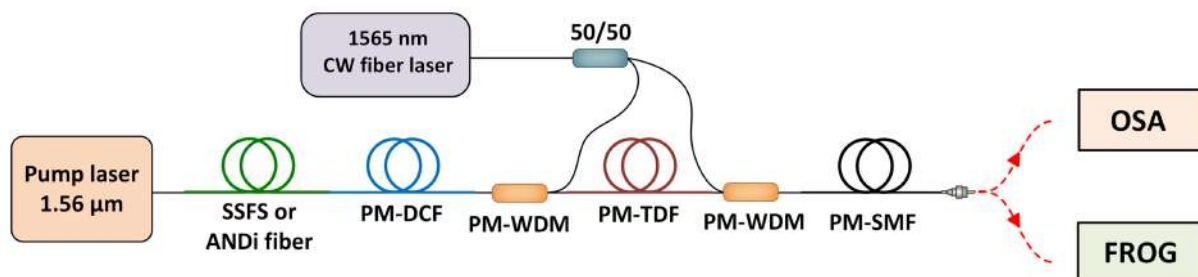


Figure 4.11: The Tm-doped fiber amplifier setup. PM-DCF: polarization-maintaining dispersion-compensating fiber; PM-TDF: polarization maintaining Tm-doped fiber; PM-WDM: polarization maintaining wavelength division multiplexer; PM-SMF polarization maintaining single-mode fiber; OSA: optical spectrum analyzer; FROG: frequency-resolved optical gating.

The results of performed measurements are presented in Table 4.1. The outcomes including pulse duration, average optical power and the energy of the pulse for the ANDi-SC and the corresponding soliton (centred at the same operating wavelength) are gathered with the best-achieved results for the soliton centred at 1950 nm . The configuration of the Tm-doped fiber amplifier seeded with ANDi-SC resulted in 92 fs pulses and 350 mW average optical power at a maximum, which corresponded to the 2.8 nJ of the pulse energy. Comparable but slightly better results were obtained for the soliton at 1870 nm : 88 fs pulse duration, 365 mW of average optical power and relating energy was 2.92 nJ . However, the shortest pulse was obtained for soliton at 1950 nm . The pulse was as short as 80 fs , possessed 400 mW average optical power and 3.24 nJ energy.

Table 4.1: Results obtained for Tm-doped amplifier seeded by ANDi-SC and Raman solitons.

Seed source	Pulse duration [fs]	Average optical power [mW]	Energy of the pulse [nJ]
ANDi-SC	92	350	2.80
SSFS @1870 nm	88	365	2.92
SSFS @1950 nm	80	405	3.24
SSFS @1970 nm	95	370	2.96
SSFS @1994 nm	107	278	2.22

The registered optical spectra from the OSA together with the results from the FROG measurements, including temporal pulse shapes, spectrograms, and temporal and spectral phase are gathered in Figures 4.12 and 4.13. The subfigures 4.12 (a) and 4.13 (a), (d), (g), (j) present the temporal shapes of the pulses and their temporal phase. One can notice that the phase is flat in the vicinity of the pulse centre in all cases. The middle column of Figures 4.12 and 4.13 (subfigures 4.12 (b) and 4.13 (b), (e), (h), (k)) demonstrate the pulse spectra and the spectral phase. The last column (Figures 4.12 (c) and 4.13 (c), (f), (i), (l)) shows the spectrograms obtained for each scenario.

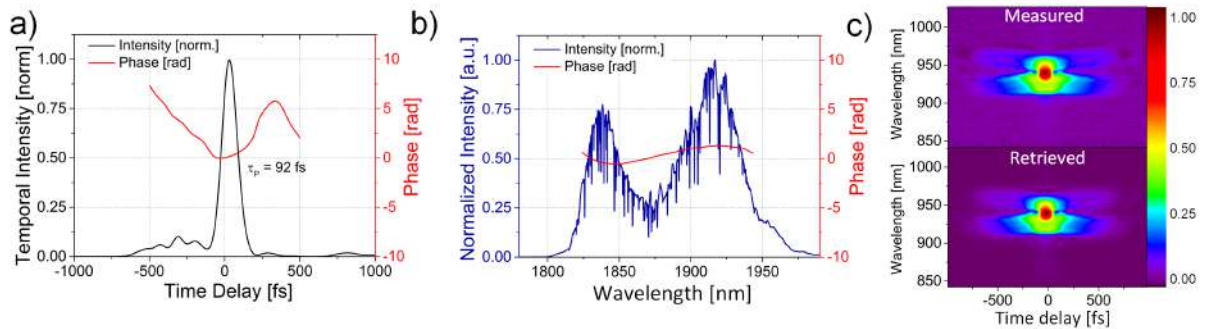


Figure 4.12: The characterization of the Thulium amplifier seeded by ANDi-SC using SHG FROG: (a) FROG-retrieved temporal intensity (black) and temporal phase profile (red); (b) FROG-retrieved spectral intensity (blue) and spectral phase profile (red); (c) Measured and retrieved FROG trace.

4.3.3 Relative intensity noise

The RIN measurements were performed following the procedure described in Section 2.7, Chapter 2 and illustrated in Figure 2.32. The measured signals were first detected by a low-noise photodiode (Thorlabs PDA10D2). Then, they were recorded by the oscilloscope (Rohde-Schwarz RTA4000). The value of the signal was maintained at the level of 1 V to avoid detector saturation. Next, each recorded trace is used in postprocessing: computer calculations transform the signals to the frequency domain by using Fourier transformation

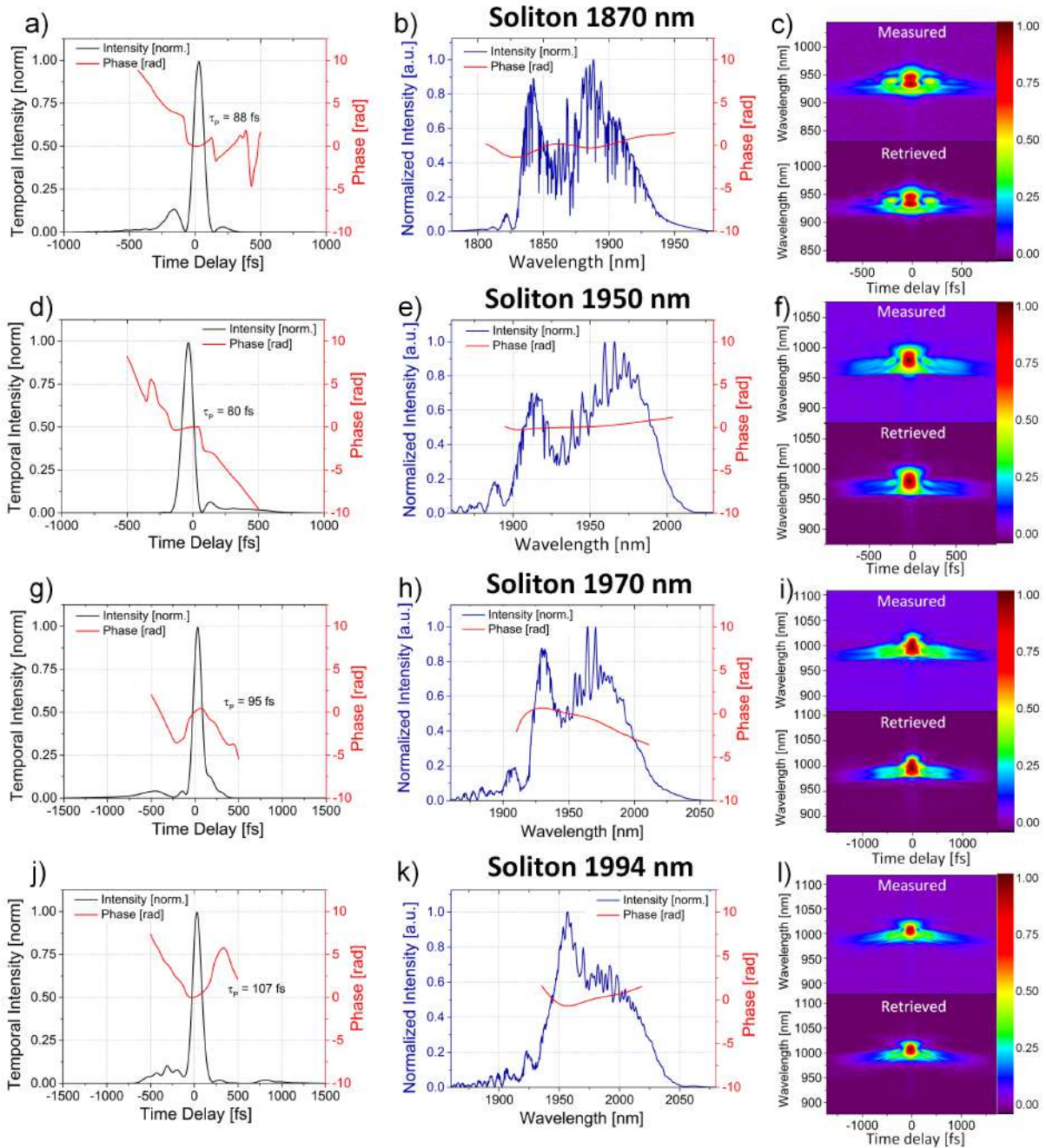


Figure 4.13: The characterization of the Thulium amplifier seeded by solitons centered at 1870, 1950, 1970, and 1994 nm; (a), (d), (g), and (j) FROG-retrieved temporal intensity (black) and temporal phase profile (red); (b), (e), (h), and (k) FROG-retrieved spectral intensity (blue) and spectral phase profile (red); (c), (f), (i), and (l) measured and retrieved FROG traces.

and the normalization by the mean value is performed. To increase the resolution of the amplitude, an oversampling method has been applied together with digital filtering by adding an anti-aliasing filter at the oscilloscope input. We also performed the averaging on 500 traces to reduce the noise. It needs to be pointed out that this procedure does not decrease the RIN peaks in the signal, it only makes it less noisy so that the individual peaks are more apparent in the signal. The results of the calculation establish the power

spectral density (PSD) of the signal over the frequency range of 10 Hz-500 kHz. The last step was to calculate the integrated RIN rms by integrating the PSD over the given frequency range. The procedure was performed for the femtosecond laser operating at 1550 nm, the outputs of both nonlinear fibers and the amplifier seeded by ANDi-SC and Raman solitons centred at a few chosen operating wavelengths. We also tested both CW pumping sources: the 980 nm CW laser diode that was used to pump the seed laser, and the 1550 nm CW pump laser used in the amplifier.

The results of the RIN measurements are presented in Figure 4.14 and Figure 4.15. Figure 4.14 (a) demonstrates the RIN expressed in [dBc/Hz] of the seed source and the nonlinear effects. Figure 4.14 (c) presents the results for the amplification stage. Figures (b) and (d) depict the integrated RIN of the corresponding sources. It can be noticed that the RIN of the 1550 nm femtosecond laser is close to the noise floor. The integrated RIN of this source amounts to 0.022%. The rms RIN values for the solitons are between 0.023% for the soliton centred at 1870 nm and 0.077% for the soliton at 1930 nm. The RIN of the ANDi-SC is 0.058%. These results show that the solitons can in fact outperform not only the ANDi-SC but also the results given in the literature (0.045% achieved by Rampur et al. in [168]). The results obtained for the Thulium amplifier together with the amplifier pump are presented in Figures 4.14 (c) and (d). The results for the ANDi-SC are comparable to the soliton centred at the same wavelength (1870 nm): the integrated RIN amounts to 0.128% for the SC and 0.153% for the soliton. The highest value of the integrated RIN is associated with the soliton centred at 1950 nm, the value reached 0.284%. These values are comparable to other amplifier sources reported in the literature (0.047 - 0.7 %). However, it needs to be emphasized that the Thulium amplifier was not specifically optimized for low-noise operation. In fact, the aim of this experiment was to compare different seedings for Tm-doped amplifier in terms of intensity noise under the same conditions. All the integrated RIN measures in this experiment are gathered in Table 4.2.

Table 4.2: Results of the integrated RIN.

Source	integrated RIN [%]
Femtosecond 1550 nm laser	0.022
ANDi-SC	0.058
Soliton 1870 nm	0.023
Soliton 1910 nm	0.024
Soliton 1930 nm	0.077
Soliton 1950 nm	0.033
Soliton 1970 nm	0.059
Amplified ANDi-SC	0.128
Amplified soliton 1870 nm	0.153
Amplified soliton 1950 nm	0.284

It has already been mentioned in this Chapter that the integrated RIN is a useful

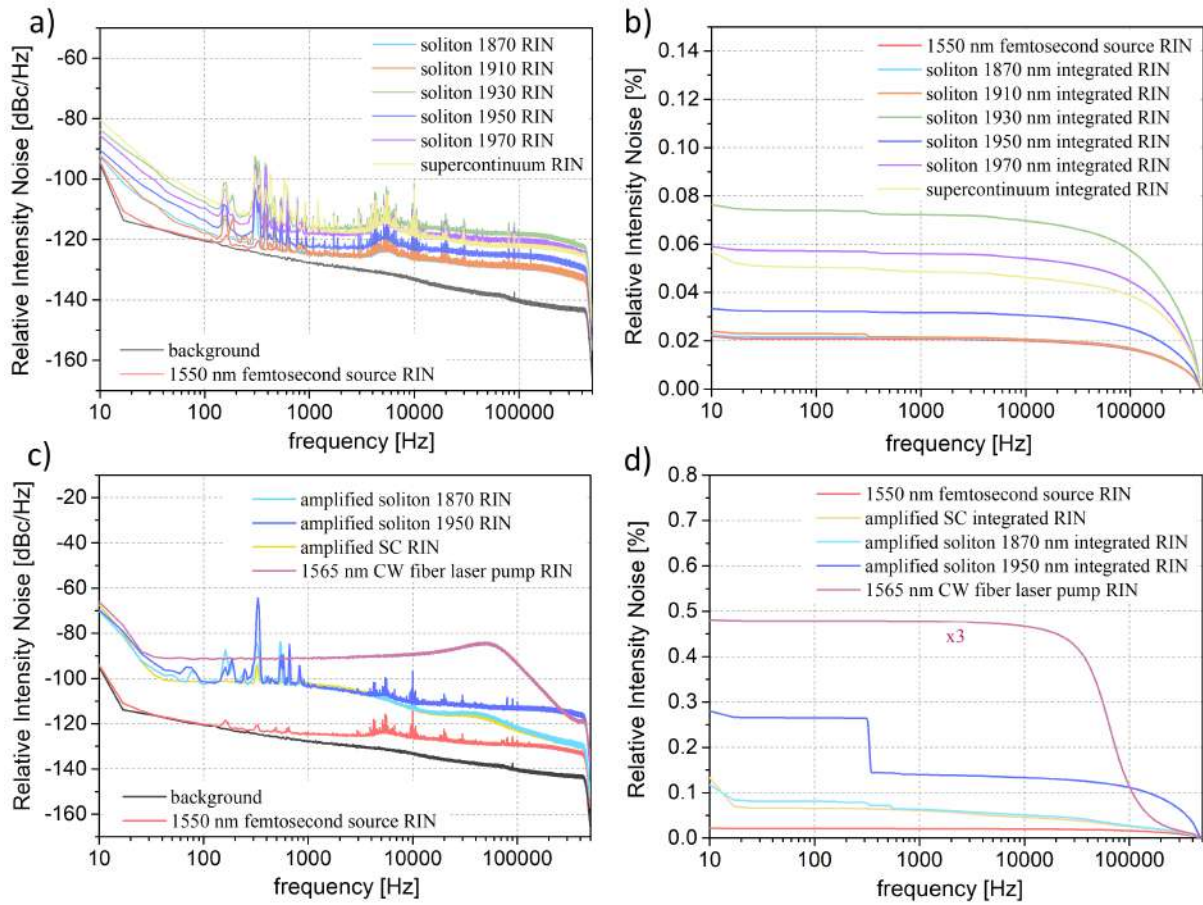


Figure 4.14: Relative intensity noise characterization: (a) RIN results for the 1550 nm femtosecond laser, ANDi-SC and solitons centred at 1870, 1910, 1930, 1950 and 1970 nm; (b) integrated RIN for 1550 nm femtosecond laser, ANDi-SC and solitons; (c) RIN results for the Thulium amplifier seeded by ANDi-SC and solitons centred at 1870 and 1950 nm and the 1565 nm CW fiber laser pump; (d) integrated RIN for the amplified solitons and SC, and the 1565 nm CW pump.

parameter to compare the results for different sources. However, to understand the possible origins of the source, one needs to concentrate on the analysis of the RIN variation over the frequency range which is presented in Figures 4.14 (a) and (c). The noise peaks < 1 kHz, which are visible in all traces, can be related to the free-space coupling of the light to the nonlinear fibers. Since the diameter of both fibers is very small, all thermal disturbances might cause intensity variation. One can also notice peaks in the regions of 100 Hz-1 kHz and 3 kHz to 100 kHz. These peaks appear in the trace of the 1550 nm femtosecond laser and are transferred to all the signals and are also amplified in the amplification stage. To verify the origins of that noise we measured the intensity noise of the 980 nm CW laser diode pump, which is used to pump the oscillator in the 1550 nm femtosecond source. The results are presented in Figure 4.15. It can be noticed that the noise peaks in the 1550 nm laser source RIN highly resemble the noise peaks from the 980 nm seed pump which are mainly caused by the laser diode driver. Probably, these noise peaks (in the regions of 100 Hz-1 kHz and 3 kHz-100 kHz) are first suppressed in the 1550 nm laser due to the

mode-locking operation and then transferred to next stages of the setup. Eventually, they are amplified in the Thulium amplifier. It was expected that the amplifier would provide the additional noise to the setup and looking at the results, the contribution of the noise in the traces of the amplified sources also comes from the 1565 nm CW pump.

The other feature that can raise questions is a difference in the intensity noise levels for solitons centred at different operating wavelengths. This behaviour has already been observed in [105] and is reported to be a consequence of the complex dynamics of the soliton propagation in the microstructured silica fibers. Also, there are other factors that can contribute to that. The detector responsivity can be different for different signal wavelengths. However, the maximal variation in the responsivity for different operating wavelengths is 7.8% at maximum, therefore, it should not cause such a discrepancy in the signal. Another factor is the gain profile of the Tm-doped fiber in the amplifier setup. It would explain the fact that the highest amplified soliton (at 1950 nm) also exhibits the highest intensity noise.

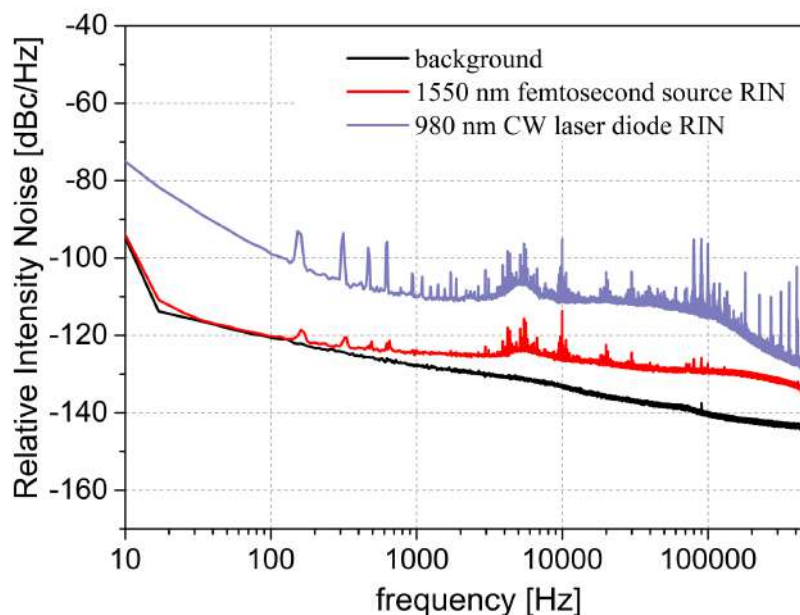


Figure 4.15: Intensity noise results measured for the 980 nm CW laser diode compared to the 1550 nm femtosecond source RIN.

Nevertheless, the results show that both the nonlinear processes: the ANDi-SC and the SSFS, exhibit comparable intensity noise before and after the amplification stage. The experiment confirmed that both nonlinear processes could be used as low-noise seed sources for Thulium-doped fiber amplifiers. The results obtained in this experiment have been gathered together with the outcomes from different laser systems based on nonlinear effects from the literature in Table 4.3. The amplifier setup can be adjusted specially for low noise performance reaching amounts of integrated RIN as low as 0.047%. However, as it was already mentioned, this was beyond the scope of this experiment.

Table 4.3: Results of the RIN for different laser systems from the literature.

Laser system	RIN [%]	Frequency range	Reference
High power frequency comb seeded by SSFS	0.3	1 Hz - 10 MHz	[164]
Tm/Ho-doped fiber amplifier seeded by SSFS	0.6	1 Hz - 10 MHz	[165]
Tm/Ho co-doped fiber amplifier based on ANDi-SC	0.07	10 Hz - 20 MHz	[169]
TDFA seeded by ANDi-SC	0.047	10 Hz - 20 MHz	[168]
TDFA seeded by SSFS	0.153	10 Hz - 500 kHz	this work
TDFA seeded by ANDi-SC	0.128	10 Hz - 500 kHz	this work

4.4 Conclusions

In this Chapter, a complete characterization of two different phenomena: SSFS and ANDi-SC has been presented. A comparative study on the seed sources for Thulium-doped fiber amplifiers based on ANDi-SC and SSFS in terms of noise performance has been conducted. A full analysis, including pulse-to-pulse coherence measurement, DFT, SHG-FROG and relative intensity noise, has been performed on both nonlinear effects in the same environmental conditions. Pulses generated in both configurations are characterized by a high degree of coherence, stability of the generated pulses and low-noise performance, however, with slightly better noise properties for the SSFS effect. Also, ANDi-SC and frequency-tunable Raman solitons are suitable as seeding for low-noise Tm-doped fiber amplifiers. To summarize, the SSFS effect, despite generation in anomalous-dispersion fiber, offers as high or even higher low-noise properties, such as stability, low intensity noise and high coherence, as the ANDi-SC, which proves the thesis.

Chapter 5

Spectral compression and amplification of the frequency-shifted solitons

5.1 Introduction

Narrow linewidth laser sources with high brightness have attracted attention due to their potential applications in nonlinear metrology, optical communication, coherent spectroscopy and Optical Coherence Tomography (OCT). With additional tunability possibility, they can be utilized for so-called swept-source OCT (SS-OCT) as they offer a broad spectral range with rapid tuning and narrow instantaneous linewidth. The OCT, which has emerged as a minimally-invasive method for cross-sectional imaging of biological tissues [171], has been widely examined for its applications in medicine and biology. There is, however, several requirements for the swept-source that is suitable for OCT. It has to be characterized with sufficiently narrow linewidth to provide a proper ranging depth of a few millimetres. Also, the sweep ranges of tens to 100 nm are desirable to ensure high axial resolution. First SS-OCT sources were based on semiconductor-optical amplifiers (SOAs) [65, 172], which covered a wide band but were relatively slow, with the sweeping rates up to kHz. Later, the Fourier-domain mode-locking (FDML) lasers were introduced, offering sweep as fast as 300 kHz and 100 nm tuning range [66]. The FDMLs have dominated the area of the light sources for the SS-OCT, however, being limited to the 1300 nm spectral window. Recently, the 1700 nm bandwidth has emerged as promising for biomedical imaging as it offers lower scattering in tissue and increased penetration depth [67–69, 173]. Figure 5.1 presents the effects of scattering and absorption in a biological tissue showing that 1.8 times more photons reach 1 mm depth with the use of a 1700 nm spectral window compared to the 1300 nm [173]. Regions shaded in orange demonstrate areas where at least 50% of photons are absorbed. The 1700 nm spectral range has already been successfully used for biological imaging, specifically for deep tissue imaging of a mouse brain [67].

Nevertheless, the standard technical problem with this spectral range is that the 1700 nm wavelength falls in a gap between available active media, between Erbium, Thulium

and Holmium. As a solution to this, nonlinear effects can be employed to allow for a spectral shift from 1500 nm using widely available and relatively cheap Erbium-doped laser and anomalous dispersion fibers. However, the tunable pulses that are generated utilizing the nonlinear effects usually are characterized by broad spectra, even > 30 nm [64, 174], as shown in Chapter 3. Therefore these methods, in order to be employed as sources for SS-OCT, must also provide spectral compression of these solitons to the linewidths even below 1 nm.

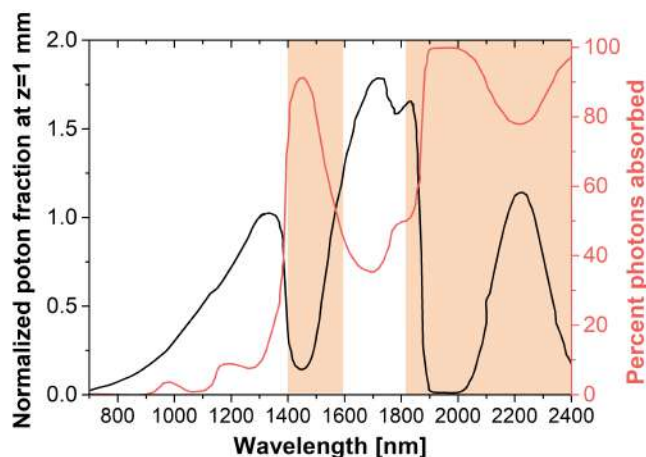


Figure 5.1: Effects of scattering and absorption in biological tissue: photon fraction at a 1 mm depth (black line), calculated percentage of absorbed photons (red line), taken from [173]. Orange-shaded regions demonstrate areas where 50% and more photons are absorbed.

In this chapter, the fundamentals of spectral compression technique are going to be explained. The Author performed a comprehensive numerical analysis of the investigated effect, demonstrating that with the use of comb-profile fiber (CPF) it is possible to spectrally narrow optical pulses from the initial 15 nm to the level below 1 nm. The experiment employing nonlinear effects together with spectral compression technique in an all-fiber setup is going to be demonstrated. The results of this work have been published by the Author in [175].

5.2 Spectral compression technique

The concept of the spectral compression phenomenon has been recently analyzed experimentally [176–180] as well as numerically [181–183]. It has been reported that the self-phase modulation (SPM) effect with proper initial conditions can lead to pulse spectral narrowing [54, 184]. The SPM has already been briefly described by the Author in Chapter 1. It is a nonlinear phenomenon usually responsible for pulse spectral broadening (and, hence, temporal compression), and widely utilized in all-fiber CPA systems to compensate dispersion of the fiber during an ultrashort laser pulse propagation. Indeed, the SPM's role is to redistribute the energy to the pulse's spectral components as a consequence of intensity-dependent nonlinear phase shift φ_{NL} . Because the nonlinear phase shift is

proportional to the pulse intensity ($\delta_\omega(t) \propto |E(t)|$), it causes a frequency upshift of the pulse trailing edge ($\delta_\omega(t) > 0$) and a downshift of the leading edge ($\delta_\omega(t) < 0$). Specifically:

$$\delta_\omega(t) = \frac{\partial \varphi_{NL}}{\partial t} \propto |E(t)|^2. \quad (5.1)$$

The behavior of the SPM strictly depends on the pulse's initial chirp. In case of positive chirp, the long-wavelength components are on the leading edge, and the short-wavelength components are on the trailing edge, therefore, the pulse is being broadened. In an opposite scenario, the long-wavelength components are on the trailing edge, and the short-wavelength belong to the leading edge. Both short- and long-wavelength components are shifted towards the centre part of the pulse and the pulse gets spectrally compressed. It has been reported that proper pre-chirping of the initial pulse results in pulse compression which is attributed to SPM [184].

The spectral compression effect has been first observed in SMF fiber [176]. Since then, the realizations in photonic-crystal fibers [177–179, 185] as well as in gain fibers [180, 184] have been demonstrated. These systems, however, lacked a sufficient tuning possibility which is crucial for SS-OCT sources. The solution to this problem has been proposed by Nishizawa et al. in [186]. The approach was to combine the spectral compression effect with the benefits from the SSFS effect in anomalous dispersion fibers. As a result, the Authors obtained a widely tunable source in the wavelength range of 1650-1900 nm. The idea was to provide an ultrashort pulse to a fiber in which dispersion is gradually increased along the fiber length. This method was called *adiabatic soliton spectral compression*. It is based on the soliton concept, which mathematically is referred to as the solution of NLS equation and, as a result of the nonlinearities/dispersion interplay is described as a wave packet that maintains its shape with propagation. The soliton order is given [6]:

$$N^2 = \frac{\gamma P_0 T_{FWHM}^2}{3.11 |\beta_2|} \quad (5.2)$$

where γ is fiber nonlinear coefficient, P_0 represents a peak power of the input pulse, T_{FWHM} is pulse duration and the symbol β_2 describes the second-order dispersion. When a soliton with the order N between 0.5 and 1.5 is provided to an optical fiber, it is going to change its shape to become a fundamental soliton whose order is 1. Therefore, when β_2 is linearly increased with the propagation length, the pulse will get temporally broadened as the T_{FWHM} also increases. And to maintain the fundamental soliton condition the pulse will be spectrally compressed.

To provide linearly increased dispersion in the fiber, a new type of fiber has been proposed. The fiber was based on the CPF technique which was initially used for pulse compression [187, 188]. In a CPF method, a fiber consists of a chain of alternating two different types of fibers: a standard telecommunication fiber, SMF and a dispersion-shifted fiber (DSF). These two fibers are spliced together with proper lengths in a manner that the average dispersion of a CPF fiber is increasing. Both SMF and DSF are commercially available for 1550 nm wavelength but their β_2 magnitudes differ significantly. As a result,

the fiber possesses dispersion of a shape as presented in Figure 5.2. When a laser pulse travels in such fiber it exhibits the influence of the nonlinear effects (mainly the SPM) in the zero-dispersion part of the CPF and the impact of the dispersion in the other parts. This method has been also used in [183]. The implementation of the CPF design in the

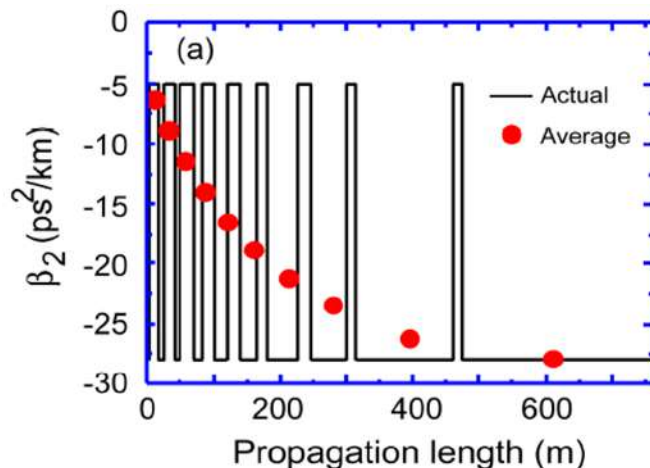


Figure 5.2: The comblike fiber dispersion profile adapted from [186].

lasers systems allowed for higher values of compression factor, up to 28 for the 1580 nm wavelength [182] or even 102.8 in the tuning range between 1580-1690 nm [189].

Later on, the spectral compression phenomenon was extensively studied numerically concentrating on optimizing the spectral compression factor and also lowering the pedestal components. However, the narrow-linewidth laser systems were still characterized by low power levels and usually also contained bulk optics. In [175], the Author et al. proposed an all-fiber narrow-linewidth system in the 1650-1900 nm wavelength range with an additional amplification stage in the 1700-1900 nm range. In this chapter, the extended version of the research is presented, which includes not only the model used in the experiment but also the simulations with the linearly increasing dispersion fiber.

5.3 Numerical model of the spectral compression technique

The numerical model to simulate the spectral compression phenomenon is based on the GNLSE (Eq. 2.26) which fundamentals have already been investigated in Chapter 2. The numerical simulations were performed in two configurations. The first one considered a situation where a parameter β_2 of the dispersion-increasing fiber was gradually increased along the propagation length. Actually, it is an ideal case as there are no such fibers currently available on the market. However, the Author believes it provides quite an important contribution to understanding the phenomenon. The second approach was to numerically simulate the CPF in a manner it could be later experimentally verified. This configuration is more complex, as it includes incorporating two different types of optical fibers. The CPF was combined of segments of SMF and DSF of different lengths

so that the laser pulse would propagate from one segment to another. Here, the numerical model was performed in a way that each segment of the fiber (SMF or DSF) served as a propagation length. This fact made the calculations relatively more time-consuming compared to the first approach.

5.3.1 Dispersion-increasing fiber at 1730 nm

In this Section, the Author investigates pulse propagation in a dispersion-increasing fiber at a wavelength of 1730 nm. The initial spectral width of the pulse is 15.6 nm, and the pulse duration is 200 fs. In this analysis, the following function was used for the dispersion increasing behaviour, similar to [183]:

$$\beta_2(x) = \beta_{2L} - \Delta\beta_2 \left(\frac{L-x}{L} \right)^2, \quad (5.3)$$

where L represents the length of the fiber, x is the propagation point, β_2 is the value of dispersion at point x , β_{2L} represents the value of dispersion at point $x = L$ and $\Delta\beta_2$ corresponds to the variation of dispersion β_2 . At 1730 nm wavelength, the magnitude of β_{2L} was $-42 \text{ ps}^2/\text{km}$ and $\Delta\beta_2$ was $21 \text{ ps}^2/\text{km}$. In this way, the magnitude of the second-order dispersion in the fiber gradually increases from -42 to $-21 \text{ ps}^2/\text{km}$. The value of the third-order dispersion was $0.02 \text{ ps}^3/\text{km}$ and the MFD (mode field diameter) was $11 \text{ }\mu\text{m}$. The magnitude of the nonlinear coefficient was $3.5 \text{ W}^{-1}\text{km}^{-1}$ [182]. Figure 5.3 illustrates a variation of pulse parameters in the 500 m length of the dispersion-increasing fiber with linearly varied dispersion. The initial pulse was adjusted to reflect the experiment, therefore, the input pulse duration is 200 fs and the initial spectrum width is 15.6 nm.

The results of the output spectrum compared to the initial pulse are presented in Figure 5.3 (a). The input and output temporal shapes are gathered in Figure 5.3 (b). It is observed that the pulse gets compressed to the level of 0.6 nm. The temporal duration of the pulse after 500 m of the CPF is 5.5 ps. Figure 5.3 (c) demonstrates the variation of the second-order dispersion and pulse spectral width in the fiber. The magnitude of β_2 is almost linearly increased along the fiber length and the spectral width gradually decreases to the level below 1 nm. The variation of the soliton order, N , and the pulse's temporal width are shown in Figure 5.3 (d). The soliton order is increased in the first 50 m of the fiber to the magnitude of 5.5 and then decreases gradually to the level of 0.9. The temporal duration of the pulse is gradually increased with the fiber length.

The simulations performed for this case confirm that the non-constant fiber dispersion can lead to spectral compression of a pulse propagating inside such fiber. The compression factor is as high as 26 and the results are promising, however, in this case there are no fiber splices which would provide additional loss.

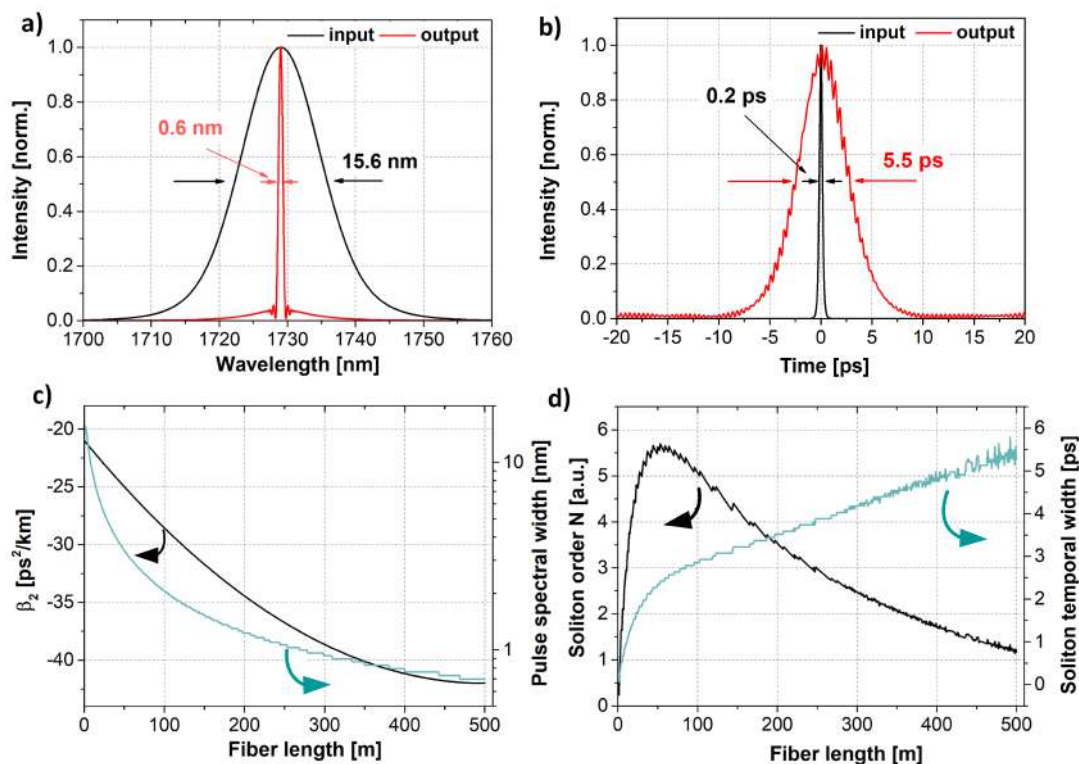


Figure 5.3: Variation of the pulse parameters inside the dispersion-increasing fiber: (a) input and output spectra of the pulse; (b) input and output pulse temporal profiles; (c) evolution of the pulse spectral width; (d) evolution of the soliton order and the pulse's temporal width.

5.3.2 Original comb-profile dispersion model

Since an optical fiber of dispersion profile presented in the previous Section does not exist, the dispersion-increasing fiber needs to be obtained in a different way. Based on other studies [183, 186], such a fiber can be combined of two types of fibers: SMF and DSF. Both these fibers are characterized by different second-order dispersion profiles. The value of β_2 for the SMF fiber at 1730 nm wavelength is $-42 \text{ ps}^2/\text{km}$ and for the DSF is $-21 \text{ ps}^2/\text{km}$ at the same wavelength. Both dispersion values are taken from dispersion measurements. By properly adjusting each segments' length of either SMF or DSF, one can achieve the required comb-profile of the average dispersion β_2 , which would ensure the spectral compression of the input pulses.

The general simulation model of the spectral compression technique provided by the CPF is demonstrated in Figure 5.4. The initial pulse with a relatively wide spectrum (10-20 nm) enters the CPF which consists of several segments of SMF and DSF spliced alternatively. A proper structure of the CPF should result in a narrow-linewidth output spectrum.

To obtain a desired results, several configurations of different CPF structures were tested. The simulations were performed with 4096 computational points. The initial time duration of the soliton was 200 fs and the pulse bandwidth was 15.6 nm. The nonlinear coefficient was equal to $3.5 (W \cdot \text{km})^{-1}$ and was constant along the fiber length. The MFD

values were equal 11 and 8.5 μm for the SMF and DSF fibers, respectively.

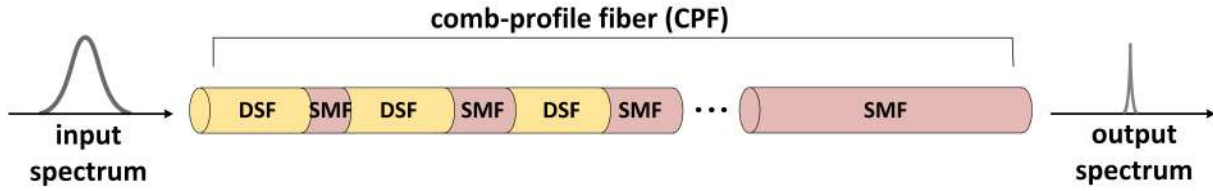


Figure 5.4: Schematic illustration of the simulation model for the pulse spectrum compression in the CPF.

Five examples of the CPF configuration are listed in Table 5.1. In each case, the simulation model starts with a segment of DSF which is spliced to an SMF, and so on. The results are demonstrated in Figure 5.5 and include the average and actual dispersion profile of the corresponding CPF model (left column) and output spectrum at the CPF end (right column). First configuration that was tested, assumes five segments of DSF and five segments of SMF, all of the same length: 10 m. The total length of the CPF is in this case 100 m. It is clear that such a configuration does not provide a comb-profile dispersion, however, there is still slight compression of the output spectrum: down to 11.5 nm. In the second approach, the DSF's segment lengths are decreasing, and SMF's are increasing, which significantly improves the results since the output pulse gets spectrally narrowed to 3.1 nm. In this scenario, the average dispersion reaches $-35.1 \text{ ps}^2/\text{km}$ after 102 m of propagation. Next configuration (3) maintains the same lengths of DSF segments while slightly increasing the middle segments of the SMF. The total length of the CPF, in this case, is 123 m and the average dispersion amounts to $-33.2 \text{ ps}^2/\text{km}$ at the fiber end. The output pulse is a little bit more compressed, the linewidth is 2.9 nm. In the next approach (4), the Author decided to increase all segments' lengths, especially the final segments of the SMF. This way, the total CPF length is 270 m and the average dispersion reaches $36.7 \text{ ps}^2/\text{km}$ at the CPF length. The linewidth of the output spectrum gets compressed to 1.9 nm.

Table 5.1: Five configurations of simulated CPF setup with varying lengths of SMF and DSF segments.

Configuration no.	Length of corresponding type of fiber: SMF or DSF													
	DSF	SMF	DSF	SMF	DSF	SMF	DSF	SMF	DSF	SMF	DSF	SMF	DSF	SMF
1	10	10	10	10	10	10	10	10	10	10				
2	10	1	8	1	6	5	4	15	2	50				
3	10	1	10	4	10	10	10	20	10	50				
4	20	1	18	5	10	25	6	75	10	100				
5	20	1	18	5	18	10	10	25	5	60	6	75	10	120

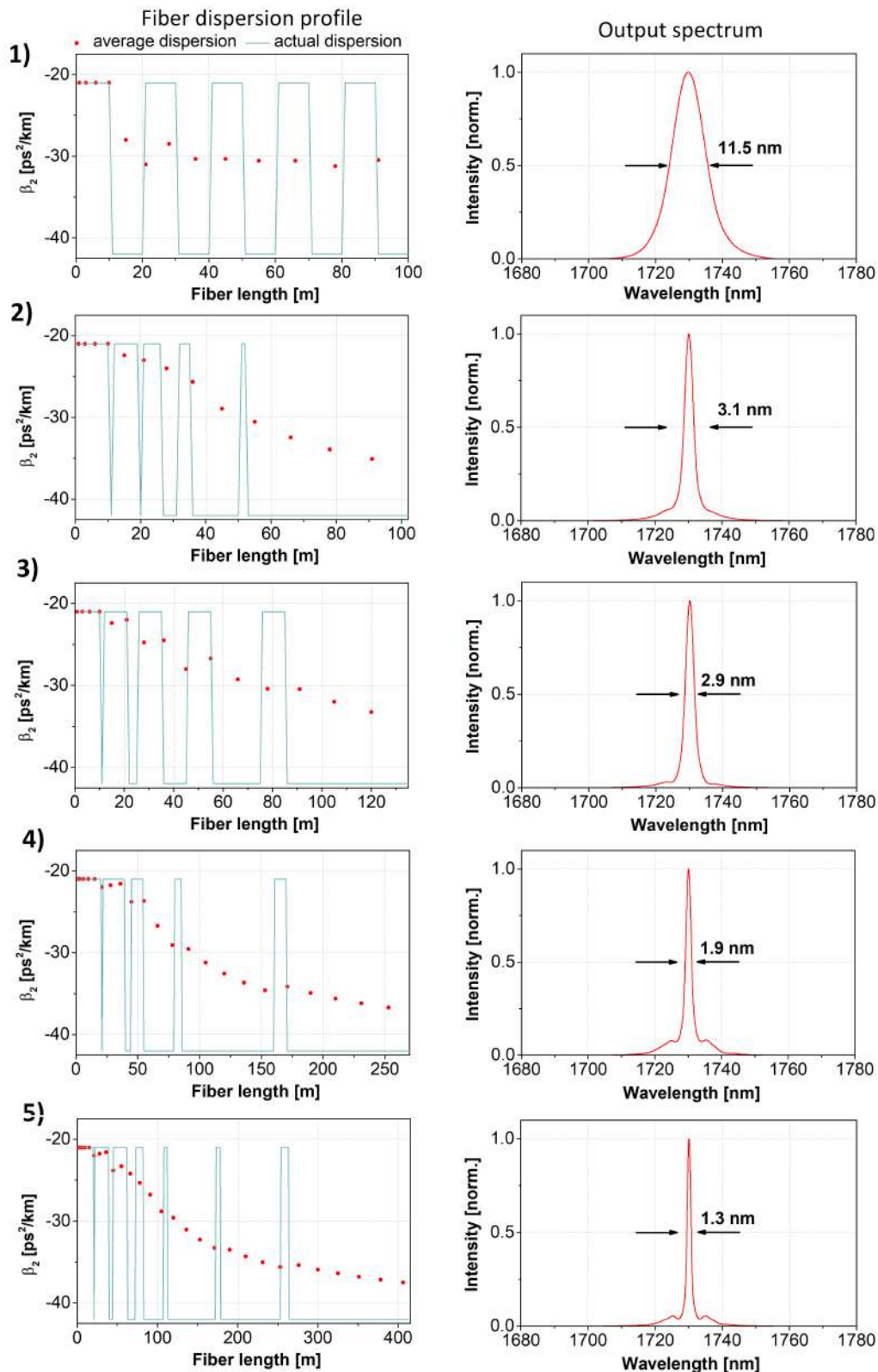


Figure 5.5: Simulation results for different configurations of SMF/DSF: actual and average dispersion profiles and output spectra of the compressed pulses.

Increasing the number of segments and the SMF lengths in the last configuration (5) results in achieving average dispersion of a magnitude of 37.5 ps²/km after 413 m of

propagation and narrowing the output pulse spectrum to 1.3 nm. Therefore, the results presented above indicate that both increasing the total length of the CPF and increasing the number of segments lead to spectral narrowing of the propagating pulse. Also, the final segments of the SMF should be much longer, so that the average dispersion could reach a value close to β_2 of SMF. As a result of numerous simulations with various configurations, the optimal CPF structure was found. The exact lengths of each DSF/SMF segment are gathered in Table 5.2.

Table 5.2: Lengths of each segment of dispersion-shifted fiber (DSF) spliced with single-mode fiber (SMF).

Fiber type	DSF	SMF																
Lengths [m]	20	1	18	3	20	8	22	25	3	60	2	60	10	70	10	180	10	300

The total length of the CPF was 822 m. The resulting dispersion profile of the CPF is presented in Figure 5.6. The lengths of the SMF segments increased along the fiber length, which resulted in the comb-profile shape of the average dispersion profile. Therefore, the average dispersion β_2 starts from the value of $-21 \text{ ps}^2/\text{km}$ and after 822 m of fiber length reaches the magnitude of $-38.95 \text{ ps}^2/\text{km}$.

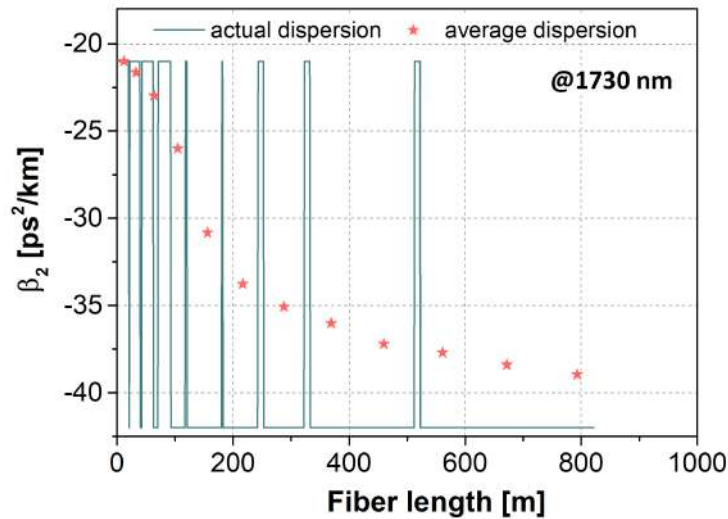


Figure 5.6: Actual and average dispersion profiles in the CPF.

The simulated propagation of the soliton pulse spectrum inside the CPF fiber is presented in Figure 5.7 a). The calculated soliton centred at 1730 nm was compressed inside the CPF from the initial 15.6 nm to the spectral width of 0.6 nm which corresponds to the compression factor of 26. Along with the propagation, the pulse acquires sidelobes that are, however, minimized in the end of the fiber length. Figure 5.7 (a) also directly indicates the exponential decrease in the spectral width compression, which effects gradually become more stagnant with the increase of the propagation length. The pulse temporal evolution

inside the CPF is presented in Figure 5.7 (b). As the pulse gets spectrally compressed, its temporal duration increases. After some distortions between 100 and 200 m, when the pulse's temporal shape loses its quality, it regains the smooth shape and gradually broadens to the fiber end.

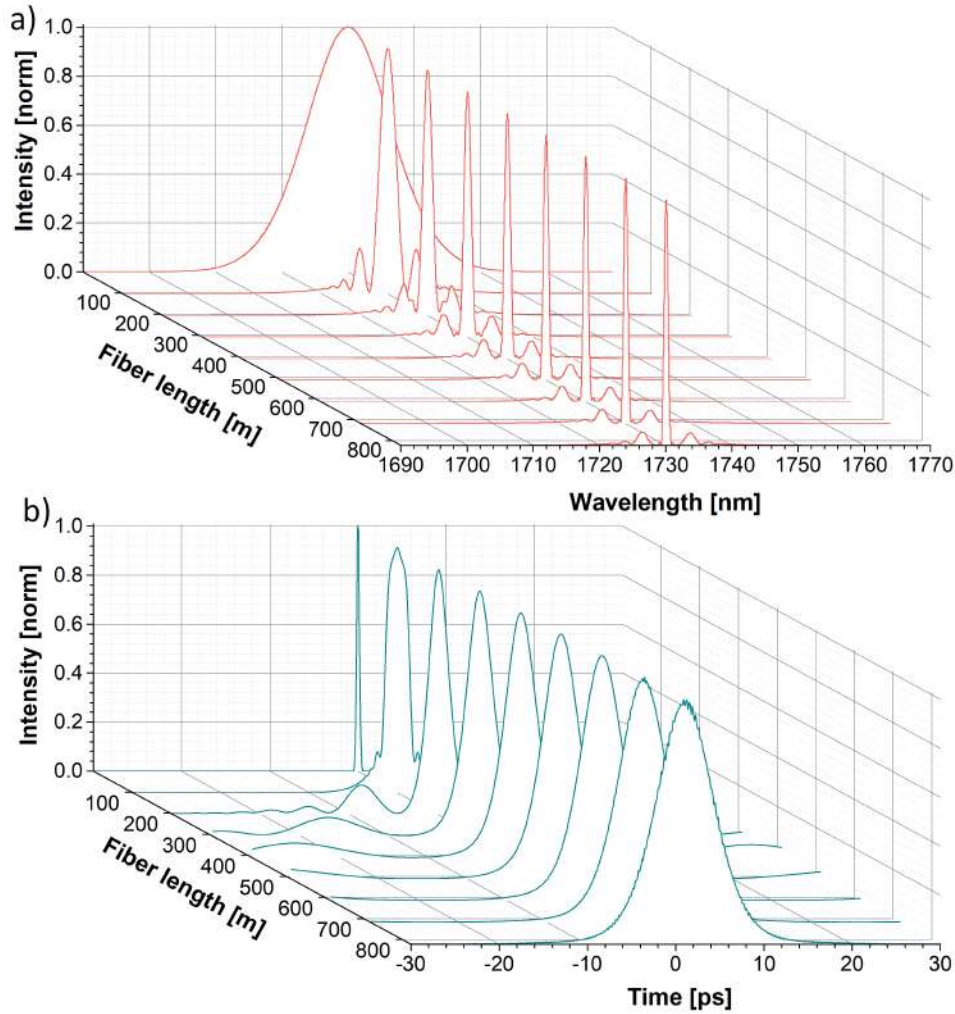


Figure 5.7: Evolution of the spectrum (a) and the temporal shape (b) of an optical soliton operating at 1730 nm propagating inside the CPF.

The comprehensive characteristics of the pulse propagation inside the CPF for the optical soliton operating at 1730 nm are demonstrated in Figure 5.8. The input and output spectra are presented in Figure 5.8 (a). The temporal profiles of the input and output pulse are depicted in Figure 5.8 (b). Figure 5.8 (c) shows the variation of the spectral width as a function of the fiber length. This picture illustrates the variation of the spectral width more completely compared to the previous example given by Figure 5.7. It can be noticed that apart from a small increase at around 100 m of propagation, the spectral width decreases gradually with the fiber length. In Figure 5.8 (d) the soliton order and the soliton temporal width are depicted as a function of the fiber length. The final magnitude of the soliton order reaches 0.95 and the temporal duration of the pulse after some perturbations is increased to the value of 7.52 ps. Both parameters exhibit

strong variations in the initial propagation of 150 m. This behaviour may indicate that the effects could be more optimized. These variations in both parameters: soliton order and pulse's temporal duration are more precisely depicted in Figure 5.8 (e) and (f), where the functions of these parameters as a fiber length are presented with the limit to the first 150 m of propagation.

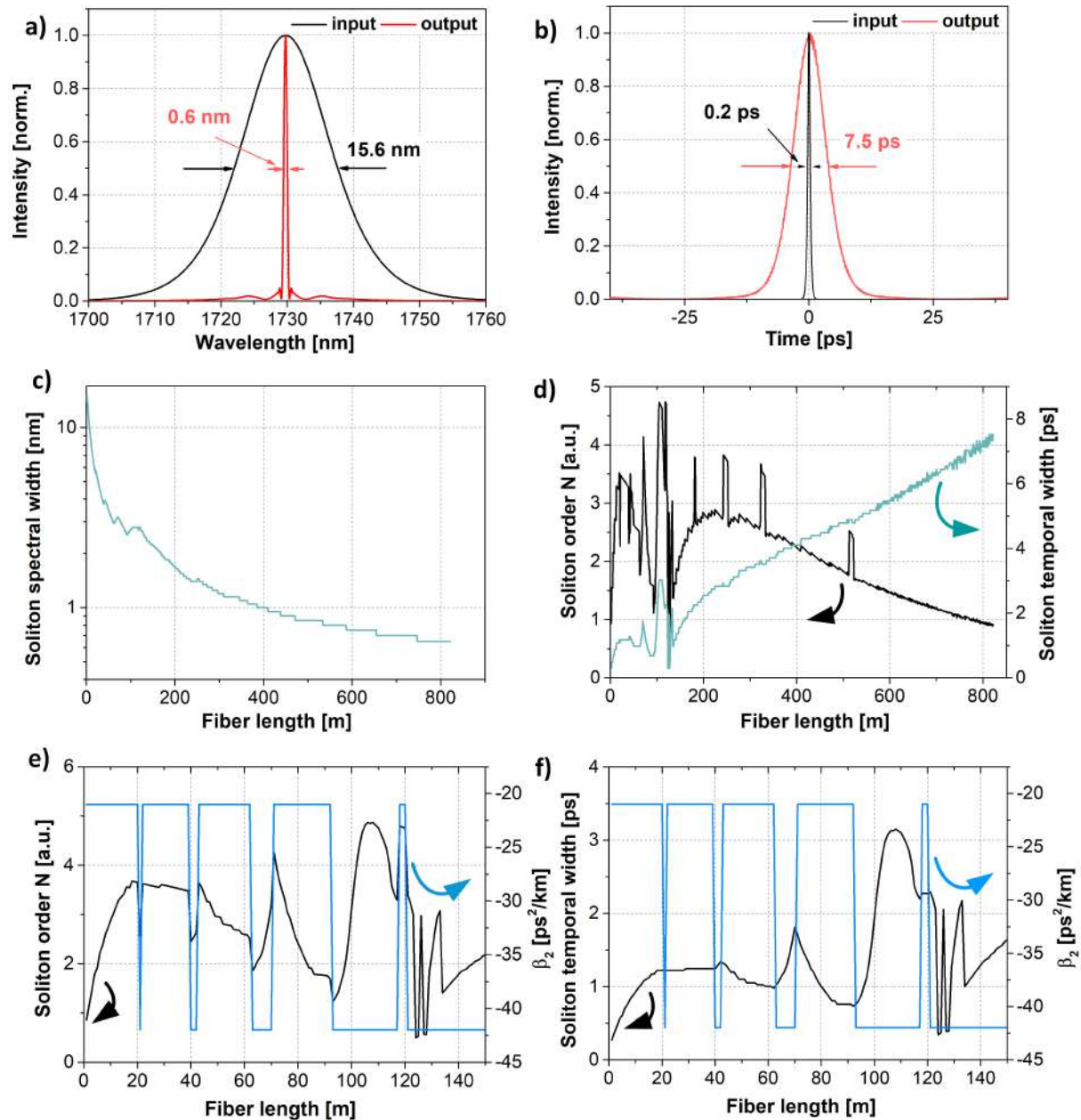


Figure 5.8: Variation of the pulse parameters inside the CPF; (a) input and output spectra of the pulse; (b) input and output pulse temporal profiles; (c) evolution of the pulse spectral width; (d) evolution of the soliton order, N , and the pulse's temporal width; (e) evolution of the N together with the actual dispersion profile β_2 for the 150 m of propagation; (f) evolution of the pulse's temporal width together with the actual dispersion profile β_2 for the 150 m of propagation.

It has already been mentioned that one of the effects that play the biggest role in this

phenomenon is SPM. And if so, the process should be crucially dependent on the pulse peak power. In Figure 5.9, the impact of the peak power on the pulse spectral width is being investigated. It can be observed how vital is a proper adjustment of the peak power on the efficiency of the process. With the increase of the peak power, the pulse gets spectrally narrowed until the magnitude of 170 W. When the value of the peak power is above the optimal, the pulse exhibits Raman gain and the quality of the spectrum become diminished.

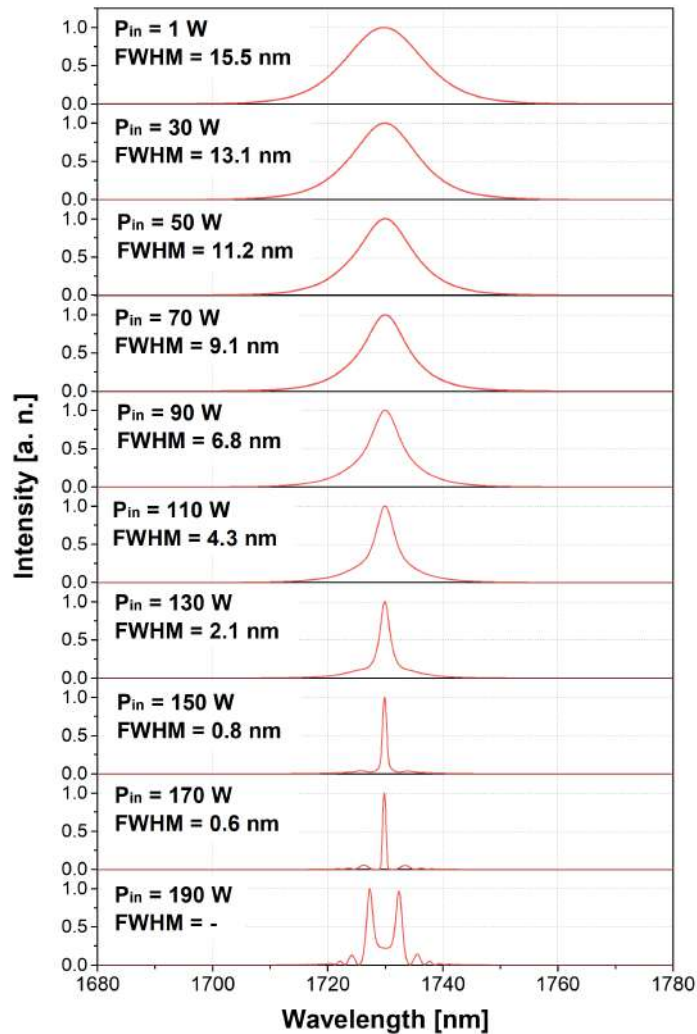


Figure 5.9: Simulation of the pulse spectrum for the values of the peak power varying from 1 W to 190 W.

5.4 Narrow linewidth laser source. Experimental results.

Based on the numerical results, the Author implemented the CPF in the experiment with the femtosecond laser source. The schematic illustration of the source is presented in

Figure 5.10. The entire setup was built in the all-fiber regime, therefore, no bulk optics was used. All splices were done with the use of a standard arc fusion splicer (Fujikura FSM 100P+). The ultrashort pulses are generated in an Erbium-doped oscillator that emits 300 fs pulses of 7 mW average optical power at a 50 MHz repetition rate. The oscillator was built in our lab and it employs the SESAM saturable absorber to obtain the mode-locking regime.

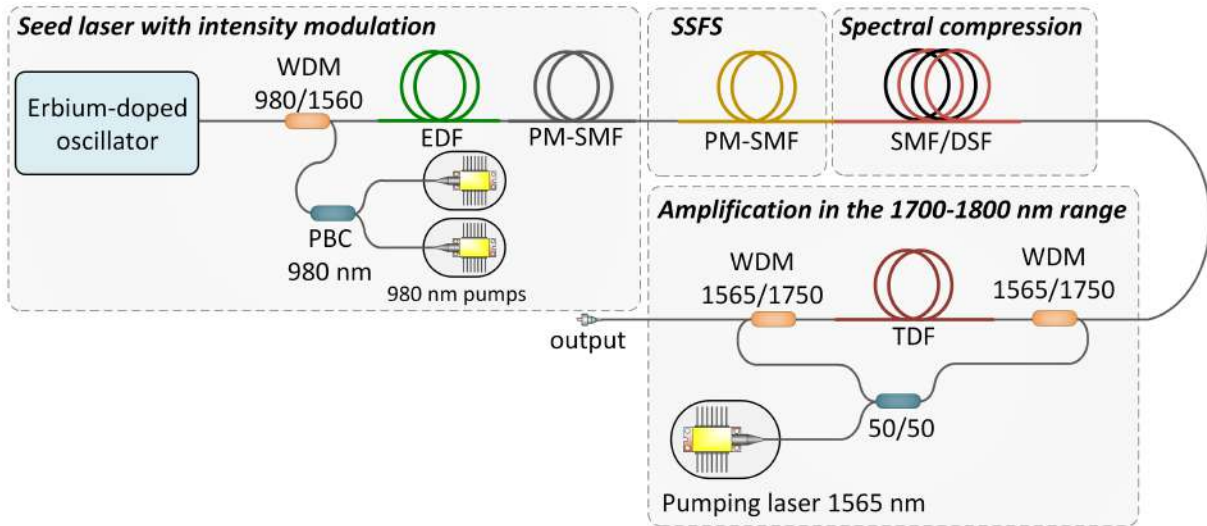


Figure 5.10: The schematic of the experimental setup for the investigation of the spectral compression effect. WDM: wavelength division multiplexer; EDF: Erbium-doped fiber; PBC: polarization beam combiner; HNLF: highly-nonlinear fiber; SMF: single-mode fiber; DSF: dispersion-shifted fiber; TDF: Thulium-doped fiber.

The ultrashort laser pulses from the oscillator are then amplified in an Erbium-doped fiber amplifier which was built in the CPA technique. In such a fiber amplifier, pulses are first stretched temporally in a normal-dispersion fiber, then they are amplified and eventually compressed in a fiber with anomalous dispersion. The normal dispersion fiber was a 130 cm-long Erbium-doped fiber (EDF, nLight Liekki Er80-4/125-PM-HD) which was pumped with two 1 W 980 nm pumps provided via polarization beam combiner (PBC). The last part of the seed laser was a 77 cm-long PM standard single-mode fiber (Coherent PM-1550 XP) which, due to its anomalous dispersion profile, served as a pulse compressor. The laser pulses were compressed to the duration of 42 fs and reached 249 mW average optical power which corresponded to 121 kW of peak power and 5.8 nJ energy. The autocorrelation of the laser pulse together with the sech²-shaped fit is presented in Figure 5.11 (a). The optical spectrum is depicted in Figure 5.11 (b), indicating that the output pulses from the laser source possessed a spectrum of 131 nm bandwidth.

The amplified pulses were later provided to a 44 m of PM-SMF which allowed for SSFS in the range of up to 1920 nm. The spectral widths of the solitons were in the range of 14.9–16.2 nm wavelength. The spectra of the tunable solitons are presented in Figure 5.12 (a). The modulations in the spectra that can be observable for solitons between 1.80–1.95 μm are related to water absorption. The power levels stored in the solitons were measured

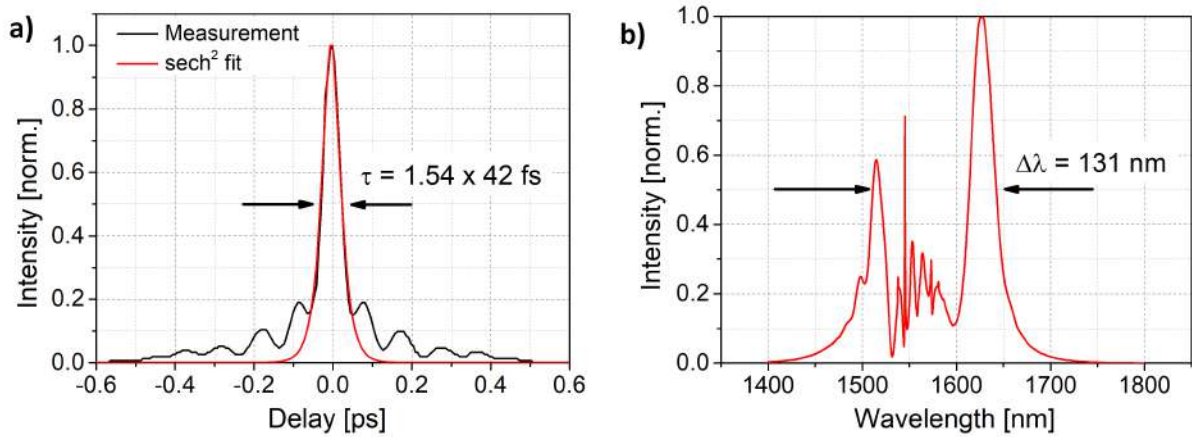


Figure 5.11: The autocorrelation (a) and the optical spectrum (b) of the laser pulse.

with the thermal power meter (Thorlabs PM400) and the bandpass filter with a 1750-2250 nm transmission band (Thorlabs FB2000). The power levels measured after the filter were in the range of 20.5-40.3 mW for the solitons in the wavelength range 1790-1920 nm. The tunable pulses were then directly provided to the CPF which was adapted according to the numerical model presented in Section 5.3. The total length of the CPF was 822 m, and its average dispersion profile resembles the profile of the numerically designed fiber. The CPF allowed for spectral compression of the pulses in the wavelength range of 1622 to 1900 nm. The spectral widths levels were 0.43-1.11 nm and the corresponding compression factor was in the range of 37.2-13.5. The compression factor of 37.2 is the highest obtained result for this wavelength range (compared to 25.6 in [190]). The spectra of the compressed solitons are depicted in Figure 5.12 (b).

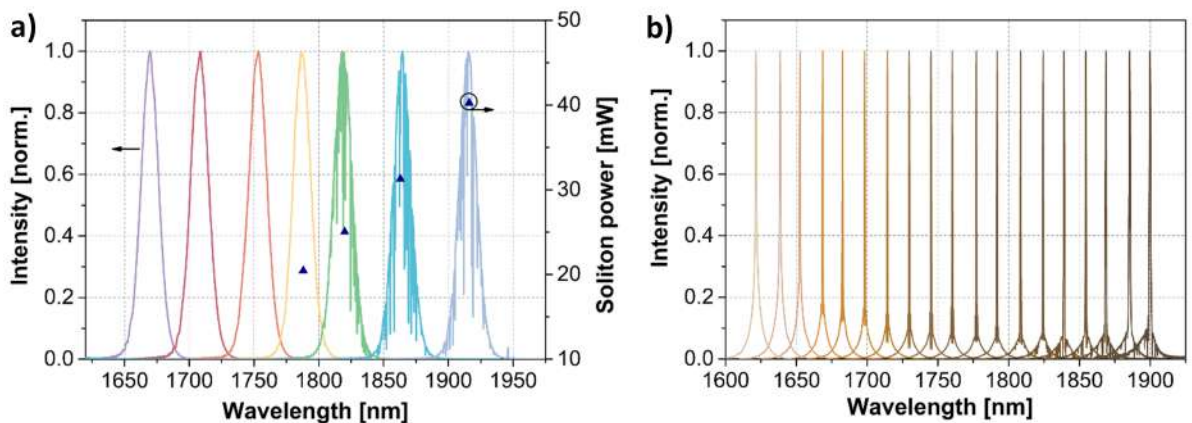


Figure 5.12: Optical spectra of the tunable solitons generated in PM-SMF with the optical powers stored in the solitons (a); optical spectra after spectral compression in the CPF (b).

Due to the fact that the spectral compression effect is a result of both dispersion and SPM, it is mainly dependent on the peak power of the pulse. If the peak power is too high it would result in the Raman gain and the pulse spectrum would be destroyed. Pulse

power management has usually been done by providing a variable attenuator together with a low-pass filter [183, 186]. However, to maintain the system in the all-fiber regime we proposed an attenuated splice that decreased the power of the broad solitons. The splice loss was adjusted and reached 3 dB. It enabled for effective spectral compression in the CPF.

The design of the CPF was based on the numerical model, therefore to compare the experimental and simulated results, three compressed pulses at wavelengths: 1682, 1730 and 1839 nm have been compared and presented in Figure 5.13. The results show excellent agreement of the simulations and the experiments. It is observed that for the solitons 1682 and 1730 nm, the experimental spectra feature a slightly higher pedestal than the modelled CPF.

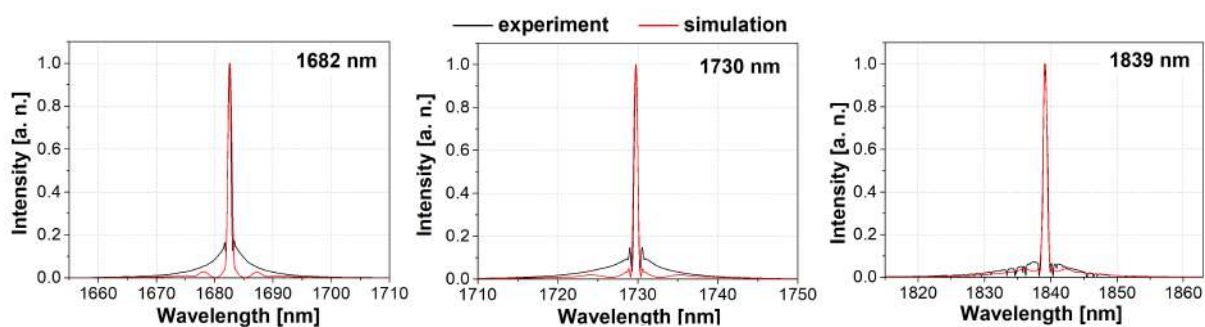


Figure 5.13: The simulated and experimental spectra for three different soliton wavelengths: 1682 nm, 1730 nm and 1839 nm.

5.4.1 Short-wavelength Tm-doped fiber amplifier.

Sweep-sources for OCT are often limited when it comes to optical power levels. Biomedical applications usually do not require high-power lasers, however, the laser setups for the actual biomedical measurements (e.g. OCT) utilize components such as optical couplers, filters, beam splitters, and many others that would reduce the actual output power of the laser system. Therefore, it would be reasonable to initially amplify the output pulses. The wavelength range of the swept-source presented in the previous section lays within a spectral range covered by the Thulium-doped fibers, however, it is on the edge of it. A short wavelength operation of Tm-doped amplifiers has already been reported [191–193].

The compressed pulses were eventually amplified in the Tm-doped fiber amplifier pumped by a 1565 nm pumping laser. The pump power was provided by two wavelength-division multiplexers (WDM), adjusted for 1750 nm wavelength, to the 1 m of Thulium-doped fiber (TDF, OFS TmDF200). The utilization of these two WDMs together with implementing a short segment of TDF allows for amplification of the signal at such short wavelength range. The spectra of the compressed pulses before and after the amplification stage are presented in Figure 5.14 (a). A small mismatch in the central wavelength is observed for solitons above and below ≈ 1800 nm. This effect is a result of a gain-pulling towards the center of the emission gain bandwidth of the Tm-doped fiber amplifier, for

which the gain peak is near 1770 nm. The maximum average optical powers obtained for different solitons are depicted in Figure 5.14 (b). The source reached maximum average power of 446 mW at a 1770 nm wavelength. With the use of WDMs adjusted for a 1750 nm wavelength it was possible to amplify such short wavelength signal in the Tm-doped fiber amplifier. Comparing our design to the similar systems in the literature we can notice the simplicity of our approach. Other proposals include either inducing a segment of Holmium-doped fiber or custom-made fiber components that are not commercially available.

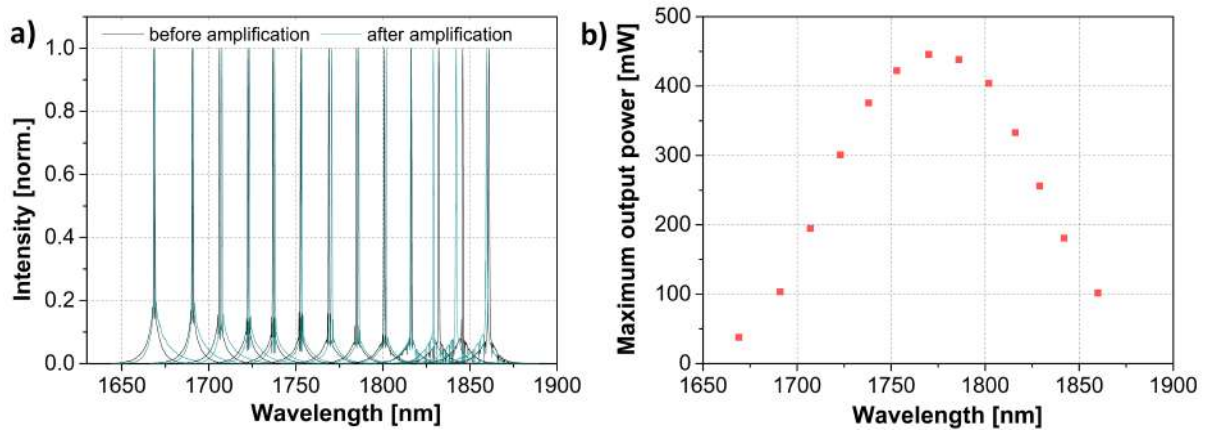


Figure 5.14: Spectra of the compressed solitons before and after amplification (a); maximum output power levels achieved for amplification of the compressed solitons for the wavelength range of 1669-1860 nm

5.5 Conclusions

In this Chapter, a narrow-linewidth laser source has been presented and characterized. A comprehensive numerical analysis of the spectral compression phenomenon in an optical fiber with dispersion varying along the length has been performed. Then, the experiment that was conducted by implementing numerically designed comb-profile fiber has been described and the experimental results have been discussed. The laser system provided optical pulses tunable in the wavelength range of 1622-1900 nm compressed to the level of 0.43-1.11 nm. The maximal compression factor was 37.2 which is the highest achieved result within this tuning range. The compressed pulses were then provided to the Tm-doped fiber amplifier adjusted for the short wavelength range. The amplified pulses achieved maximal optical power of 446 mW. The laser source was entirely all-fiber, with narrow linewidth and sufficient power to be used as a swept-source for applications such as OCT. The results of this experiment have been published by the Author in [175].

Chapter 6

Conclusions

The subject of this dissertation was a study of nonlinear effects that lead to spectral conversion in nonlinear silica fibers. The thesis was that the optical solitons generated through SSFS effect in microstructured silica fibers with anomalous dispersion regime possess as good noise properties as the supercontinuum generated in a microstructured fiber with a normal dispersion profile, and that the SSFS effect can lead to a generation of narrow-linewidth frequency-shifted solitons. The dissertation consists of 6 Chapters, among which one contains theoretical information and simulations, and three of them describe the experimental work.

Chapter 2 provides theoretical information on pulse propagation inside an optical fiber. The dispersion and nonlinear effects that play the most important role in affecting the pulse inside the optical fiber were discussed. The formation of optical solitons was described. The Author presented a full characterization of the microstructured fibers, including their design and properties. The simulation of the SSFS effect and supercontinuum in a MOF was presented. Also, the description of the numerical method used for pulse propagation modelling was given. Lastly, a few methods that are used for characterizing pulse properties were given and discussed.

In Chapter 3 results of SSFS effect generated in a microstructured silica fiber for two pumping sources are presented. In the experiment, two laser sources are used: Ytterbium-doped fiber laser operating at $1.06 \mu\text{m}$ and Erbium-doped fiber laser that emitted pulses at $1.56 \mu\text{m}$. The full characterization of the frequency-shifted solitons is demonstrated. The optical solitons generated in the MOF are widely tunable and of a high degree of coherence and birefringence.

Chapter 4 describes the study of two nonlinear effects SSFS and ANDi-SC used as seedings for Tm-doped fiber amplifier. The study concentrates on the noise dynamics inside the nonlinear fibers possessing opposite signs of dispersion. The comprehensive analysis, that was performed, includes coherence measurement, dispersive Fourier transform, and intensity noise, and the results are discussed. Eventually, the Tm-doped fiber amplifier is presented, seeded by both nonlinear effects and the outcome pulses are compared for both configurations in terms of relative intensity noise, spectral and temporal phase. The amplified pulses are of 80 fs duration and 405 mW average maximal optical power for

SSFS seeding and 92 fs and 350 mW average optical power for ANDi-SC seeding.

Chapter 5 provides insight to the spectral compression phenomenon that can occur in an optical fiber with varying dispersion profile. A numerical analysis of the subject is performed, including the case, where the fiber possesses a linearly-varying dispersion, and the simulation of the original comb-profile fiber that is later used in the experiment. The laser setup generating spectrally-compressed optical solitons with the tuning possibility in the 1622-1900 nm wavelength range is demonstrated. The optical solitons are compressed from the initial 14.9–16.2 nm to the linewidths of 0.43–1.11 nm. The additional amplification stage is added to obtain output pulses at power levels sufficient for later applications. The Thulium-doped fiber amplifier is adjusted for 1750 nm so that within the short-wavelength range it was possible to amplify the spectrally-compressed pulses up to 400 mW.

All the thesis goals have been accomplished. The results presented in Chapter 4 confirm the thesis that optical solitons generated in an anomalous dispersion regime can exhibit low-noise properties which are comparable or even of higher quality than the supercontinuum produced in the normal dispersion fiber. Additionally, Chapter 5 demonstrates that optical solitons can be used for the generation of narrow-linewidth pulses. By implementing a dispersion-varying fiber the optical solitons can be successfully spectrally compressed to the level < 1 nm.

The most important research achievements are summarized below:

- Comparative study on the nonlinear effects in air-silica microstructured fibers: SSFS and ANDi-SC in terms of noise properties including: coherence, shot-to-shot stability, spectral and temporal phase analysis, and intensity noise.
- An assembly of the Tm-doped fiber amplifier seeded by SSFS and ANDi-SC.
- Realization of a numerical model of the spectral compression effect in a fiber with comb-like dispersion profile.
- Realization of the narrow-linewidth laser source tunable in the wavelength range of 1620-1900 nm
- An assembly of the Tm-doped fiber amplifier adjusted for short wavelength operation (1650-1900 nm)

The Author currently continues the study on the spectral compression phenomenon that was demonstrated in this dissertation. The research concentrates on adjusting the narrow-linewidth source for OCT measurements by adding the electro-optical modulator to the setup and the analysis of the rapidly swept narrow line with the use of a Fourier transform spectrometer. The Author also plans to conduct research on the spectral conversion process in fluoride fibers when pumped with a 2 μ m pumping laser.

Streszczenie

Konwersja spektralna, która występuje w światłowodach nieliniowych przy zapompowaniu ich laserowym źródłem impulsowym, to technika pozwalająca na generację promieniowania poza dostępnymi ośrodkami wzmacniającymi (takimi jak Irb, Erb, Tul i Holm). Efekty nieliniowe, jakie wtedy występują, w połączeniu z laserami erbowymi lub iterbowymi, mogą zostać wykorzystane do budowy źródeł pracujących w zakresach spektralnych 1300 nm lub 1700 nm, które są w szczególnym zainteresowaniu obrazowania biomedycznego.

Praca rozpoczyna się od wprowadzenia teoretycznego. Zaprezentowane zostały efekty nieliniowe występujące w światłowodach, które mają wpływ na propagujący impuls laserowy. Opisano efekty dyspersji oraz nieliniowości, które mogą wystąpić dla dużych natężeń wprowadzanych impulsów. Została przedstawiona i opisana struktura włókna mikrostrukturalnego oraz symulacje efektów nieliniowych, takich jak samo-przesunięcie częstotliwości solitonu (SSFS) i superkontinuum w tego rodzaju włóknie. Część teoretyczną zamyka opis technik służących charakteryzacji krótkich impulsów laserowych, takich jak dyspersyjna transformata Fouriera, pomiar koherencji, pomiar metodą FROG oraz analiza szumów amplitudowych.

W ramach pracy badawczej zostały opracowane liczne symulacje numeryczne celem dostosowania parametrów impulsu jak i włókna, i dzięki temu uzyskać generację promieniowania w wybranym zakresie spektralnym. Trzy rozdziały pracy zostały poświęcone układom eksperymentalnym, które zostały zaprezentowane i omówione. W pierwszym kroku została przedstawiona analiza efektu SSFS we włóknie mikrostrukturalnym przy zapompowaniu laserami pracującymi na różnych długościach fali: erbowym oraz iterbowym. W efekcie uzyskano generację przestrajalnych solitonów w zakresie długości fali 1,42-1,67 μm dla lasera iterbowego oraz w zakresie 1,70-1,95 μm dla lasera erbowego. Wygenerowane solitony charakteryzowały się wysoką koherencją oraz dwójłomnością, co sprawia, że mogą być wykorzystane w aplikacjach takich jak optyczna tomografia koherencyjna oraz jako źródła do tulowych lub holmowych wzmacniaczy światłowodowych.

Następny rozdział dotyczył analizy porównawczej efektów nieliniowych: SSFS oraz superkontinuum wygenerowanych w światłowodach mikrostrukturalnych o różnym reżimie dyspersji. Została przeprowadzona pełna charakteryzacja impulsów wychodzących z obu światłowodów, zawierająca pomiar widm optycznych, koherencji, stabilności impulsów oraz szumów amplitudowych. Otrzymane wyniki wskazują, że impulsy z obu efektów nieliniowych cechują się bardzo dobrymi parametrami nisko-szumnymi, jak i wysoką

stabilnością oraz mogą służyć jako źródła do tulowych wzmacniaczy światłowodowych.

Kolejnym eksperymentem opisanym w pracy był efekt kompresji spektralnej we włóknie o zmiennej dyspersji. Omówiono podstawy teoretyczne techniki kompresji spektralnej oraz zaprezentowano model numeryczny opracowany na potrzeby układu. Dzięki symulacjom możliwe było wyznaczenie optymalnej konstrukcji włókna o zmiennej dyspersji, które później zostało wykorzystane w układzie eksperymentalnym przestrajalnych wąskopasmowych solitonów. Uzyskano solitony optyczne przestrajalne w zakresie długości fali 1620-1900 nm o szerokościach linii w zakresie 0,43-1,11 nm. Tak zawężone spektralnie solitony zostały następnie wzmocnione w tulowym wzmacniaczu światłowodowym, dostosowanym do tego zakresu długości fali, w celu otrzymania mocy impulsów potrzebnych do późniejszych zastosowań.

Ostatni rozdział zawiera podsumowanie omówionych prac badawczych. Zostały wymienione autorskie osiągnięcia oraz zaprezentowane dalsze plany naukowe.

Abstract

Spectral conversion, that can be obtained in nonlinear fibers when pumped with femtosecond laser sources, is a powerful technique which allows for generation of non-standard wavelengths outside the available gain media, including Ytterbium, Erbium, Thulium and Holmium. These nonlinear effects, when combined with Yb- or Er-doped fiber lasers, can be used either as sources operating in the spectral range of 1300 or 1700 nm which is of particular interest of biomedical imaging, or as seedings for Tm- or Ho-doped fiber amplifiers, as an alternative to Tm- or Ho-doped fiber lasers.

The Dissertation begins with the theoretical analysis of different phenomena affecting an ultrashort pulse propagating in an optical fiber. The impact of dispersion as well as various nonlinear effects, that can occur for high intensities of the light confined in an optical fiber, is discussed. The concept of microstructured silica fiber is analyzed and the simulation examples of soliton self-frequency shift effect (SSFS) and supercontinuum in such a fiber are given. The theoretical part of the thesis ends with the description of different methods that are used for characterization of the short pulse, such as dispersive Fourier transform, pulse-to-pulse coherence, FROG measurement, and intensity noise.

For the purpose of the doctoral thesis, numerous simulations have been performed to model and adjust both the pulse and the fiber parameters to obtain required spectral range. Three chapters of the thesis are devoted to experimental setups that have been demonstrated and discussed. First, the analysis of the SSFS generated in a microstructured optical fiber for two pumping sources: EDFL and YDFL is presented. Generation of the SSFS in the range of 1.42-1.67 μm for YDFL pumping and 1.70-1.95 μm for EDFL pumping has been obtained. The frequency-shifted solitons are highly coherent and birefringent which makes them suitable to be used in applications such as optical coherence tomography and as seedings for Tm-doped fiber amplifiers.

The next experiment concentrates on the comparative study of the SSFS and ANDi-SC effects generated in microstructured optical fibers with opposite dispersion profiles. The characterization of both phenomena are presented, including measurements of optical spectra, coherence, shot-to-shot stability, and intensity noise. The results reveal that both nonlinear effects, despite being generated in fibers with different signs of dispersion, can feature excellent noise properties. What is more, both effects can successfully be used as seedings for Tm-doped fiber amplifiers.

The next Chapter covers the analysis of the spectral compression phenomenon in a dispersion-increasing fiber. The theory of the spectral compression effect is given and

the numerical simulations are performed leading to finding the optimal structure of the dispersion-increasing fiber. Such a fiber is used to build a narrow-linewidth laser source that provides widely tunable optical solitons in the wavelength range of 1620-1900 nm with linewidths between 0.43-1.11 nm. The spectrally-compressed solitons are eventually amplified in a Tm-doped fiber amplifier optimized for this wavelength range to obtain power levels satisfactory for later applications as a swept-source.

The last Chapter contains summary of the performed experimental results. A list of most important research achievements is provided and the outlook for future plans is given.

Bibliography

- [1] F. P. Kapron, D. B. Keck, and R. D. Maurer. “Radiation losses in glass optical waveguides.” In: *Applied Physics Letters* 17.10 (1970), pp. 423–425.
- [2] T. Miya, Y. Terunuma, T. Hosaka, and T. Miyashita. “Ultimate low-loss single-mode fibre at 1.55 μm .” In: *Electronics Letters* 15.4 (1979), pp. 106–108.
- [3] R. Ramaswami, K. Sivarajan, and G. Sasaki. *Optical Networks: A Practical Perspective, 3rd Edition*. 3rd edition. 2009. 928 pp.
- [4] G. Keiser. *Optical Fiber Communications*. 4th edition. 2010. 688 pp.
- [5] R. Stolen. “The Early Years of Fiber Nonlinear Optics.” In: *Journal of Lightwave Technology* 26.9 (2008), pp. 1021–1031.
- [6] G. P. Agrawal. *Nonlinear Fiber Optics - 5th Edition*. 2013.
- [7] R. H. Stolen, E. P. Ippen, and A. R. Tynes. “Raman Oscillation in Glass Optical Waveguide.” In: *Applied Physics Letters* 20.2 (1972), pp. 62–64.
- [8] E. Ippen and R. Stolen. “Stimulated Brillouin scattering in optical fibers.” In: *Applied Physics Letters* 21.11 (1972), pp. 539–541.
- [9] R. Stolen and A. Ashkin. “Optical Kerr effect in glass waveguide.” In: *Applied Physics Letters* 22.6 (1973), pp. 294–296.
- [10] R. H. Stolen, J. E. Bjorkholm, and A. Ashkin. “Phase-matched three-wave mixing in silica fiber optical waveguides.” In: *Applied Physics Letters* 24 (1974), p. 308.
- [11] R. Stolen. “Phase-matched-stimulated four-photon mixing in silica-fiber waveguides.” In: *IEEE Journal of Quantum Electronics* 11.3 (1975), pp. 100–103.
- [12] R. H. Stolen and C. Lin. “Self-phase-modulation in silica optical fibers.” In: *Physical Review A* 17.4 (1978), pp. 1448–1453.
- [13] A. Hasegawa and F. Tappert. “Transmission of stationary nonlinear optical pulses in dispersive dielectric fibers. I. Anomalous dispersion.” In: *Applied Physics Letters* 23.3 (1973), pp. 142–144.
- [14] L. F. Mollenauer, R. H. Stolen, and J. P. Gordon. “Experimental Observation of Picosecond Pulse Narrowing and Solitons in Optical Fibers.” In: *Physical Review Letters* 45.13 (1980), pp. 1095–1098.
- [15] R. Boyd. *Nonlinear Optics - 3rd Edition*. 2008.
- [16] G. P. Agrawal. “Nonlinear fiber optics: its history and recent progress [Invited].” In: *JOSA B* 28.12 (2011), A1–A10.

-
- [17] K. S. Thyagarajan and A. Ghatak. *Fiber Optic Essentials*. 2007.
- [18] E. P. Ippen, S. Jacobs, M. Sargent III, J. F. Scott, and M. O. Scully. “Chapt. 6.” In: *Laser applications to optics and spectroscopy*. Vol. 2. 1975.
- [19] P. Diament. *Wave transmission and fiber optics*. 1990.
- [20] M. F. S. Ferreira. *Nonlinear Effects in Optical Fibers*. 2011.
- [21] T. Li. *Optical Fiber Communications: Fiber Fabrication*. 1985.
- [22] D. Marcuse. *Light Transmission Optics*. 1989. 534 pp.
- [23] G. P. Agrawal and M. J. Potasek. “Nonlinear pulse distortion in single-mode optical fibers at the zero-dispersion wavelength.” In: *Physical Review A* 33.3 (1986), pp. 1765–1776.
- [24] M. A. Ablowitz and P. A. Clarkson. *Solitons, Nonlinear Evolution Equations and Inverse Scattering*. 1991.
- [25] C. Sulem and P. Sulem. *The Nonlinear Schrödinger Equation: Self-Focusing and Wave Collapse*. 1999.
- [26] Y. Kivshar and G. Agrawal. *Optical Solitons: From Fibers to Photonic Crystals*. 2003. 557 pp.
- [27] L. F. Mollenauer and J. Gordon. *Solitons in Optical Fibers - Fundamentals and Applications*. 2006.
- [28] N. Bloembergen. *Nonlinear Optics*. 1996. 172 pp.
- [29] Y. R. Shen. *The Principles of Nonlinear Optics*. 1984.
- [30] G. P. Agrawal. In: *Properties, Processing, and Applications of Glass and Rare Earth-Doped Glasses for Optical Fibres*. 1998, pp. 17–22.
- [31] H. A. Haus and W. S. Wong. “Solitons in optical communications.” In: *Reviews of Modern Physics* 68.2 (1996), pp. 423–444.
- [32] R. Gangwar, S. P. Singh, and N. Singh. “Soliton Based Optical Communication.” In: *Progress In Electromagnetics Research* 74 (2007), pp. 157–166.
- [33] M. E. Fermann, A. Galvanauskas, and G. Sucha. *Ultrafast Lasers: Technology and Applications*.
- [34] E. Picholle, C. Montes, C. Leycuras, O. Legrand, and J. Botineau. “Observation of dissipative superluminous solitons in a Brillouin fiber ring laser.” In: *Physical Review Letters* 66.11 (1991), pp. 1454–1457.
- [35] P. Grellu and N. Akhmediev. “Dissipative solitons for mode-locked lasers.” In: *Nature Photonics* 6.2 (2012), pp. 84–92.
- [36] J. M. Soto-Crespo, N. N. Akhmediev, V. V. Afanasjev, and S. Wabnitz. “Pulse solutions of the cubic-quintic complex Ginzburg-Landau equation in the case of normal dispersion.” In: *Physical Review E* 55.4 (1997), pp. 4783–4796.
- [37] P. Grellu and J.M. Soto-Crespo. “Temporal Soliton “Molecules” in Mode-Locked Lasers: Collisions, Pulsations, and Vibrations.” In: *Dissipative Solitons: From Optics to Biology and Medicine*. 2008, pp. 1–37.

- [38] P. K. Shukla and J. Juul Rasmussen. “Modulational instability of short pulses in long optical fibers.” In: *Optics Letters* 11.3 (1986), pp. 171–173.
- [39] R. Paschota. *Encyclopedia of Laser Physics and Technology*. 2008.
- [40] C. V. Raman. “A new radiation.” In: *Proceedings of the Indian Academy of Sciences - Section A* 37.3 (1928), pp. 333–341.
- [41] E. J. Woodbury and W. K. Ng. “First demonstration of stimulated Raman scattering.” In: *Light Scattering in Solids* 50.2347 (1962), pp. 275–328.
- [42] M. D. Duncan, J. Reintjes, and T. J. Manuccia. “Scanning coherent anti-Stokes Raman microscope.” In: *Optics Letters* 7.8 (1982), pp. 350–352.
- [43] B. von Vacano, L. Meyer, and M. Motzkus. “Rapid polymer blend imaging with quantitative broadband multiplex CARS microscopy.” In: *Journal of Raman Spectroscopy* 38.7 (2007), pp. 916–926.
- [44] T. B. Huff and J. X. Cheng. “In vivo coherent anti-Stokes Raman scattering imaging of sciatic nerve tissue.” In: *Journal of microscopy* 225 (Pt 2 2007), pp. 175–182.
- [45] M. Okuno, H. Kano, P. Leproux, V. Couderc, J. P. R. Day, M. Bonn, and H. Hamaguchi. “Quantitative CARS Molecular Fingerprinting of Single Living Cells with the Use of the Maximum Entropy Method.” In: *Angewandte Chemie International Edition* 49.38 (2010), pp. 6773–6777.
- [46] Q. Lin and Govind P. Agrawal. “Raman response function for silica fibers.” In: *Optics Letters* 31.21 (2006), pp. 3086–3088.
- [47] R. Shuker and R. W. Gammon. “Raman-Scattering Selection-Rule Breaking and the Density of States in Amorphous Materials.” In: *Physical Review Letters* 25.4 (1970), pp. 222–225.
- [48] E. M. Dianov, A. Ya. Karasik, P. V. Mamyshev, A. M. Prokhorov, V. N. Serkin, M. F. Stel’Makh, and A. A. Fomichev. “Stimulated-Raman conversion of multisoliton pulses in quartz optical fibers.” In: *Soviet Journal of Experimental and Theoretical Physics Letters* 41 (1985), pp. 294–297.
- [49] F. M. Mitschke and L. F. Mollenauer. “Discovery of the soliton self-frequency shift.” In: *Optics Letters* 11.10 (1986), pp. 659–661.
- [50] P. Beaud, W. Hodel, B. Zysset, and H. Weber. “Ultrashort pulse propagation, pulse breakup, and fundamental soliton formation in a single-mode optical fiber.” In: *IEEE Journal of Quantum Electronics* 23.11 (1987), pp. 1938–1946.
- [51] N. Nishizawa and T. Goto. “Widely wavelength-tunable ultrashort pulse generation using polarization maintaining optical fibers.” In: *IEEE Journal of Selected Topics in Quantum Electronics* 7.4 (2001), pp. 518–524.
- [52] S. Kivisto, T. Hakulinen, M. Guina, and O. G. Okhotnikov. “Tunable Raman Soliton Source Using Mode-Locked Tm–Ho Fiber Laser.” In: *IEEE Photonics Technology Letters* 19.12 (2007), pp. 934–936.

-
- [53] F. Liu, J. Li, H. Luo, Q. Wu, X. Wu, F. Ouellette, and Y. Liu. “Study on soliton self-frequency shift in a Tm-doped fiber amplifier seeded by a Kelly-sideband-suppressed conventional soliton.” In: *Optics Express* 29.5 (2021), pp. 6553–6562.
- [54] B. R. Washburn, S. E. Ralph, P. A. Lacourt, J. M. Dudley, W. T. Rhodes, R. S. Windeler, and S. Coen. “Tunable near-infrared femtosecond soliton generation in photonic crystal fibres.” In: *Electronics Letters* 37.25 (2001), pp. 1510–1512.
- [55] I. G. Cormack, D. T. Reid, W. J. Wadsworth, J. C. Knight, and P. St J. Russell. “Observation of soliton self-frequency shift in photonic crystal fibre.” In: *Electronics Letters* 38.4 (2002), pp. 167–169.
- [56] N. Nishizawa, Y. Ito, and T. Goto. “Wavelength-Tunable Femtosecond Soliton Pulse Generation for Wavelengths of 0.78–1.0 μm Using Photonic Crystal Fibers and a Ultrashort Fiber Laser.” In: *Japanese Journal of Applied Physics* 42.2 (2003), p. 449.
- [57] H. Lim, J. Buckley, A. Chong, and F. W. Wise. “Fibre-based source of femtosecond pulses tunable from 1.0 to 1.3 μm .” In: *Electronics Letters* 40.24 (2004), pp. 1523–1525.
- [58] G. Soboń, T. Martynkien, D. Tomaszewska, K. Tarnowski, P. Mergo, and J. Sotor. “All-in-fiber amplification and compression of coherent frequency-shifted solitons tunable in the 1800-2000 nm range.” In: *Photonics Research* 6.5 (2018), pp. 368–372.
- [59] O. Szewczyk, P. Pala, K. Tarnowski, J. Olszewski, F. S. Vieira, C. Lu, A. Foltynowicz, P. Mergo, J. Sotor, G. Soboń, and T. Martynkien. “Dual-Wavelength Pumped Highly Birefringent Microstructured Silica Fiber for Widely Tunable Soliton Self-Frequency Shift.” In: *Journal of Lightwave Technology* 39.10 (2021), pp. 3260–3268.
- [60] D. G. Ouzounov, F. R. Ahmad, D. Müller, N. Venkataraman, M. T. Gallagher, M. G. Thomas, J. Silcox, K. W. Koch, and A. L. Gaeta. “Generation of megawatt optical solitons in hollow-core photonic band-gap fibers.” In: *Science (New York, N.Y.)* 301.5640 (2003), pp. 1702–1704.
- [61] J. Howe, J. H. Lee, S. Zhou, F. Wise, C. Xu, S. Ramachandran, S. Ghalmi, and M. F. Yan. “Demonstration of soliton self-frequency shift below 1300nm in higher-order mode, solid silica-based fiber.” In: *Optics Letters* 32.4 (2007), pp. 340–342.
- [62] J. H. Lee, J. Howe, C. Xu, S. Ramachandran, S. Ghalmi, and M. F. Yan. “Generation of femtosecond pulses at 1350 nm by Čerenkov radiation in higher-order-mode fiber.” In: *Optics Letters* 32.9 (2007), pp. 1053–1055.
- [63] O. Szewczyk, K. Tarnowski, A. Głuszek, D. Szulc, K. Stefańska, P. Mergo, and G. Soboń. “All-normal dispersion supercontinuum vs frequency-shifted solitons pumped at 1560 nm as seed sources for thulium-doped fiber amplifiers.” In: *Optics Express* 29.12 (2021), pp. 18122–18138.
- [64] G. Soboń, T. Martynkien, P. Mergo, L. Rutkowski, and A. Foltynowicz. “High-power frequency comb source tunable from 2.7 to 4.2 μm based on difference frequency

- generation pumped by an Yb-doped fiber laser.” In: *Optics Letters* 42.9 (2017), pp. 1748–1751.
- [65] R. Huber, M. Wojtkowski, J. G. Fujimoto, J. Y. Jiang, and A. E. Cable. “Three-dimensional and C-mode OCT imaging with a compact, frequency swept laser source at 1300 nm.” In: *Optics Express* 13.26 (2005), pp. 10523–10538.
- [66] R. Huber, M. Wojtkowski, and J. G. Fujimoto. “Fourier Domain Mode Locking (FDML): A new laser operating regime and applications for optical coherence tomography.” In: *Optics Express* 14.8 (2006), pp. 3225–3237.
- [67] N. G. Horton, K. Wang, D. Kobat, C. G. Clark, F. W. Wise, C. B. Schaffer, and C. Xu. “In vivo three-photon microscopy of subcortical structures within an intact mouse brain.” In: *Nature Photonics* 7.3 (2013), pp. 205–209.
- [68] H. Kawagoe, S. Ishida, M. Aramaki, Y. Sakakibara, E. Omoda, H. Kataura, and N. Nishizawa. “Development of a high power supercontinuum source in the 1.7 μm wavelength region for highly penetrative ultrahigh-resolution optical coherence tomography.” In: *Biomedical Optics Express* 5.3 (2014), pp. 932–943.
- [69] S. Ishida, N. Nishizawa, T. Ohta, and K. Itoh. “Ultrahigh-Resolution Optical Coherence Tomography in 1.7 μm Region with Fiber Laser Supercontinuum in Low-Water-Absorption Samples.” In: *Applied Physics Express* 4.5 (2011), p. 052501.
- [70] F. Forghieri, R. W. Tkach, and A. Chraplyvy. “Fiber Nonlinearities and Their Impact on Transmission Systems.” In: *Optical Fiber Telecommunications*. Vol. IIIA. 1997.
- [71] R. Fisher and W. Bischel. “The role of linear dispersion in plane-wave self-phase modulation.” In: *Applied Physics Letters* 23.12 (1973), pp. 661–663.
- [72] R. Fisher and W. Bischel. “Numerical studies of the interplay between self-phase modulation and dispersion for intense plane-wave laser pulses.” In: *Journal of Applied Physics* 46.11 (1975), pp. 4921–4934.
- [73] M. J. Ablowitz and J. F. Ladik. “A Nonlinear Difference Scheme and Inverse Scattering.” In: *Studies in Applied Mathematics* 55.3 (1976), pp. 213–229.
- [74] T. R. Taha and M. J. Ablowitz. “Analytical and numerical aspects of certain nonlinear evolution equations. II. Numerical, nonlinear Schrödinger equation.” In: *J. Comput. Phys.* 55 (1984), pp. 203–230.
- [75] Q. Sheng, A. Q. M. Khaliq, and E. A. Al-Said. “Solving the Generalized Nonlinear Schrödinger Equation via Quartic Spline Approximation.” In: *Journal of Computational Physics* 166.2 (2001), pp. 400–417.
- [76] T. Kremp and W. Freude. “Fast Split-Step Wavelet Collocation Method for WDM System Parameter Optimization.” In: *Journal of Lightwave Technology* 23.3 (2005), p. 1491.
- [77] J.R. Costa, P.M. Ramos, C.R. Paiva, and A.M. Barbosa. “Numerical study of passive gain equalization with twin-core fiber coupler amplifiers for WDM systems.” In: *IEEE Journal of Quantum Electronics* 37.12 (2001), pp. 1553–1561.

-
- [78] J.M. Dudley and S. Coen. “Numerical simulations and coherence properties of supercontinuum generation in photonic crystal and tapered optical fibers.” In: *IEEE Journal of Selected Topics in Quantum Electronics* 8.3 (2002), pp. 651–659.
- [79] G. Genty, M. Lehtonen, H. Ludvigsen, J. Broeng, and M. Kaivola. “Spectral broadening of femtosecond pulses into continuum radiation in microstructured fibers.” In: *Optics Express* 10.20 (2002), pp. 1083–1098.
- [80] T. Hori, N. Nishizawa, T. Goto, and M. Yoshida. “Experimental and numerical analysis of widely broadened supercontinuum generation in highly nonlinear dispersion-shifted fiber with a femtosecond pulse.” In: *JOSA B* 21.11 (2004), pp. 1969–1980.
- [81] N. Gautam, A. Choudhary, and B. Lall. “Comparative study of neural network architectures for modelling nonlinear optical pulse propagation.” In: *Optical Fiber Technology* 64 (2021), p. 102540.
- [82] P. Kaiser and H. W. Astle. “Low-loss single-material fibers made from pure fused silica.” In: *The Bell System Technical Journal* 53.6 (1974), pp. 1021–1039.
- [83] B. J. Eggleton, C. Kerbage, P. S. Westbrook, R. S. Windeler, and A. Hale. “Microstructured optical fiber devices.” In: *Optics Express* 9.13 (2001), pp. 698–713.
- [84] R. Windeler, J. Wagener, and D. DiGiovanni. “Silica-Air Microstructured Fibers: Properties and Applications.” In: *Optical Fiber Communication Conference and the International Conference on Integrated Optics and Optical Fiber Communication (1999)*, paper FG1. Optical Fiber Communication Conference. 1999, FG1.
- [85] J. C. Knight, T. A. Birks, P. St J. Russell, and D. M. Atkin. “All-silica single-mode optical fiber with photonic crystal cladding: errata.” In: *Optics Letters* 22.7 (1997), pp. 484–485.
- [86] J. Broeng, D. Mogilevstev, S. Barkou, and A. Bjarklev. “Photonic Crystal Fibers: A New Class of Optical Waveguides.” In: *Optical Fiber Technology* 5.3 (1999), pp. 305–330.
- [87] R. F. Cregan, B. J. Mangan, J. C. Knight, T. A. Birks, P. St. J. Russell, P. J. Roberts, and D. C. Allan. “Single-Mode Photonic Band Gap Guidance of Light in Air.” In: *Science* 285.5433 (1999), pp. 1537–1539.
- [88] T. A. Birks, J. C. Knight, and P. St J. Russell. “Endlessly single-mode photonic crystal fiber.” In: *Optics Letters* 22.13 (1997), pp. 961–963.
- [89] J. K. Ranka, R. S. Windeler, and A. J. Stentz. “Optical properties of high-delta air-silica microstructure optical fibers.” In: *Optics Letters* 25.11 (2000), pp. 796–798.
- [90] D. Mogilevtsev, T. A. Birks, and P. St J. Russell. “Group-velocity dispersion in photonic crystal fibers.” In: *Optics Letters* 23.21 (1998), pp. 1662–1664.
- [91] N. G. R. Broderick, T. M. Monro, P. J. Bennett, and D. J. Richardson. “Nonlinearity in holey optical fibers: measurement and future opportunities.” In: *Optics Letters* 24.20 (1999), pp. 1395–1397.

- [92] T. Yang, E. Wang, H. Jiang, Z. Hu, and K. Xie. “High birefringence photonic crystal fiber with high nonlinearity and low confinement loss.” In: *Optics Express* 23.7 (2015), pp. 8329–8337.
- [93] M. Lehtonen, G. Genty, H. Ludvigsen, and M. Kaivola. “Supercontinuum generation in a highly birefringent microstructured fiber.” In: *Applied Physics Letters* 82.14 (2003), pp. 2197–2199.
- [94] A. Ortigosa-Blanch, A. Diez, M. Delgado-Pinar, J.L. Cruz, and M.V. Andres. “Ultra-high birefringent nonlinear microstructured fiber.” In: *IEEE Photonics Technology Letters* 16.7 (2004), pp. 1667–1669.
- [95] J. K. Ranka, R. S. Windeler, and A. J. Stentz. “Visible continuum generation in air–silica microstructure optical fibers with anomalous dispersion at 800 nm.” In: *Optics Letters* 25.1 (2000), pp. 25–27.
- [96] Y. L. Hoo, W. Jin, C. Shi, H. L. Ho, D. N. Wang, and S. C. Ruan. “Design and modeling of a photonic crystal fiber gas sensor.” In: *Applied Optics* 42.18 (2003), pp. 3509–3515.
- [97] P. J. A. Sazio, A. Amezcua-Correa, C. E. Finlayson, J. E. Hayes, T. Scheidemantel, N. Baril, B. Jackson, D.-J. Won, F. Zhang, E. Margine, V. Gopalan, V. Crespi, and J. Badding. “Microstructured Optical Fibers as High-Pressure Microfluidic Reactors.” In: *Science* 311.5767 (2006), pp. 1583–1586.
- [98] J. Limpert, T. Schreiber, S. Nolte, H. Zellmer, A. Tünnermann, R. Iliew, F. Lederer, J. Broeng, G. Vienne, A. Petersson, and C. Jakobsen. “High-power air-clad large-mode-area photonic crystal fiber laser.” In: *Optics Express* 11.7 (2003), pp. 818–823.
- [99] S. Olyae and F. Taghipour. “Design of new square-lattice photonic crystal fibers for optical communication applications.” In: 2011.
- [100] G. Latha. “Solid Core Photonic Crystal Fiber for Dispersion tailoring in Optical Tele Communication systems.” In: *Journal of Advanced Optics and Photonics* 1.4 (1), pp. 291–302.
- [101] J. M. Dudley, G. Genty, and S. Coen. “Supercontinuum generation in photonic crystal fiber.” In: *Reviews of Modern Physics* 78.4 (2006), pp. 1135–1184.
- [102] R. R. Alfano and S. L. Shapiro. “Emission in the Region 4000 to 7000 Å Via Four-Photon Coupling in Glass.” In: *Physical Review Letters* 24.11 (1970), pp. 584–587.
- [103] R. R. Alfano and S. L. Shapiro. “Observation of Self-Phase Modulation and Small-Scale Filaments in Crystals and Glasses.” In: *Physical Review Letters* 24.11 (1970), pp. 592–594.
- [104] Herrmann, Griebner, Zhavoronkov, Husakou, Nickel, Korn, Knight, Wadsworth, and Russel. “Experimental evidence for supercontinuum generation by fission of higher-order solitons in photonic crystal fibers.” In: *2002 Summaries of Papers Presented at the Quantum Electronics and Laser Science Conference*. 2002 Summaries of

- Papers Presented at the Quantum Electronics and Laser Science Conference. 2002, pp. 165–166.
- [105] K.L. Corwin, N.R. Newbury, J.M. Dudley, S. Coen, S.A. Diddams, B.R. Washburn, K. Weber, and R.S. Windeler. “Fundamental amplitude noise limitations to supercontinuum spectra generated in a microstructured fiber.” In: *Applied Physics B* 77.2 (2003), pp. 269–277.
- [106] N. R. Newbury, B. R. Washburn, K. L. Corwin, and R. S. Windeler. “Noise amplification during supercontinuum generation in microstructure fiber.” In: *Optics Letters* 28.11 (2003), pp. 944–946.
- [107] A. Heidt. “Pulse preserving flat-top supercontinuum generation in all-normal dispersion photonic crystal fibers.” In: *JOSA B* 27.3 (2010), pp. 550–559.
- [108] A. Heidt, A. Hartung, G. Bosman, P. Krok, E. Rohwer, H. Schwoerer, and H. Bartelt. “Coherent octave spanning near-infrared and visible supercontinuum generation in all-normal dispersion photonic crystal fibers.” In: *Optics Express* 19.4 (2011), pp. 3775–3787.
- [109] A. Hartung, A. Heidt, and H. Bartelt. “Design of all-normal dispersion microstructured optical fibers for pulse-preserving supercontinuum generation.” In: *Optics Express* 19.8 (2011), pp. 7742–7749.
- [110] X. Gu, L. Xu, M. Kimmel, E. Zeek, P. O’Shea, A. Shreenath, R. Trebino, and R. Windeler. “Frequency-resolved optical gating and single-shot spectral measurements reveal fine structure in microstructure-fiber continuum.” In: *Optics Letters* 27.13 (2002), pp. 1174–1176.
- [111] X. Gu, M. Kimmel, A. P. Shreenath, R. Trebino, J. M. Dudley, S. Coen, and R. S. Windeler. “Experimental studies of the coherence of microstructure-fiber supercontinuum.” In: *Optics Express* 11.21 (2003), pp. 2697–2703.
- [112] K. L. Corwin, N. R. Newbury, J. M. Dudley, S. Coen, S. A. Diddams, K. Weber, and R. S. Windeler. “Fundamental noise limitations to supercontinuum generation in microstructure fiber.” In: *Physical Review Letters* 90.11 (2003), p. 113904.
- [113] K. Tarnowski, T. Martynkien, P. Mergo, J. Sotor, and G. Soboń. “Compact all-fiber source of coherent linearly polarized octave-spanning supercontinuum based on normal dispersion silica fiber.” In: *Scientific Reports* 9.1 (2019), p. 12313.
- [114] Shreesha Rao D. S, R. D. Engelholm, I. B. Gonzalo, B. Zhou, P. Bowen, P. Moselund, O. Bang, and M. Bache. “Ultra-low-noise supercontinuum generation with a flat near-zero normal dispersion fiber.” In: *Optics Letters* 44.9 (2019), pp. 2216–2219.
- [115] C. Finot, B. Kibler, L. Provost, and S. Wabnitz. “Beneficial impact of wave-breaking for coherent continuum formation in normally dispersive nonlinear fibers.” In: *JOSA B* 25.11 (2008), pp. 1938–1948.
- [116] A. Heidt, J. Feehan, J. Price, and T. Feurer. “Limits of coherent supercontinuum generation in normal dispersion fibers.” In: *JOSA B* 34.4 (2017), pp. 764–775.

- [117] J. Rothhardt, A. Heidt, S. Hädrich, S. Demmler, J. Limpert, and A. Tünnermann. “High stability soliton frequency-shifting mechanisms for laser synchronization applications.” In: *JOSA B* 29.6 (2012), pp. 1257–1262.
- [118] A. Heidt, J. Rothhardt, A. Hartung, H. Bartelt, E. Rohwer, J. Limpert, and A. Tünnermann. “High quality sub-two cycle pulses from compression of supercontinuum generated in all-normal dispersion photonic crystal fiber.” In: *Optics Express* 19.15 (2011), pp. 13873–13879.
- [119] S. Demmler, J. Rothhardt, A. Heidt, A. Hartung, E. Rohwer, H. Bartelt, J. Limpert, and A. Tünnermann. “Generation of high quality, 1.3 cycle pulses by active phase control of an octave spanning supercontinuum.” In: *Optics Express* 19.21 (2011), pp. 20151–20158.
- [120] K. Goda and B. Jalali. “Dispersive Fourier transformation for fast continuous single-shot measurements.” In: *Nature Photonics* 7.2 (2013), pp. 102–112.
- [121] Keisuke Goda, Daniel R. Solli, Kevin K. Tsia, and Bahram Jalali. “Theory of amplified dispersive Fourier transformation.” In: *Physical Review A* 80.4 (2009), p. 043821.
- [122] Ray-Kuang Lee, Yinchieh Lai, and Yuri S. Kivshar. “Quantum correlations in soliton collisions.” In: *Physical Review A* 71.3 (2005), p. 035801.
- [123] D. R. Solli, G. Herink, B. Jalali, and C. Ropers. “Fluctuations and correlations in modulation instability.” In: *Nature Photonics* 6.7 (2012), pp. 463–468.
- [124] B. Wetzels, A. Stefani, L. Larger, P. A. Lacourt, J. M. Merolla, T. Sylvestre, A. Kudlinski, A. Mussot, G. Genty, F. Dias, and J. M. Dudley. “Real-time full bandwidth measurement of spectral noise in supercontinuum generation.” In: *Scientific Reports* 2.1 (2012), p. 882.
- [125] T. Godin, B. Wetzels, T. Sylvestre, L. Larger, A. Kudlinski, A. Mussot, A. Ben Salem, M. Zghal, G. Genty, F. Dias, and J. M. Dudley. “Real time noise and wavelength correlations in octave-spanning supercontinuum generation.” In: *Optics Express* 21.15 (2013), pp. 18452–18460.
- [126] A. Głuszek, F. Senna Vieira, A. Hudzikowski, A. Wąż, J. Sotor, A. Foltynowicz, and G. Soboń. “Compact mode-locked Er-doped fiber laser for broadband cavity-enhanced spectroscopy.” In: *Applied Physics B* 126.8 (2020), p. 137.
- [127] G. Soboń, R. Lindberg, V. Pasiskevicius, T. Martynkien, and J. Sotor. “Shot-to-shot performance analysis of an all-fiber supercontinuum source pumped at 2000nm.” In: *JOSA B* 36.2 (2019), A15–A21.
- [128] S. P. Ó Dúill, R. Zhou, P. M. Anandarajah, and L. P. Barry. “Analytical Approach to Assess the Impact of Pulse-to-Pulse Phase Coherence of Optical Frequency Combs.” In: *IEEE Journal of Quantum Electronics* 51.11 (2015), pp. 1–8.
- [129] M. Bellini and T. Hänsch. “Phase-locked white-light continuum pulses: toward a universal optical frequency-comb synthesizer.” In: *Optics Letters* 25.14 (2000), pp. 1049–1051.

-
- [130] J. W. Nicholson and M. F. Yan. “Cross-coherence measurements of supercontinua generated in highly-nonlinear, dispersion shifted fiber at 1550 nm.” In: *Optics Express* 12.4 (2004), pp. 679–688.
- [131] A. F. J. Runge, C. Aguergaray, N. Broderick, and M. Erkintalo. “Coherence and shot-to-shot spectral fluctuations in noise-like ultrafast fiber lasers.” In: *Optics Letters* 38.21 (2013), pp. 4327–4330.
- [132] S. Kim, J. Park, S. Han, Y.-J. Kim, and S.-W. Kim. “Coherent supercontinuum generation using Er-doped fiber laser of hybrid mode-locking.” In: *Optics Letters* 39.10 (2014), pp. 2986–2989.
- [133] D.J. Kane and R. Trebino. “Characterization of arbitrary femtosecond pulses using frequency-resolved optical gating.” In: *IEEE Journal of Quantum Electronics* 29.2 (1993), pp. 571–579.
- [134] D. Kane and R. Trebino. “Single-shot measurement of the intensity and phase of an arbitrary ultrashort pulse by using frequency-resolved optical gating.” In: *Optics Letters* 18.10 (1993), pp. 823–825.
- [135] J. Kim and Y. Song. “Ultralow-noise mode-locked fiber lasers and frequency combs: principles, status, and applications.” In: *Advances in Optics and Photonics* 8.3 (2016), pp. 465–540.
- [136] C. Smith, R. Engelsholm, and O. Bang. “Pulse-to-pulse relative intensity noise measurements for ultrafast lasers.” In: *Optics Express* 30.5 (2022), pp. 8136–8150.
- [137] D. E. McCumber. “Intensity Fluctuations in the Output of cw Laser Oscillators. I.” In: *Physical Review* 141.1 (1966), pp. 306–322.
- [138] P. Z. Peebles. *Probability, random variables, and random signal principles*. 2nd edition. 1987. 349 pp.
- [139] K. Lee, C. Hensley, P. Schunemann, and M. E. Fermann. “Midinfrared frequency comb by difference frequency of erbium and thulium fiber lasers in orientation-patterned gallium phosphide.” In: *Optics Express* 25.15 (2017), pp. 17411–17416.
- [140] J. Luo, B. Sun, J. Ji, E. Tan, Y. Zhang, and X. Yu. “High-efficiency femtosecond Raman soliton generation with a tunable wavelength beyond 2 μm .” In: *Optics Letters* 42.8 (2017), pp. 1568–1571.
- [141] N. Nishizawa, Y. Ito, and T. Goto. “0.78-0.90- μm wavelength-tunable femtosecond soliton pulse generation using photonic crystal fiber.” In: *IEEE Photonics Technology Letters* 14.7 (2002), pp. 986–988.
- [142] J. H. V. Price, K. Furusawa, T. M. Monro, L. Lefort, and D. J. Richardson. “Tunable, femtosecond pulse source operating in the range 1.06–1.33 μm based on an Yb^{3+} -doped holey fiber amplifier.” In: *JOSA B* 19.6 (2002), pp. 1286–1294.
- [143] D. T. Reid, I. G. Cormack, W. J. Wadsworth, J. C. Knight, and P. ST. J. Russell. “Soliton self-frequency shift effects in photonic crystal fibre.” In: *Journal of Modern Optics* 49.5 (2002), pp. 757–767.

- [144] J. Takayanagi, T. Sugiura, M. Yoshida, and N. Nishizawa. “1.0–1.7- μ m Wavelength-Tunable Ultrashort-Pulse Generation Using Femtosecond Yb-Doped Fiber Laser and Photonic Crystal Fiber.” In: *IEEE Photonics Technology Letters* 18.21 (2006), pp. 2284–2286.
- [145] J. Sotor and G. Sobon. “24 fs and 3 nJ pulse generation from a simple, all polarization maintaining Er-doped fiber laser.” In: *Laser Physics Letters* 13.12 (2016), p. 125102.
- [146] J. C. Travers, M. H. Frosz, and J. M. Dudley. “Nonlinear fibre optics overview.” In: *Supercontinuum Generation in Optical Fibers*. 2010, pp. 32–51.
- [147] J. Lægsgaard. “Mode profile dispersion in the generalized nonlinear Schrödinger equation.” In: *Optics Express* 15.24 (2007), pp. 16110–16123.
- [148] O. Humbach, H. Fabian, U. Grzesik, U. Haken, and W. Heitmann. “Analysis of OH absorption bands in synthetic silica.” In: *Journal of Non-Crystalline Solids* 203 (1996), pp. 19–26.
- [149] P. Balla and G. P. Agrawal. “Nonlinear interaction of vector solitons inside birefringent optical fibers.” In: *Physical Review A* 98.2 (2018), p. 023822.
- [150] S. Dekker, A. Judge, R. Pant, I. Gris-Sánchez, J. C. Knight, C. Sterke, and B. Eggleton. “Highly-efficient, octave spanning soliton self-frequency shift using a specialized photonic crystal fiber with low OH loss.” In: *Optics Express* 19.18 (2011), pp. 17766–17773.
- [151] Y. Tang, L. Wright, K. Charan, T. Wang, C. Xu, and F. Wise. “Generation of intense 100 fs solitons tunable from 2 to 4.3 μ m in fluoride fiber.” In: *Optica* 3.9 (2016), pp. 948–951.
- [152] T. Neely, T. Johnson, and C. Diddams. “High-power broadband laser source tunable from 3.0 μ m to 4.4 μ m based on a femtosecond Yb: fiber oscillator.” In: *Optics Letters* 36.20 (2011), pp. 4020–4022.
- [153] R F Stevens. *Polarisation extinction ratio-measurement requirements for optical communication systems*. NPL Rep. CETM 41. 2002.
- [154] D. Penninckx and N. Beck. “Definition, meaning, and measurement of the polarization extinction ratio of fiber-based devices.” In: *Applied Optics* 44.36 (2005), pp. 7773–7779.
- [155] W. Liu, C. Li, H. Chung, S.-H. Chia, Z. Zhang, F. Kärtner, and G. Chang. “Widely tunable ultrafast sources for multi-photon microscopy.” In: *Conference on Lasers and Electro-Optics (2016), paper SM2I.7*. CLEO: Science and Innovations. 2016, SM2I.7.
- [156] F. Adler and S. Diddams. “High-power, hybrid Er: fiber/Tm: fiber frequency comb source in the 2 μ m wavelength region.” In: *Optics Letters* 37.9 (2012), pp. 1400–1402.
- [157] P. Kadwani, J. Chia, F. Altal, R. Sims, C. Willis, L. Shah, D. Killinger, and M. Richardson. “Atmospheric absorption spectroscopy using Tm: fiber sources around two microns.” In: *Atmospheric and Oceanic Propagation of Electromagnetic Waves*

- V. Atmospheric and Oceanic Propagation of Electromagnetic Waves V. Vol. 7924. 2011, p. 79240L.
- [158] E. Passacantilli, G. Anichini, G. Lapadula, M. Salvati, J. Lenzi, and A. Santoro. “Assessment of the utility of the 2- μm thulium laser in surgical removal of intracranial meningiomas.” In: *Lasers in Surgery and Medicine* 45.3 (2013), pp. 148–154.
- [159] H. Jeong, S. Choi, M. Kim, F. Rotermund, Y. Cha, D.-Y. Jeong, S. Lee, K. Lee, and D. Yeom. “All-fiber Tm-doped soliton laser oscillator with 6 nJ pulse energy based on evanescent field interaction with monolayer graphene saturable absorber.” In: *Optics Express* 24.13 (2016), pp. 14152–14158.
- [160] J. Wang, X. Liang, G. Hu, Z. Zheng, S. Lin, D. Ouyang, X. Wu, P. Yan, S. Ruan, Z. Sun, and T. Hasan. “152 fs nanotube-mode-locked thulium-doped all-fiber laser.” In: *Scientific Reports* 6.1 (2016), p. 28885.
- [161] J. Jiang, C. Mohr, J. Bethge, A. Mills, W. Mefford, I. Hartl, M. E. Fermann, C.-C. Lee, S. Suzuki, T. R. Schibli, N. Leindecker, K. L. Vodopyanov, and P. G. Schunemann. “500 MHz, 58fs highly coherent Tm fiber soliton laser.” In: *2012 Conference on Lasers and Electro-Optics (CLEO)*. 2012 Conference on Lasers and Electro-Optics (CLEO). 2012, pp. 1–2.
- [162] P. Wang, C. Bao, B. Fu, X. Xiao, P. Grelu, and C. Yang. “Generation of wavelength-tunable soliton molecules in a 2-m ultrafast all-fiber laser based on nonlinear polarization evolution.” In: *Optics Letters* 41.10 (2016), pp. 2254–2257.
- [163] T. Zhu, F. Xiao, L. Xu, M. Liu, M. Deng, and K. Chiang. “Pressure-assisted low-loss fusion splicing between photonic crystal fiber and single-mode fiber.” In: *Optics Express* 20.22 (2012), pp. 24465–24471.
- [164] N. Coluccelli, M. Cassinerio, A. Gambetta, P. Laporta, and G. Galzerano. “High-power frequency comb in the range of 2 μm based on a holmium fiber amplifier seeded by wavelength-shifted Raman solitons from an erbium-fiber laser.” In: *Optics Letters* 39.6 (2014), pp. 1661–1664.
- [165] N. Coluccelli, M. Cassinerio, P. Laporta, and G. Galzerano. “Single-clad Tm–Ho: fiber amplifier for high-power sub-100-fs pulses around 1.9 μm .” In: *Optics Letters* 38.15 (2013), pp. 2757–2759.
- [166] T. Hori, J. Takayanagi, N. Nishizawa, and T. Goto. “Flatly broadened, wideband and low noise supercontinuum generation in highly nonlinear hybrid fiber.” In: *Optics Express* 12.2 (2004), pp. 317–324.
- [167] N. Nishizawa and J. Takayanagi. “Octave spanning high-quality supercontinuum generation in all-fiber system.” In: *JOSA B* 24.8 (2007), pp. 1786–1792.
- [168] A. Rampur, A. Rampur, Y. Stepanenko, G. Stępniewski, T. Kardaś, D. Dobrakowski, D.-M. Spangenberg, T. Feurer, A. Heidt, and M. Klimczak. “Ultra low-noise coherent supercontinuum amplification and compression below 100 fs in an all-fiber polarization-maintaining thulium fiber amplifier.” In: *Optics Express* 27.24 (2019), pp. 35041–35051.

- [169] A. Heidt, J. Modupeh Hodasi, A. Rampur, D. Spangenberg, M. Ryser, M. Klimczak, and T. Feurer. “Low noise all-fiber amplification of a coherent supercontinuum at 2 μm and its limits imposed by polarization noise.” In: *Scientific Reports* 10.1 (2020), p. 16734.
- [170] M Klimczak, G. Soboń, R. Kasztelanic, K. Abramski, and R. Buczyński. “Direct comparison of shot-to-shot noise performance of all normal dispersion and anomalous dispersion supercontinuum pumped with sub-picosecond pulse fiber-based laser.” In: *Scientific Reports* 6.1 (2016), p. 19284.
- [171] D. Huang, E. A. Swanson, C. P. Lin, J. S. Schuman, W. G. Stinson, W. Chang, M. R. Hee, T. Flotte, K. Gregory, and C. A. Puliafito. “Optical coherence tomography.” In: *Science (New York, N.Y.)* 254.5035 (1991), pp. 1178–1181.
- [172] S. H. Yun, C. Boudoux, G. J. Tearney, and B. E. Bouma. “High-speed wavelength-swept semiconductor laser with a polygon-scanner-based wavelength filter.” In: *Optics Letters* 28.20 (2003), pp. 1981–1983.
- [173] D. Miller, J. Jarrett, A. Hassan, and A. Dunn. “Deep tissue imaging with multiphoton fluorescence microscopy.” In: *Current Opinion in Biomedical Engineering* 4 (2017), pp. 32–39.
- [174] M. Yu. Koptev, E. A. Anashkina, A. V. Andrianov, V. V. Dorofeev, A. F. Kosolapov, S. V. Muravyev, and A. V. Kim. “Widely tunable mid-infrared fiber laser source based on soliton self-frequency shift in microstructured tellurite fiber.” In: *Optics Letters* 40.17 (2015), p. 4094.
- [175] O. Szewczyk, Z. Łaszczych, and G. Soboń. “Spectral compression and amplification of ultrashort pulses tunable in the 1650 – 1900 nm wavelength range.” In: *Optics & Laser Technology* 164 (2023), p. 109465.
- [176] M. Oberthaler and R. A. Höpfel. “Special narrowing of ultrashort laser pulses by self-phase modulation in optical fibers.” In: *Applied Physics Letters* 63.8 (1998), p. 1017.
- [177] E. Andresen, J. Thøgersen, and S. Keiding. “Spectral compression of femtosecond pulses in photonic crystal fibers.” In: *Optics Letters* 30.15 (2005), pp. 2025–2027.
- [178] Esben Ravn Andresen, John M. Dudley, Dan Oron, Christophe Finot, and Hervé Rigneault. “Transform-limited spectral compression by self-phase modulation of amplitude-shaped pulses with negative chirp.” In: *Optics Letters* 36.5 (2011), pp. 707–709.
- [179] A. B. Fedotov, A. A. Voronin, I. V. Fedotov, A. A. Ivanov, and A. M. Zheltikov. “Spectral compression of frequency-shifting solitons in a photonic-crystal fiber.” In: *Optics Letters* 34.5 (2009), p. 662.
- [180] J. Limpert, N. Deguil-Robin, I. Manek-Hönniger, F. Salin, T. Schreiber, A. Liem, F. Röser, H. Zellmer, A. Tünnermann, A. Courjaud, C. Hönniger, and E. Mottay. “High-power picosecond fiber amplifier based on nonlinear spectral compression.” In: *Optics Letters* 30.7 (2005), p. 714.

-
- [181] R. Liang, X. Zhou, Z. Zhang, Z. Qin, H. Li, and Y. Liu. “Numerical investigation on spectral compression of femtosecond soliton in a dispersion-increasing fiber.” In: *Optical Fiber Technology* 15.5 (2009), pp. 438–441.
- [182] W. Chao, Y. Lin, J. Peng, and C. Huang. “Adiabatic pulse propagation in a dispersion-increasing fiber for spectral compression exceeding the fiber dispersion ratio limitation.” In: *Optics Letters* 39.4 (2014), pp. 853–856.
- [183] N. Nishizawa, Y. Andou, E. Omoda, H. Kataura, and Y. Sakakibara. “Characteristics and improvement of wideband wavelength-tunable narrow-linewidth source by spectral compression in quasi-dispersion-increasing comb-profile fiber.” In: *Optics Express* 24.20 (2016), pp. 23403–23418.
- [184] J. Limpert, A. Liein, T. Gabler, H. Zellmer, and A. Tünnerinann. “SPM-induced spectral compression of picosecond pulses in a single-mode Yb-doped fiber amplifier.” In: *Advanced Solid-State Lasers (2002)*, paper MD8. Advanced Solid State Lasers. 2002, p. MD8.
- [185] D. Sidorov-Biryukov, E. Serebryannikov, and A. Zheltikov. “Time-resolved coherent anti-Stokes Raman scattering with a femtosecond soliton output of a photonic-crystal fiber.” In: *Optics Letters* 31.15 (2006), pp. 2323–2325.
- [186] N. Nishizawa, K. Takahashi, Y. Ozeki, and K. Itoh. “Wideband spectral compression of wavelength-tunable ultrashort soliton pulse using comb-profile fiber.” In: *Optics Express* 18.11 (2010), p. 11700.
- [187] S. V. Chernikov, J. R. Taylor, and R. Kashyap. “Comblike dispersion-profiled fiber for soliton pulse train generation.” In: *Optics Letters* 19.8 (1994), pp. 539–541.
- [188] K. Igarashi, J. Hiroishi, T. Yagi, and S. Namiki. “Comb-like profiled fibre for efficient generation of high quality 160 GHz sub-picosecond soliton train.” In: *Electronics Letters* 41.12 (2005), pp. 688–690.
- [189] Y. Lin and C. Huang. “Large-scale and structure-tunable laser spectral compression in an optical dispersion-increasing fiber.” In: *Optics Express* 25.15 (2017), pp. 18024–18030.
- [190] N. Nishizawa and K. Takahashi. “Time-domain near-infrared spectroscopy using a wavelength-tunable narrow-linewidth source by spectral compression of ultrashort soliton pulses.” In: *Optics Letters* 36.19 (2011), pp. 3780–3782.
- [191] Z. Li, Y. Jung, J. M. O. Daniel, N. Simakov, M. Tokurakawa, P. C. Shardlow, D. Jain, J. K. Sahu, A. M. Heidt, W. A. Clarkson, S. U. Alam, and D. J. Richardson. “Exploiting the short wavelength gain of silica-based thulium-doped fiber amplifiers.” In: *Optics Letters* 41.10 (2016), pp. 2197–2200.
- [192] Z. Li, Y. Jung, J. M. O. Daniel, N. Simakov, P. C. Shardlow, A. M. Heidt, W. A. Clarkson, S. U. Alam, and D. J. Richardson. “Extreme Short Wavelength Operation (1.65 – 1.7 μm) of Silica-Based Thulium-Doped Fiber Amplifier.” In: *Optical Fiber Communication Conference (2015)*, paper Tu2C.1. Optical Fiber Communication Conference. 2015, Tu2C.1.

- [193] J. M. O. Daniel, N. Simakov, M. Tokurakawa, M. Ibsen, and W. A. Clarkson. “Ultra-short wavelength operation of a thulium fibre laser in the 1660–1750 nm wavelength band.” In: *Optics Express* 23.14 (2015), pp. 18269–18276.

List of achievements

List of publications

1. **O. Szewczyk**, Z. Łaszczych, G. Soboń, "Spectral compression and amplification of ultrashort pulses tunable in the 1650 – 1900 nm wavelength range", *Optics & Laser Technology*. vol. **164**, 109465, p. 1-5.
2. **O. Szewczyk**, K. Tarnowski, A. Głuszek, D. Szulc, K. Stefańska, P. Mergo, G. Soboń, All-normal dispersion supercontinuum vs frequency-shifted solitons pumped at 1560 nm as seed sources for thulium-doped fiber amplifiers *Optics Express*, 2021, vol. **29**, no 12, p. 18122-18138
3. **O. Szewczyk**, P. Pala, K. Tarnowski, J. Olszewski, F. S. Vieira, C. Lu, A. Foltynowicz, P. Mergo, J. Sotor, G. Soboń, T. Martynkien, "Dual-wavelength pumped highly birefringent microstructured silica fiber for widely tunable soliton self-frequency shift", *Journal of Lightwave Technology*, 2021, vol. **39**, no 10, p. 3260-3268.

Conference papers

- **O. Szewczyk**, G. Statkiewicz-Barabach, J. Olszewski, K. Żołnacz, M. Makara, K. Poturaj, P. Mergo, J. Sotor, G. Soboń, W. Urbańczyk, "Highly birefringent all-normal dispersion silica fiber with flat dispersion profile in the 1200–2100 nm wavelength range", *EPJ Web of Conferences*, ISSN 2100-014X; vol. 267
- **O. Szewczyk**, A. Głuszek, T. Martynkien, K. Tarnowski, P. Mergo, G. Soboń, "Demonstration of supercontinuum and frequency shifted solitons pumped at 1.56 μm as seed sources for Tm-doped fiber amplifiers", *EPJ Web of Conferences*, ISSN 2100-014X; vol. 243

Conference contributions

- **O. Szewczyk**, G. Statkiewicz-Barabach, J. Olszewski, K. Żołnacz, M. Makara, K. Poturaj, P. Mergo, J. Sotor, G. Soboń, W. Urbańczyk, "Highly birefringent all-normal dispersion silica fiber with flat dispersion profile in the 1200–2100 nm wavelength range", Europhoton, Hannover, Germany, poster
- **O. Szewczyk**, G. Statkiewicz-Barabach, J. Olszewski, K. Żołnacz, M. Makara, K. Poturaj, P. Mergo, J. Sotor, G. Soboń, W. Urbańczyk, "Włókno światłowodowe o wysokiej

- dwójłomności z normalną dyspersją w zakresie długości fali 1200-2100 nm XIII Sympozjum Techniki Laserowej STL 2022", Karpacz, Polska, poster
- **O. Szewczyk**, Z. Łaszczych, G. Soboń, "Szeroko przestrajalne, wąskopasmowe źródło laserowe w zakresie długości fali 1600-1800 nm", Polska Konferencja Optyczna 2022, Płock, Polska, talk
 - **O. Szewczyk**, Z. Łaszczych, G. Soboń, "All-fiber tunable system of spectrally-compressed soliton pulses amplified in the 1600-1800 nm wavelength range", IONS Ireland 2021, online, talk
 - **O. Szewczyk**, G. Soboń, "All-fiber amplification system of spectrally-compressed soliton pulses tunable in the 1600-1800 nm wavelength range", EOS Annual Meeting (EOSAM) 2021, Rome, Italy, poster
 - **O. Szewczyk**, G. Soboń, "All-fiber narrow-linewidth laser source tunable in the 1600-1800 nm range", Opto 2021 Wrocław, online, talk
 - **O. Szewczyk**, A. Głuszek, T. Martynkien, K. Tarnowski, P. Mergo, G. Soboń, "Demonstration of supercontinuum and frequency shifted solitons pumped at 1.56 μm as seed sources for Tm-doped fiber amplifiers", Europhoton 2020, online, talk
 - **O. Szewczyk**, A. Głuszek, T. Martynkien, K. Tarnowski, P. Mergo, G. Soboń, "Raman-shifted solitons vs all-normal dispersion supercontinuum as seed sources for Thulium-doped fiber amplifiers", Siegman International School on Lasers 2020, online, poster
 - **O. Szewczyk**, A. Głuszek, T. Martynkien, K. Tarnowski, P. Mergo, G. Soboń, "Comparison between all-normal dispersion supercontinuum and frequency shifted soliton as seed sources for Tm-doped fiber amplifiers", Opto 2020, online, talk
 - **O. Szewczyk**, A. Głuszek, T. Martynkien, K. Tarnowski, P. Mergo, G. Soboń, "Demonstracja superkontinuuum i efektu samo-przesunięcia częstotliwości solitonów w światłowodach mikrostrukturalnych do zastosowań jako źródła do światłowodowych wzmacniaczy tulowych", V Ogólnopolska Studencka Fizyczno-Optyczna Konferencja FOKA 2020, online, talk
 - **O. Szewczyk**, G.Sobon, J. Sotor, K. Stefanska, K. Tarnowski, K. Poturaj, M. Makara, P. Mergo, T. Martynkien, "Soliton self-frequency shift in microstructured silica fibers", Opto 2019, Poland, Toruń, talk
 - **O. Drożdżowska**, G.Sobon, J. Sotor, K. Stefanska, K. Tarnowski, K. Poturaj, M. Makara, P. Mergo, T. Martynkien, "Soliton self-frequency shift in microstructured silica fibers", ELISS Summer School 2019, Prague, poster
 - J. Sotor, M. Pawliszewska, **O. Drożdżowska**, D. Tomaszewska, G. Soboń, "All-fiber, Ultrafast Seed Sources Operating in 2 μm Spectral Range", PIERS 2019 Rome, talk

Patents submission

- Kamil Dybka, Mateusz Pietryna, Marek Biduś, Michał Dłubek, Mariusz Dyrkacz, Karolina Stefańska, Tadeusz Martynkien, Grzegorz Soboń, Jarosław Sotor, **Olga Szewczyk**, Paweł Mergo, Mariusz Makara, title: "Pasywny nieliniowy moduł światłowodowy", date of registration: 13.07.2022

Participation in scientific projects

- "Spectral compression of ultrashort laser pulses tunable in the biological window of 1600-1800 nm", Financed by the National Centre of Science (NCN)
- "Polarization-maintaining dispersion-engineered fiber modules in the spectral range 1500-2000 nm", Financed by the National Centre for Research and Development (NCBR)
- "National Laboratory for Photonics and Quantum Technologies", financed by European Regional Development Fund
- "Dispersion-engineered fiber modules for tunable laser sources", Financed by the National Centre for Research and Development (NCBR)
- "Ultrashort-pulsed fiber amplifiers for the mid-infrared spectral range", Financed by The Polish Ministry of Science and Higher Education (MNiSW)

Scientific schools and trainings

- 28-29.08.2022 Europhoton Summer School
- 19-23.07.2021 All-Stars Virtual Siegman School
- 20-24.07.2020 All-Stars Virtual Siegman School
- 25-30.08.2019 ELISS Summer School 2019, Prague, Czech Republic

Research stays

- 11.10 – 6.11.2022 Umeå University, Department of Physics, Umeå, Sweden. Supervision: prof. Aleksandra Foltynowicz-Matyba.

Awards

- Best Oral Presentation Award at the OPTICA IONS Ireland 2021 Conference (Virtual Event)
- Prize of the Rector of the Wrocław University of Science and Technology for scientific achievements (academic year 2021/2022)

List of achievements

- Prize of the Rector of the Wrocław University of Science and Technology for scientific achievements (academic year 2020/2021)
- 10.11.2020 Prize of the Dean of the Faculty of the Electronics for scientific achievements (academic year 2019/2020)